UNIVERSITÉ DE STRASBOURG

EDSC
École Doctorale des Sciences Chimiques

UNIVERSITÉ FRANCO ITALIENNE | UNIVERSITÀ ITALO FRANCESE

UNIVERSITÉ DE STRASBOURG

ÉCOLE DOCTORALE DES SCIENCES CHIMIQUES

THÈSE

EN CO-TUTELLE AVEC L'UNIVERSITÉ DE FERRARA
FINANCÉ PAR BANDO VINCI 2013

présentée par

Laura FERLAUTO

Soutenue le: **25 février 2015**

pour obtenir le grade de

Docteur de l'Université de Strasbourg

Discipline/ Spécialité: Chimie/Physique

Correlation between structural and electrical properties of organic semiconducting materials

THÈSE dirigée par:

M GUIDI Vincenzo	Prof., Università degli Studi di Ferrara
M SAMORÌ Paolo	Prof., Université de Strasbourg

RAPPORTEURS:

Mme FRABONI Beatrice	Prof., Università degli studi di Bologna
M MORGANTE Alberto	Prof., Università degli studi di Trieste

EXAMINATEURS:

M MAURO Matteo	Dr. MdC., Université de Strasbourg
M SILWA Michel	Dr., Université de Lille
Mme MILITA Silvia	Dr., IMM-CNR Bologna

Università degli Studi di Ferrara

UNIVERSITÉ FRANCO ITALIENNE
UNIVERSITÀ ITALO FRANCESE

DOTTORATO DI RICERCA IN
FISICA

CICLO XXVII

COORDINATORE Prof. VINCENZO GUIDI

Tesi in co-tutela con l'Università di Strasburgo
finanziata dal Bando Vinci 2013

CORRELATION BETWEEN STRUCTURAL AND ELECTRICAL PROPERTIES OF ORGANIC SEMICONDUCTING MATERIALS

Settore Scientifico Disciplinare FIS/01

Dottorando
Dott. FERLAUTO LAURA

Tutore
Prof. GUIDI VINCENZO

Co-tutore
Prof. SAMORÍ PAOLO

Referee
Prof. FRABONI BEATRICE, Università di Bologna
Prof. MORGANTE ALBERTO, Università di Trieste
Prof. SCHREIBER FRANK, Università di Tubinga (Germania)
Prof. RESEL ROLAND, Università di Graz (Austria)

Altri membri della commissione
Dr. SLIWA MICHEL, Università di Lille (Francia)
Dr. MdC. MAURO MATTEO, Università di Strasburgo (Francia)
Dr. MILITA SILVIA, IMM-CNR di Bologna

Anni 2012/2014

To Max and his patience.
To Faby and the diplomacy
which I will never learn.

This thesis is as mine as yours.

ACKNOWLEDGMENTS

These last years have been like a very intense journey full of satisfactions. The achievement of this PhD represents an important milestone in my life, both from the scientific and personal point of view, which is exactly what I was looking for.

I am indebted to Prof. Guidi who let me continue the research already started at IMM-CNR of Bologna in total freedom and supported me in the realization of the co-supervision between Ferrara and Strasbourg. Also, I would like to express here my gratitude to the administrative office of the Physics Department and the Doctoral office, which helped this ″exotic case″ out with all the bureaucracy of many travels and missions.

I am grateful to Prof. Samorí for welcoming me in his group and offering me the opportunity to differentiate my skills at the ISIS facilities in Strasbourg. There, I learned how to face problems from other perspectives and to exchange the scientific knowledge with colleagues. The time spent with them at work and after work was priceless and the friendship that I have built with some of them will always be essential for me.

I deeply acknowledge the IMM-CNR of Bologna for welcoming me right after the Master degree and financially supporting me during the entire PhD. In particular, I want to explicitly acknowledge Dr. Milita and Dr. Liscio for the constant supervision and suggestions aimed to improve my work. From them I learned the importance of a scrupulous characterization of a physical system and I believe this imprinting will accompany me in future.

A big thanks goes to Prof. Biscarini's old group at ISMN-CNR of Bologna, which was the very first big group I got in touch with. Participating to the meetings and the scientific discussions about the research topics studied within the group was very helpful to enlarge and enrich the view of science that I had at the beginning. Moreover, sharing every-day lab-life with other PhD students and postdocs contributed to establish precious lasting friendships.

My deepest gratitude goes to all the commission members, Prof. Fraboni, Prof. Morgante, Dr. Mauro and Dr. Sliwa, as well as to the external referees, Prof. Resel and Prof. Schreiber, for the time they dedicated to me and my thesis. Having external scientific opinions and comments on the work I carried out is of fundamental importance for my future.

In the end, as always, I am thankful to all the people who trust and love me: my family, Max, his family, old and new friends as well as close and very far ones. All of you contributed to make this journey amazing.

Laura Ferlauto

INDEX

SUMMARY

Résumé

Introduction

La première fois qu'un semi-conducteur organique (OS), agissant comme couche active dans un transistor à effet de champ, a été rapporté, date de 1986 [1]. A partir de cette date, les OS ont suscité de plus en plus d'attention, notamment du fait de la polyvalence dans la conception du matériau, offrant des possibilités sans limites dans la construction de molécules ayant des propriétés électroniques ad-hoc pour divers dispositifs électroniques, tels que les diodes électroluminescentes organiques (OLED), les cellules photovoltaïques organiques (OPV)[2], les transistors à effet de champ organiques (OFET) et les transistors électroluminescents organiques (OLET)[3]. Les efforts des chercheurs ont conduit la transition de ces dispositifs, de simple curiosité scientifique, à une potentielle technologie, importante pour l'électronique grand public [4]. Leur adaptabilité chimique [5], couplée à la possibilité de les exploiter par des méthodes de mise en forme rapides et peu coûteuses, représentent le principal intérêt pour l'avènement d'une nouvelle génération d'électronique légère et produtite à faible coût, basée sur des dispositifs imprimables et flexibles [6–11]. De nos jours par exemple, les OS sont utilisés dans la fabrication de différents types de détecteurs, notamment comme détecteurs dans de la peau synthétique [12], et ils entrent également dans le domaine de la spintronique [13].

La nécessité d'applications produites à faible coût et sur de grandes surfaces, compatibles avec des substrats flexibles, a conduit la communauté scientifique à penser de nouveaux matériaux semi-conducteurs organiques, se caractérisant par une solubilité élevée dans les solvants communs, avec une bonne stabilité à l'air et une mobilité des porteurs de charge élevée, pour les transistors à effets de champ organique (OFET) [14], le bloque de construction de l'électronique organique.

Le succés de la production de matériaux π-conjugués est principalement lié à une meilleure compréhension physique de la relation structure-propriétés. Parmi les nombreux facteurs influençant le comportement d'un dispositif organique, il y a sa géométrie, l'épaisseur et le type de diélectrique, les électrodes et les propriétés intrinsèques du matériau organique, ainsi que sa microstructure, qui est sa structure cristalline, l'orientation et l'arrangement des molécules sur le substrat, la formations de domaines cristallins ou la présence de désordre et de défauts est certainement le plus grand défi, et a la plus grande influence sur le transport de charge survenant dans les OFET [15, 16]. Des interactions entre molécules au cœur π-conjugué, i. e. de la prolongation de l'ordre moléculaire au matériau massif [17], dépend le transfert de charge entre molécules. D'autre part, les interactions intermoléculaires gouvernent également la solubilité du matériau, influençant son procédé d'utilisation. Par conséquent, l'ordre structural au niveau supramoléculaire, le procédé et les perfcormances du dispositif sont étroitement liés [18–20].

Eclaircir le lien entre les propriétés structurales et électriques de plusieurs matériaux semi-conducteurs organiques, de petites molécules ou de polymères, caractérisés par différents degrés de cristallinité, est l'objectif de cette thèse. Les OFET peuvent être fabriqués en exploitant différents matériaux organiques et architectures, déposés soit par une technique basée sur une solution, soit par sublimation sous vide. Du fait du haut degré de cristallinité et d'homogénéité, les dispositifs basés sur la sublimation sous vide sont largement étudiés comme système modèle, pour la compréhension de la physique des semi-conducteurs organiques. Même s'ils sont plus attrayants pour des applications peu coûteuses, les dispositifs réalisés à partir d'une technique basée sur une solution présentent moins d'ordre cristallin, en comparaison avec ceux par sublimation sous vide, et leur étude détaillée représente encore un défi. Différentes approches sont présentées dans cette thèse, pour relever ce défi : des méthodes structurales ex-situ standards, ainsi que d'autres, in-situ et en temps réel, plus compliquées et moins conventionnelles

L'approche structurale ex-situ

La caractérisation ex-situ (structurale, morphologique, électrique, optique, etc.) d'un système à l'équilibre est l'une des approches les plus communes dans la littérature. Tout particulièrement, dans cette thèse, elle a été utilisée pour étudier les OFET basés sur deux dérivés de pérylènes, ainsi que pour des transistors ambipolaires fabriqué à partir de polymère de type n et p en solution, déposés selon une technique particulière.

Différemment de leurs homologues (les OS de type p), les matériaux organiques de type n sont plus sensibles aux conditions environnementales, et donc, moins stables. Malgré ce défi de stabilité, les OS de type n sont essentiels dans le développement d'une électronique complémentaire, qui sera capable de combiner des substrats flexibles avec une consommation d'énergie restreinte [21–24]. Parmi les semi-conducteurs organiques de type n, les dérivés de pérylène alkyldiimide (PDI) ont été choisis pour leurs bonnes performances électriques, ainsi que pour la facilité d'utilisation [25, 26]. En particulier, nous avons étudié des PDI présentant un cœur fonctionnalisé par des groupements cyano, ce qui diminue l'énergie de l'orbitale inoccupée la plus basse en énergie [27, 28] améliorant la stabilité à l'air, ainsi que fonctionnalisé par des chaînes latérales, qui améliore la solubilité du matériau, et donc, la qualité de dépôt réalisé. L'introduction de chaînes latérales dans des molécules π-conjugués affecte également l'étendue de l'ordre moléculaire, et, par conséquent, l'efficacité du transport de charge dans le matériau, dont l'aspect a été étudié. Les OFET basés sur des couches minces spin-coatés de dicyanopérylène, décorés avec une chaîne linéaire (PDI8-CN2 - N, N'-bis (n-octyl) -dicyanoperylene-3,4: 9,10-bis-dicarboximide), ou avec une chaîne branchée (N1400 - N, N'-bis- (2-éthylhexyl) -1,7-dicyano-pérylène-3,4: 9,10-bis (dicarboximide)) ont été étudiés dans le but de comprendre le rôle de la forme de la chaîne alkyle, sur la structure de la couche mince, et par conséquent, des performances du dispositif.

Les résultats montrent que pour les dérivés de PDI, l'introduction d'une chaîne alkyle asymétrique branchée permet d'obtenir, lors d'un recuit, un OFET avec des propriétés de transport accrues, par rapport aux chaînes alkyles linéaires. L'espèce branchée conduit à la formation de films constitués d'un mélange de quatre stéréo-isomères, deux RR/SS, ainsi qu'une paire énantiomérique RS/SR, qui engendre un désordre conformationnel, favorisant un mode de croissance 2D (Figure 1). Pour ces molécules, un recuit post-dépôt optimisé conduit à une transition structurale vers la phase massive, préservant tout de même la morphologie 2D, et améliorant les propriétés de transport des dispositifs en couche mince. En revanche, les molécules avec des chaînes alkyles linéaires s'auto-assemblent en îlots 3D stables, présentant une structure de phase massive, qui maintient sa taille constante, sans changements majeurs dans les caractéristiques des OFET, lors de traitements thermiques.
Ces résultats montrent comment la substitution d'une molécule de dicyanopérylène, avec une chaîne alkyle asymétrique branchée, peut être une stratégie efficace pour obtenir, juste après un traitement thermique, un transistor à effet de champ avec des propriétés de transport améliorées, comparées aux chaînes alkyles linéaires. En outre, ce constat montre que le désordre généré par des chaînes alkyles asymétriques branchées, quand la molécule est physisorbée en couche mince, peut contribuer à l'augmentation du transport de charge, par un traitement thermique [29].

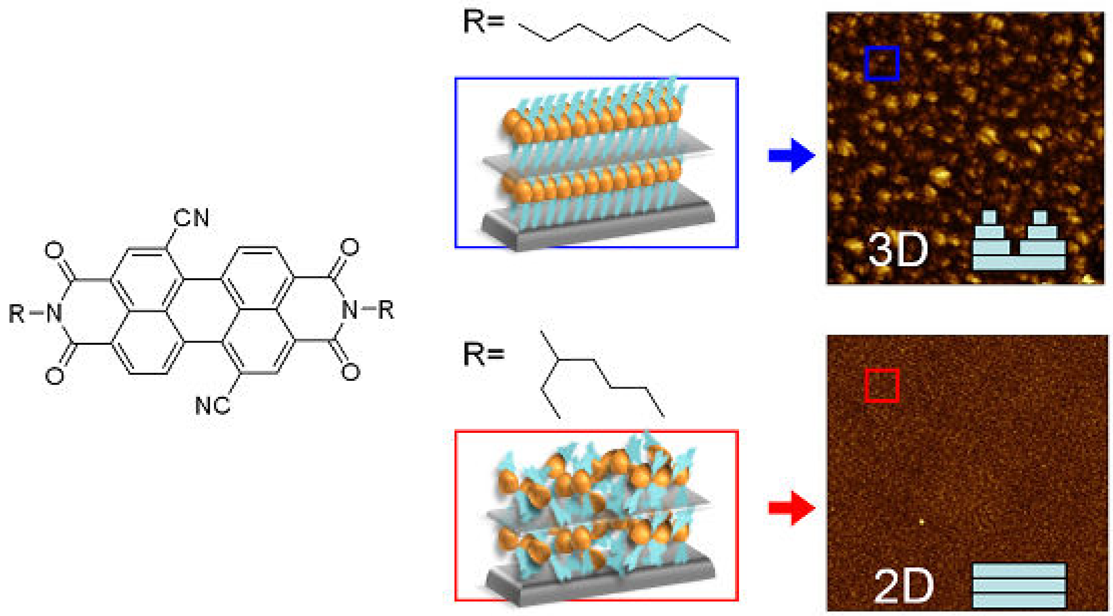

Figure 1: Schéma de l'effet de la forme des chaînes alkyles latérales sur les isoméres de dérivés de pérylène. L'espèce branchée conduit à la formation d'une phase 2D métastable plus désordonnée, constituée d'un mélange de quatre stéréo-isoméres distincts, alors que l'espéce linéaire est responsable de l'apparition d'une phase plus ordonnée, caractérisée par une morphologie 3D.

La seconde étude ex-situ concerne la caractérisation d'OFET à double couche ambipolaire, basée sur des multicouches de films minces polymériques de type n et p, déposés par la technique de Langmuir-Schaefer (LS). La production d'OFET ambipolaires avec des mobilités électron-trou, à la fois élevées et équivalentes, est actuellement un point important dans la recherche, du fait de son application potentielle dans les circuits organiques intégrés. La possibilité d'obtenir simultanément un transport des deux types de porteurs de charge, non seulement conduirait à une simplification de la structure des circuits logiques complémentaires, mais voudrait également réduire la dissipation d'énergie ainsi que le bruit. La technique LS permet la fabrication d'un dispositif ambipolaire par dépôts successifs des couches de type n et p, à partir des solutions. Cette méthode implique la création d'une monocouche épaisse, par diffusion d'une solution à l'interface eau-air, puis transfert en plaçant doucement en contact un substrat solide avec le film à la surface de l'eau [30]; cette procédure peut être réalisée une seule fois, si une monocouche est voulue, ou plusieurs fois si de multiples couches doivent être déposées (Figure 2). Cette technique permet un contrôle prcis de l'épaisseur du film, et favorise un empilement moléculaire rigide, ainsi qu'un ordre à grande échelle, dans la structure de la couche déposée.

Généralement, la mobilité des charges dans les dispositifs polymériques souffrent de peu d'empilement, et d'un manque d'ordre microscopique induit par la conformation

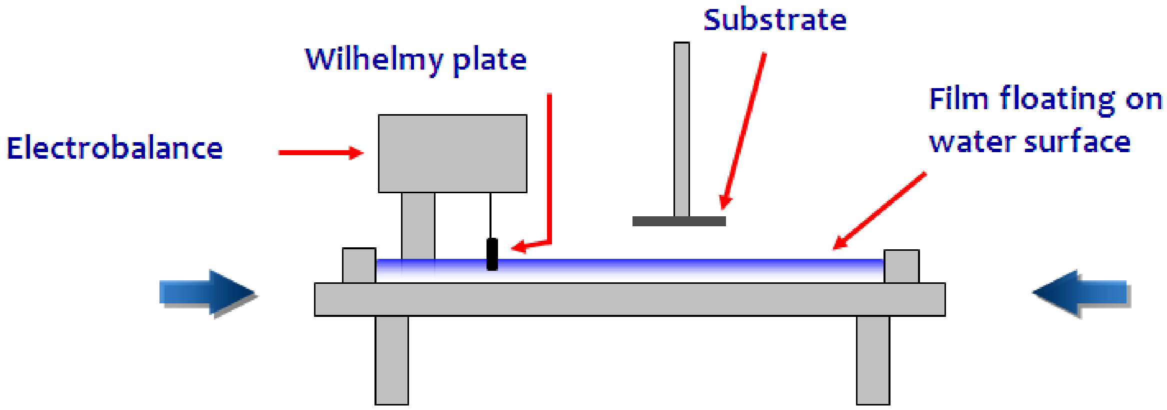

Figure 2: Schéma d'un dispositif de dépôt de type Langmuir-Schaefer. Une solution contenant le matériau organique est doucement déposée à la surface de l'eau ; puis, les barrières mobiles contraignent les molécules (ou monomères) à s'empiler, et à former un film continu. Quand la pression de surface désirée, mesurée par une balance de Wilhelmy, est atteinte, le dépôt peut avoir lieu.

du polymère lui-même, ainsi que par la présence de longues chaînes alkyles qui créent un effet stérique approprié [31]. En comparaison à d'autres techniques de dépôt à partir de solution, la méthode LS force l'empilement des polymères, dans une configuration favorisant le transport de charge. Pour cette étude particulière, l'IIDDT-C3, un polymère conjugué prometteur de type p, basé sur un cœur isoindogo, a été choisi pour ses performances électriques exceptionnellement hautes, et sa bonne cristallinité atteinte par une technique de spin-coating [32] avec P(NDI2OD-T2)(ou N2200, un remarquable polymère commercial de type n, qui a déjà démontré sa réponse électrique élevée par spin-coating et LS [33–36]. Aprés avoir choisi les conditions optimales de dépôt pour les matériaux de type n et p, les monocouches et bicouches composés de la superposition de N2200 et IIDDT-C3 (et inversement), ont été caractérisées structuralement.

Une mesure GIXRD (pour Grazing Incidence X-Ray Diffraction) fourni des informations nécessaires sur les effets de la technique de dépôt utilisée, sur l'ordre cristallin et l'empilement moléculaire des couches organiques. Les monocouches de types p et n présentent des arrangements sur la tranche (edge-on) des couches lamellaires polymériques, par rapport cc la surface (Figure 3), qui est également maintenue dans les architectures ambipolaires, et permet ainsi d'atteindre des mobilités de trous (μ_h) et d'électrons (μ_e) remarquables, avec des valeurs, en régime de saturation, de l'ordre de 10^{-1} et $10^{-2} cm^2/Vs$, respectivement. Par ailleurs, la couche d'IIDDT-C3 présente une organisation comparable à des fibres, induite par la technique de dépôt LS, prouvée par des images de microscopie à force atomique.

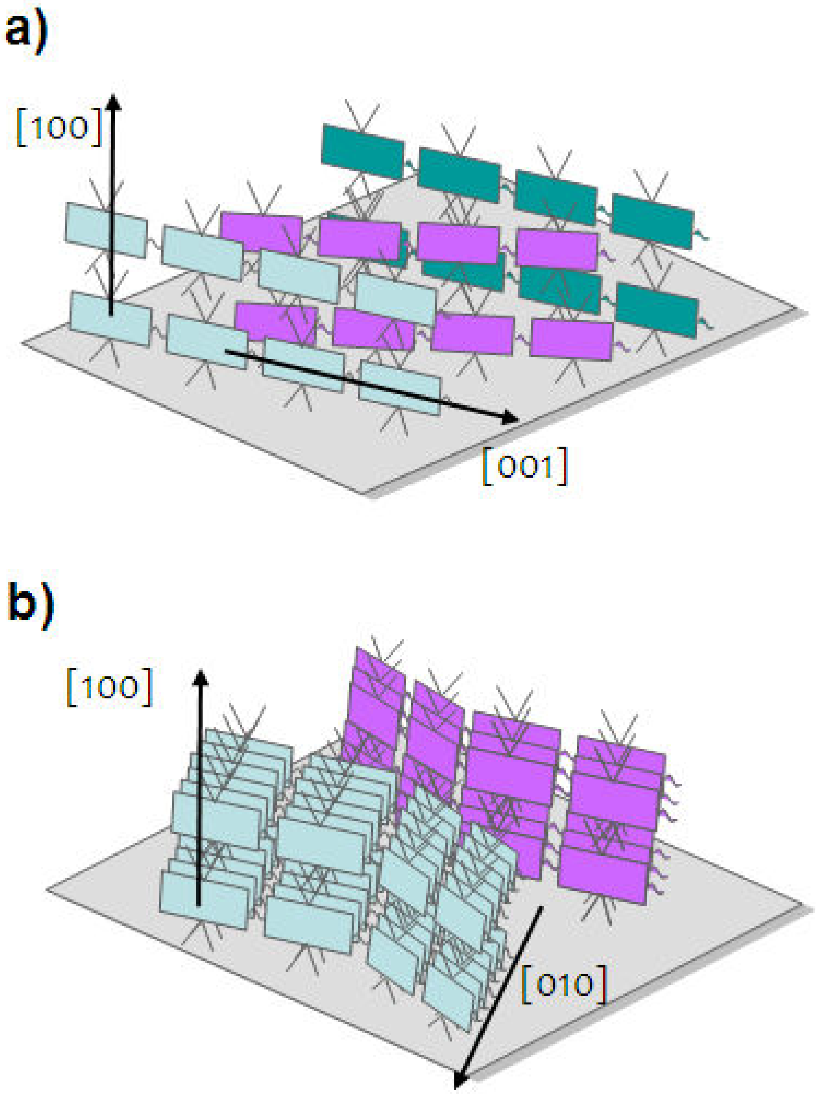

Figure 3: Schéma de l'arrangement sur la tranche (edge-on) d'une lamelle polymérique a) de type n et b) de type p, par rapport à la surface du substrat.

Investigation structural in-situ et en temps réel

L'approche basée sur une analyse structurale in-situ et en temps réel est la démarche la plus appropriée pour décrire l'évolution structurale d'un système hors équilibre. Cela implique que la caractérisation structurale soit réalisée précisément lors de la réponse du système à un stimulus externe. Malgré l'énorme quantité de données physiques qui peuvent être extrapolées, cette approche n'est pas vraiment courante, du fait de la complexité expérimentale de pouvoir suivre l'évolution rapide des phénomènes. Cette stratégie a été utilisée lors de cette thèse, pour étudier l'effet d'un champ électrique sur la structure de pentacène évaporé dans un OFET, ainsi que pour suivre l'évolution structurale de couche mince de dérivés de thiophène, pour des applications de détecteur d'humidité, lors de variations relatives d'humidités dans l'environnement.

Comme il a déjà été étudié dans la littérature [37–39], le transport de charge dans les OFET est fortement influencé par la structure et la morphologie du film organique à l'interface avec le diélectrique. Cependant, les changements structuraux dans la couche de semi-conducteur organique, induits par le champ électrique influençant les porteurs de charge de l'électrode source vers l'électrode drain, sont toujours inconnus. Les mesures in-situ en temps réel, de diffraction des rayons X utilisant une source de radiation synchrotron, les géométries incidentes, spéculaires et d'incidence rasante, sont toutes les deux réalisées sur l'OFET basé sur le pentacène, dans le but de résoudre l'évolution structurale du matériau organique lors de l'application d'un potentiel entre source-gate (V_{SG}) et source-drain (V_{SD}). Des OFET de type bottom-gate top contact, adaptés pour la réalisation des mesures de rayons X dans la chaîne du dispositif, ont été fabriqués. Le Schéma de l'expérience est représenté en Figure 4.

Le faisceau de rayons X a été concentré sur la chaîne du dispositif, et deux réflexions de Bragg différentes ont été modulées lors de l'application constante des potentiels V_{SG} et V_{SD} au transistor. Plus spécifiquement, la réflexion (001), dans la direction hors du plan (q_z), a donné un aperçu de l'évolution du réseau de plans parallèles à la surface du substrat, alors que la réflexion 11, dans la direction du plan (q_{xy}) nous a permis d'observer les modifications dans la périodicité du réseau de plans perpendiculairement orientés par rapport à la surface du substrat.

Avec cette expérience singulière, il a été possible de démontrer pour la première fois l'apparition d'une expansion du réseau, dans la direction q_z, du fait d'une inclinaison (quelques mrads) des molécules de pentacène lors de l'application de V_{SG} et V_{SD}. Le résultat est réversible, et appuyé par de la dynamique moléculaire, et des simulations de théorie de la fonctionnelle de densité (DFT). De plus, une réorganisation dans le plan des molécules localisées sur les bords des domaines cristallins a été observée, en lien avec l'application d'un champ électrique externe à la structure du pentacène.

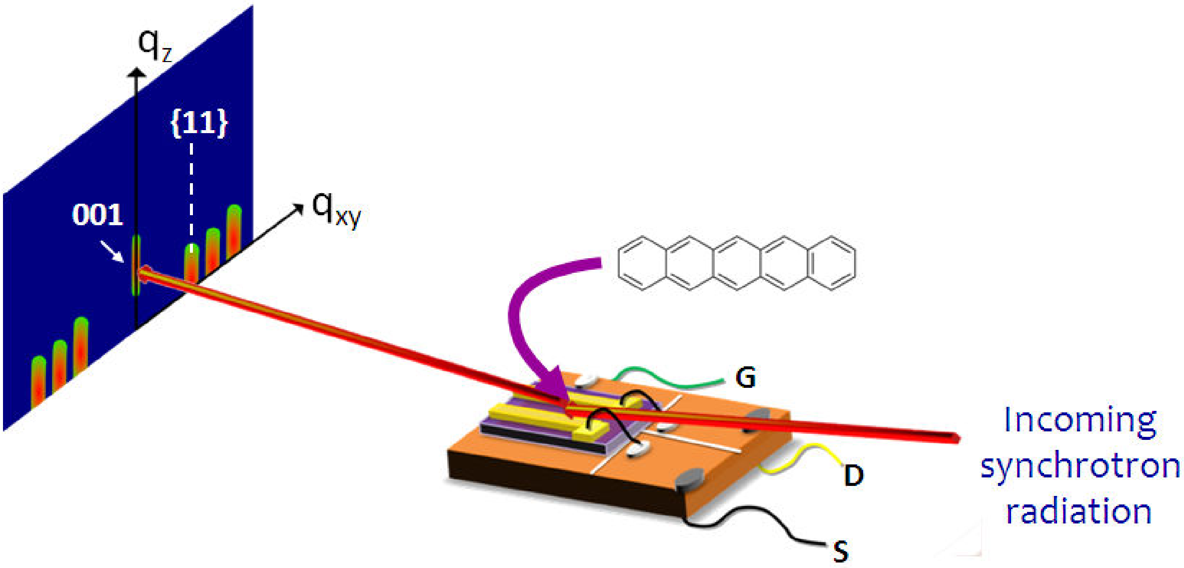

Figure 4: Schéma de l'expérience in-situ, en temps réel, basée sur les OFET avec le pentacène.

Les matériaux organiques basés sur le tetrathiafulvalene- (TTF-) sont largement étudiés pour des applications en tant que détecteurs [40–43]. Des échantillons constitués par des couches minces conductrices, basés sur du TTF, au-dessus d'une matrice de polymère, ont été étudiés par le groupe du professeur Rovira (ICMAB-CSIC, Spain). Une chambre humide artisanale, adaptée pour des mesures de rayons X et électriques simultanées, dans une atmosphère contrôlée, a été construite et positionnée sur le goniomètre du diffractomètre du laboratoire (Figure 5).
La chambre a été connectée à une sonde thermo-hygrométrique et à un tube de gaz, par lequel un flux d'azote humide a été introduit, dans le but d'atteindre le RH% voulu. Deux fenêtre en Kapton permettent de laisser passer le faisceau de rayons X incident, pour atteindre l'échantillon situé à l'intérieur de la chambre, et que le faisceau réfléchi/diffracté puisse atteindre le détecteur. Ce montage, permet l'analyse de certains pics caractéristiques du matériau, lors des variations relatives d'humidité (RH%). Le résultat montre que les variations de RH% affectent de manière réversible la structure de la couche mince; notamment, une expansion du réseau a été corrélée à l'incrémentation de RH%, suggérant que les molécules d'eau pénètrent à l'intérieur des cristallites, modifiant les paramètres de maille.

Conclusion

En conclusion, dans cette thèse, des exemples d'approche ex-situ multitechnique ainsi que d'investigation structurale in-situ en temps réel, sur différents matériaux semi-conducteurs

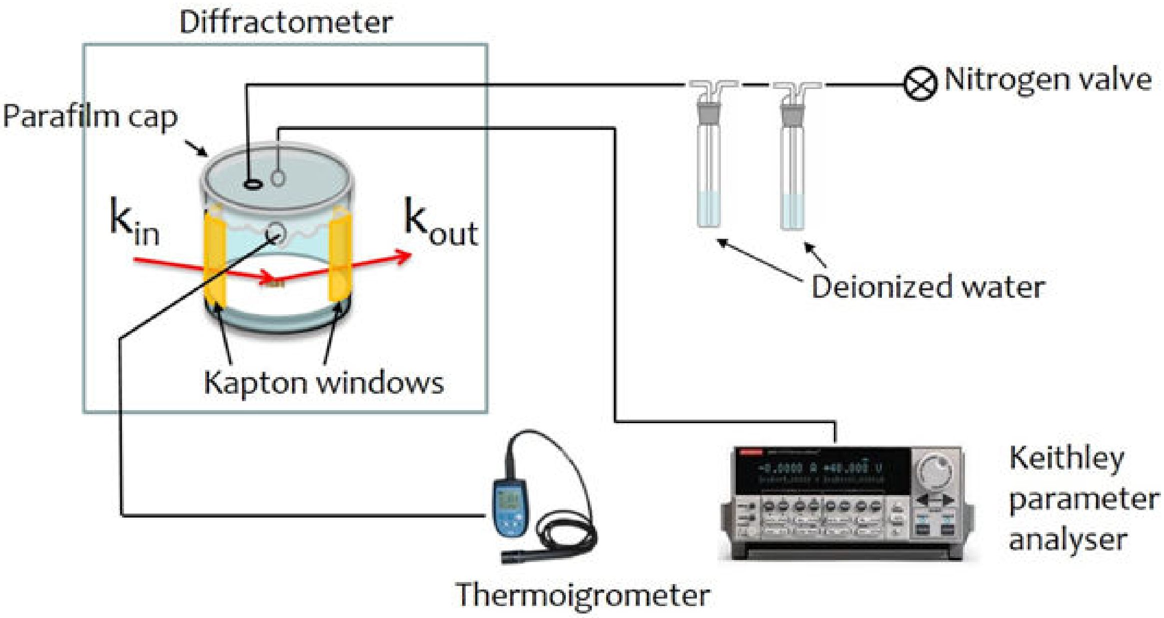

Figure 5: Schéma du montage expérimental pour les mesures in-situ, en temps réel, dans une atmosphère contrôlée.

organiques, sont présentés. La caractérisation structurale des systèmes a été effectuée par des techniques de diffraction de rayons X, exploitant à la fois les sources communes du laboratoire, ainsi que les radiations du synchrotron. Les informations obtenues sur l'ordre cristallin, l'empilement et l'arrangement des matériaux organiques ont été corrélées à la morphologie des films, et finalement, des performances électriques des OFET correspondant. Dans tous les cas, l'étude multi-échelle des interconnections entre les propriétés structurales, morphologiques et électriques d'un système apporte une description complète des matériaux eux même, ainsi que sur les dispositifs utilisés. Les résultats présentés sont le fruit d'investigations multitechniques, sur des dispositifs à couche mince. Nous avons démontré que les deux approches adoptées, ex-situ, et in-situ en temps réel, peuvent apporter un soutien irremplaçable à la description correct du lien entre les propriétés structurales et électriques de différents systèmes organiques.

Ce manuscrit présente les résultats de 3 années de travail de doctorat, en co-tutelle entre l'Université de Ferrara (Italie) et l'Université de Strasbourg (France), avec le support financier de l'Université Franco-Italienne avec le Bando Vinci 2013. Ce travail a été principalement effectué à l'Istituto di Microelettronica e Microsistemi du Consiglio Nazionale delle Ricerche (IMM-CNR) de Bologne (Italie), ainsi qu'à l'Institut de Science et d'Ingénierie Supramoléculaire (ISIS) de Strasbourg (France).

Organisation du manuscrit

La thèse est organisée comme suit. Une introduction sur les généralités des semi-conducteurs organiques, incluant les principales méthodes de transport de charge connues à ce jour, et une description du principe de fonctionnement d'un OFET, ainsi que les principaux facteurs influençant ses performances, est donné dans **Chapitre 1**.

Dans le **Chapitre 2**, les principales techniques utilisées pour la fabrication et la caractérisation du matériau étudié sont décrites. Une attention toute particulière est dédiée aux techniques de caractérisation structurales, incluant aussi bien les mesures standards de rayons X du laboratoire que celles du synchrotron.

Les résultats sur la première étude multitechnique sont présentés dans le **Chapitre 3**. Les OFET basés sur les isomères de dérivés de pérylènes, différenciés uniquement par la forme de la chaîne alkyle latérale, et déposés à partir d'une solution, ont été structurellement, morphologiquement, et électriquement caractérisés. Ces résultats indiquent les capacités d'une organisation supramoléculaire sur une surface et le transport de charge, a être affectés par l'introduction d'une modification chimique (structurale).

Le **Chapitre 4** illustre, pour la première fois, la fabrication et la caractérisation d'un dispositif ambipolaire à bicouche, basée sur des couches actives de polymères déposés à partir d'une solution. Dans ce cas, la technique de dépôt utilisée impose une orientation aux chaînes polymèriques, qui semblent adaptées pour des performances électriques remarquables.

Le **Chapitre 5** répond à une question fondamentale et non résolue au sujet des OFET. Dans cette étude, un matériau organique bien connu (le pentacène) a été sublimé sous vide, sur le substrat, et la géométrie du dispositif n'a pas été optimisée pour obtenir des performances surprenantes. Le but de ce travail a été de détecter l'effet d'un champ électrique sur la structure d'une couche active d'un OFET, lors du fonctionnement de celui-ci. Pour ce projet, une caractérisation in-situ en temps réel, non conventionnelle, basée sur les radiations d'un synchrotron, a été exploitée.

Le **Chapitre 6** décrit les résultats préliminaires de l'investigation structurale in-situ en temps réel, d'une couche mince flexible, sensible aux variations d'humidité. Pour cette étude, un dispositif ad-hoc expérimental, permettant de réaliser simultanément des mesures électriques et structurales dans une atmosphère contrôlée, a été construit. Dans ce cas, la source de rayons X du laboratoire a été utilisée, et les résultats préliminaires obtenus soulignent les limites comme le potentiel de ce dispositif. D'avantage d'optimisations de l'appareillage doivent être réalisées, dans le but de poursuivre ce projet. Seulement, dans ce cas-ci, la couche mince organique caractérisée a été fournie par le groupe du Prof. Rovira, de l'Institut de Ciencia de Materials de Barcelona du Consejo Superior de Investigaciones Cientifica (ICMAB-CSIC)(Spain).

Les principales conclusions pour chaque étude présentées, tout comme les perspectives pour de futurs projets, ont été résumées dans le dernier chapitre, à savoir le **Chapitre 7**.

Abstract

The need of low-cost and large-area applications compatible with flexible substrates has guided the scientific community to the design of new organic semiconducting materials characterized by high solubility in common solvents, good air stability and high charge carrier mobility for organic field effect transistors (OFETs) devices, the building blocks of organic electronics. The success of this generation of π-conjugated materials is principally related to the improved physical understanding of their structure-properties relationship. The material microstructure, that is its crystalline structure, its molecular packing, the orientation and arrangement of the molecules on a substrate, the formation of crystalline domains as well as the presence of disorder and defects, has in fact a strong influence on the charge transport taking place in the OFET [15, 16]. To unravel the relationship linking the structural and electrical properties of several organic semiconducting materials, small molecules and polymers, characterized by different degrees of crystalline order is the aim of this thesis. OFETs can be fabricated exploiting a variety of architectures and organic materials deposited either by solution based techniques or vacuum sublimation. Thanks to the high degree of crystalline order and large homogeneity, vacuum sublimated devices are largely studied as model-systems for the comprehension of the organic semiconductor physics. Even though more attractive for inexpensive applications, solution based devices presents less crystaline order with respect to vacuum sublimated ones and their deep investigation still represents a challenge. Two basic approaches for the nvestigation of the relationship between structural and electrical properties of some organic materials were adopted in this thesis: ex-situ multiple characterization and in-situ and real-time structural investigation.

The ex-situ characterization (structural, morphological, electrical, optical, etc.) of the system at the equilibrium is one of the most common approaches in literature. In this thesis it has been exploited to investigate OFETs based on two perylene derivatives as well as on ambipolar transistors fabricated with solution processable n-type and p-type polymers deposited with a particular technique. Among n-type organic semiconductors, perylene alkyldiimide derivatives (PDIs) were chosen for their good electrical performance as well as excellent processability. [25, 26]. In particular,we studied PDIs exhibiting a core functionalized with cyano-groups, which lower the lowest unoccupied molecular orbital energy [27, 28] improving the air stability, and side chains, which increment the solubility and thus the material processability. The introduction of side chains in π-conjugated molecules also affects the extent of molecular order and consequently the efficiency of charge transport in the material and it is this aspect that we investigated. OFETs based on spin-coated thin films of dicyanoperylene molecules decorated with either linear (PDI8-CN2 - N,N′-bis(n-octyl)-dicyanoperylene-3,4:9,10-bis-dicarboximide) or branched (N1400 - N,N′-bis-(2-ethylhexyl)-1,7-dicyano-perylene-3,4:9,10-bis (dicarboximide)) side chains were studied to elucidate the role of the alkyl chins shape on the struc-

ture of the thin films and consequently on the device performance. The results demonstrate that in PDI derivatives the introduction of asymmetric branched alkyl chains allows obtaining, upon thermal annealing, OFETs with enhanced transport properties with respect to linear alkyl chains. The branched specie leads to the formation of films consisting on a mixture of four stereoisomers, two RR/SS and RS/SR enantiomeric pairs which introduce conformational disorder favoring the 2D-growth mode. For these molecules optimized post-deposition thermal annealing leads to a structural transition towards the bulk-phase, still preserving the 2D morphology and improving the transport properties of thin film devices. Conversely, molecules with linear alkyl chains self-assemble in stable 3D islands exhibiting the bulk phase structure which keep their size constant without major changes in the OFETs characteristics upon thermal treatment. These results show how the substitution of a dicyanoperylene molecule with asymmetric branched alkyl chains can be an effective strategy for obtaining, just after simple thermal annealing, field-effect transistors with enhanced transport properties with respect to linear alkyl chains. Moreover, these findings demonstrate that the disorder generated by the asymmetric branched chains when the molecule is physisorbed in thin film can be instrumental for enhancing charge transport via thermal annealing [29].

The second ex-situ study concerns the characterization of bilayer ambipolar OFETs based on multiple-layers of n-type and p-type polymeric thinfilms deposited by Langmuir-Schaefer (LS) technique. The production of ambipolar OFETs with high and balanced electron-hole mobilities is currently a research highlight due to their potential application in organic integrated circuits. The possibility of obtaining a simultaneous transport of both types of carriers would not only lead to a simplification in the design of complementary logic circuits, but would also reduce power dissipation and increase noise margins. The LS technique permits the fabrication of an ambipolar device by the consecutive deposition of both n- and p-type layers from solutions. This method involves the creation of a single monolayer thick film by spreading a solution at the water-air interface and then transferring it by gently putting in contact a solid substrate with the film floating on the water surface [30]; the procedure can be performed just one time if a single monolayer is needed or many times if multiple layers have to be deposited. This technique enables an accurate control over the film thickness and favors a strong molecular packing and long-range order in the structure of the deposited layer. Generally, charge mobility in polymeric devices suffers from poor packing and lack of microscopic order induced by the polymer conformation itself and the presence of long alkyl chains which create a relevant steric hindrance [31]. With respect to other deposition techniques from solution, the LS method forces the polymer packing in an advantageous configuration for charge transport. For this particular study, IIDDT-C3, a promising isoindigo-based conjugated p-type polymer, was chosen for exceptionally high electrical performance and good crystalline order already reached by spin-coating technique [32] together with P(NDI2OD-T2) (or N2200), a commercial outstanding n-type polymer, which has already demonstrated high electrical response both in spin-coated and LS thin-films [33–36]. After choosing optimal deposition conditions for the n-type and p-type materials, single layers and bilayers composed by the superposition of N2200 and IIDDT-C3 (and vice versa) were structurally characterized. Grazing incidence X-ray diffraction measurements provided necessary information about the effect of the deposition technique onto the crystalline order and molecular packing of the organic layers. Single p- and n-type layers showed an edge-on arrangement of the polymeric lamella with respect to the surface which was maintained also in the ambipolar architectures and enabled to reach remarkable holes (μh) and electrons (μe) mobility, with values in saturation regime of the order of 10^{-1}. Moreover, the IIDDT-C3 layer showed a fiber-like organization induced by the LS deposition technique further proved by atomic force microscopy images.

The approach based on the in-situ and real-time structural investigation is the most appropriate one to describe the structural evolution of a system under not equilibrium circumstances. It implies that the structural characterization is performed exactly during the system response to an external stimulus. Despite the tremendous amount of physical information that can be extrapolated, this approach is not very common due to the experimental complexity of following fast evolving phenomena. This strategy has been exploited in this thesis to study the effect of the electric field on the structure of evaporated pentacene in working OFET as well as to follow the structural evolution of thiophene derivative thin films for humidity sensor applications during the relative humidity variation in the environment. As already known in literature [37–39], in OFETs charge transport is strongly influenced by the structure and morphology of the organic film at the interface with the dielectric. Nevertheless, the structural changes in the organic semiconducting layer induced by the electric field drifting the charge carriers from the source to the drain electrode are still unknown. In-situ and real-time X-Ray diffraction measurements using a synchrotron radiation source, both in specular and grazing incidence geometries, were thus performed on pentacene-based OFETs to elucidate the structural evolution of the organic material during the application of gate (V_{SG}) and source-drain (V_{SD}) bias. Ad-hoc bottom-gate top-contact OFETs suitable for the realization of X-ray measurements inside the device channel were fabricated. Although very small (few mrad), it was possible to demonstrate for the first time the occurrence of a lattice expansion due to the tilt of pentacene molecules during the V_{SG} and V_{SD} application. The result is reversible and supported by molecular dynamics and DFT simulations.

Tetrathiafulvalene- (TTF-) based organic materials are widely studied for sensors applications [40–43]. Samples constituted by a thin TTF-based conductive layer on top of a polymeric matrix were supplied by the group of Professor Rovira (ICMAB-CSIC, Spain). A home-made humidity chamber adapted for simultaneous X-rays and electrical measurements in a controlled atmosphere was built and set on the goniometer of the laboratory diffractometer. The chamber was connected to a hygrometer probe and to a gas tube, through which a hydrate nitrogen flux was inflated, in order to reach the desired relative humidity (RH%). Two kapton windows allowed the X-ray incident beam to reach the sample positioned inside the chamber and the reflected/diffracted beam to reach the detector. This setup allowed for the X-ray analysis of some characteristic peaks of the material during RH% variation. The results demonstrated that the variation of RH% reversibly affects the thin-film structure; in particular a lattice expansion was correlated to the increment of RH%, suggesting that water molecules penetrate inside the crystallites modifying the lattice parameters.

In conclusion, in this thesis examples of multi-technique approach as well as in-situ and real-time structural investigations on different organic semiconducting materials are presented. In both cases, the multiscale study of the close interconnection between structural, morphological and electrical properties of a system brought to a comprehensive description of the materials themselves and of the devices based on them.

This manuscript presents the results of a 3 years Ph.D. work in co-supervision between the University of Ferrara and the University of Strasbourg under the financial support of the French-Italian University with the Bando Vinci 2013. The work has been mainly carried out at the Istituto di Microelettronica e Microsistemi of the Consiglio Nazionale delle Ricerche (IMM-CNR) of Bologna (Italy) and at the Institut de Science et d'Ingénierie Supramoléculaires (ISIS) of Strasbourg (France).

Sommario

La necessità di produrre applicazioni dai costi contenuti, capaci di coprire grandi superfici e compatibili con substrati flessibili, ha guidato la comunità scientifica verso la progettazione di nuovi materiali organici caratterizzati da elevata solubilità in solventi comuni, buona stabilità in aria ed alta mobilità dei portatori di carica in transistori ad effetto di campo (OFETs), i mattoni dell' elettronica organica. Il successo di questa generazione di materiali π-coniugati è principalmente legato ai miglioramenti nella comprensione della fisica del legame struttura-proprietà nei materiali stessi. La microstruttura del materiale, ovvero la sua struttura cristallina, l'orientazione ed organizzazione delle molecole su di un substrato, la formazione di domini cristallini, nonché la presenza di disordine e difetti, ha infatti una forte influenza sul trasporto di carica nel corrispettivo OFET [15, 16]. Lo scopo di questa tesi è di chiarire la relazione tra le proprietà strutturali ed elettriche di materiali semiconduttori organici, piccole molecole e polimeri, caratterizzati da differenti gradi d'ordine cristallino. Gli OFETs possono essere fabbricati sfruttando una varietà d'architetture e materiali organici depositati sia mediante tecniche da soluzione, sia mediante sublimazione in ultra-alto vuoto. Grazie all'elevato grado d'ordine cristallino ed omogeneità, dispositivi basati su molecole organiche sublimate sono ampiamente studiati come sistemi-modello per la comprensione della fisica del dispositivo. I dispositivi fabbricati mediante processi di deposizione da soluzione, nonostante siano più attraenti per applicazioni a basso costo, presentano un basso ordine cristallino e l'indagine approfondita dei loro meccanismi di trasporto rappresenta ancora una sfida. In questa tesi sono stati adottati due approcci per investigare la relazione tra struttura e proprietà elettriche di alcuni materiali organici: caratterizzazione multipla ex-situ ed indagine strutturale in-situ in tempo reale.

La caratterizzazione ex-situ (strutturale, morfologica, elettrica, ottica, ecc) di un sistema è uno degli approcci più comuni in letteratura. In questa tesi è stata sfruttata per indagare OFETs basati su due derivati perilenici oltre che transistori ambipolari fabbricati depositando strati multipli di polimeri di tipo n e p mediante una particolare tecnica da soluzione.

Tra i semiconduttori organici di tipo n, sono stati scelti i derivati del perilene alkyldiimide (PDIs) per le loro buone prestazioni elettriche e l'ottima processabilità [25, 26]. In particolare sono stati studiati derivati del PDI il cui core è funzionalizzato con gruppi ciano che abbassano l'energia del più basso orbitale molecolare non occupato incrementando la stabilità in aria [27, 28] e con catene laterali in grado di aumentare la solubilità emigliorare quindi la processabilità. La presenza di di catene laterali influisce anche sul grado d'ordine molecolare del film e di conseguenza sull'efficienza del trasporto di carica nel materiale. OFETs basati su film sottili di derivati del PDI decorati con catene lineari (PDI8-CN2 - N,N'-bis(n-octyl)-dicyanoperylene-3,4:9,10-bis-dicarboximide) e ramificatie (N1400 - N,N'-bis-(2-ethylhexyl)-1,7-dicyano-perylene-3,4:9,10-bis(dicarboximide)) sono

stati studiati per stabilire il ruolo della forma delle catene alchiliche sulla struttura dei film sottili e di conseguenza sulle prestazioni elettriche del dispositivo. I risultati ottenuti dimostrano che l'introduzione di catene ramificate asimmetriche permette di ottenere, con un opportuno trattamento termico, OFETs con migliori prestazioni elettriche rispetto a quelle lineari. Il composto a catene ramificate è costituito da una miscela di quattro stereoisomeri, ovvero le due coppie enantiomeriche RR/SS e RS/SR, che sono presenti nel film ed inducono un disordine conformazionale da cui dipende la morfologia bidimensionale. Per queste molecole un trattamento termico ottimizzato a seguito della deposizione porta ad una transizione strutturale verso la fase di bulk, conservando la morfologia 2D e migliorando le proprietà di trasporto dei dispositivi. Al contrario, le molecole con catene alchiliche lineari auto-assemblano in isole 3D caratterizzate dalla fase bulk più stabile e mantengono le loro caratteristiche pressoché inalterate anche dopo il trattamento termico. Questi risultati mostrano come in un derivato del PDI la sostituzione di catene alchiliche lineari con catene asimmetriche ramificate possa essere una strategia efficace per ottenere, a seguito di un semplice trattamento termico, transistori ad effetto di campo con migliori proprietà di trasporto. Inoltre, questi risultati dimostrano che il disordine generato dalle catene asimmetriche ramificate quando la molecola viene fisisorbita su una superficie può essere decisivo per il miglioramento del trasporto di carica [29].

Il secondo studio ex-situ riguarda la caratterizzazione di OFETs ambipolari basati su più strati di polimeri di tipo n e p depositati mediante la tecnica Langmuir-Schaefer (LS). La produzione di OFETs ambipolari con mobilità elettrone-lacuna elevate e comparabili è attualmente un tema d'interesse a causa della loro potenziale applicazione in circuiti integrati organici. La possibilità di ottenere un trasporto simultaneo di entrambi i tipi di portatori porterebbe non solo ad una semplificazione nella progettazione di circuiti logici complementari, ma servirebbe anche a ridurre la dissipazione di potenza ed aumentare i margini di rumore dei dispositivi. La tecnica LS permette la fabbricazione di un dispositivo ambipolare mediante la deposizione consecutiva di entrambi gli strati n e p da soluzione. Questo metodo comporta la creazione di un monostrato di film per diffusione della soluzione all'interfaccia acqua-aria ed il trasferimento dello stesso su di un substrato solido [30]; la procedura può essere eseguita una volta sola, se un singolo monostrato è necessario oppure diverse volte se devono essere depositati strati multipli. Questa tecnica permette un controllo accurato dello spessore e la struttura dello starto depositato favorendo un forte impacchettamento molecolare nonchè ordine a lungo raggio. In generale, la mobilità dei portatori di carica in dispositivi polimerici è ridotta a causa dello scarso impacchettamento e mancanza di ordine indotto dalla conformazione del polimero stesso e dalla presenza di catene alchiliche lunghe che creano un rilevante ingombro sterico [31]. Rispetto ad altre tecniche di deposizione da soluzione, il metodo LS costringe il polimero ad impacchettarsi ed organizzarsi sulla superficie in una configurazione vantaggiosa per il trasporto di carica. In particolare per questo studio è stato scelto l' IIDDT-C3, un polimero π-coniugato di tipo p derivato dell'isoindigo, per le eccezionali prestazioni elettriche e buon ordine cristallino già ottenibile mediante deposizione dd spin-coating [32]. All'IIDDT-C3 è stato affiancato P(NDI2OD-T2) (o N2200), un eccezionale polimero commerciale di tipo n, che ha già dimostrato buone risposte elettriche in film sottili preparati sia per spin-coating che LS [33–36]. Dopo aver determinato le condizioni ottimali per la deposizione degli strati polimerici, singoli e multipli strati composti dalla sovrapposizione di N2200 e IIDDT-C3 (e viceversa) sono stati caratterizzati strutturalmente. La diffrazione da raggi X ad incidenza radente ha fornito le informazioni necessarie per comprendere l'effetto della tecnica di deposizione sull'ordine cristallino e l'impacchettamento molecolare degli strati organici. I singoli strati di entrambi i polimeri mostrato infatti un'organizzazione edge-on (rispetto alla superficie del substrato) delle lamelle polimeriche che viene mantenuta anche nelle architetture ambipolari e che ha permesso di raggiungere mobilità di elettroni (μe) e lacune (μh) dell'ordine di 10^{-1} cm^2/Vs in regime di saturazione. Inoltre, lo strato di IIDDT-C3 mostra un'organizzazione fibrillare indotta dalla tecnica di deposizione LS, ulteriormente dimostrato da immagini di microscopia a forza atomica (AFM).

L'approccio basato sull'indagine strutturale in-situ ed in tempo reale è il metodo più adatto per descrivere l'evoluzione strutturale di un sistema in situazioni di non equilibrio. Ciò implica che la caratterizzazione strutturale viene eseguita esattamente durante la risposta del sistema ad uno stimolo esterno. Nonostante l'enorme quantità di informazioni fisiche che possono fornire, questo approccio non è molto comune a causa della complessità sperimentale necessaria per seguire fenomeni che evolvono in scale di tempi molto ridotte. Questa strategia è stata sfruttata in questa tesi per studiare l'effetto del campo elettrico sulla struttura di film di pentacene durante il funzionamento del OFET e per seguire l'evoluzione strutturale di film sottili basati su derivati del TTF (tetrathiafulvalene) durante la variazione dell'umidità relativa nell'ambiente circostante.

Come già noto in letteratura [37–39], negli OFETs il trasporto di carica è fortemente influenzato dalla struttura e morfologia del film organico all'interfaccia con il dielettrico. Tuttavia, quale sia la risposta strutturale dello strato semiconduttivo all'applicazione del campo elettrico rappresenta ancora un quesito irrisolto. Misure di diffrazione da raggi X in-situ ed in tempo reale utilizzando una sorgente di radiazione di sincrotrone sono state quindi effettuate su OFETs di pentacene per investigare l'evoluzione strutturale del materiale organico durante l'applicazione simultanea del potenziale di gate (V_{SG}) e di source-drain (V_{SD}). OFETs con geometria bottom-gate top-contact specificatamente fabbricati per la realizzazione di misure raggi X all'interno del canale del dispositivo sono stati utilizzati. Con questa tecnica è stato possibile rivelare per la prima volta un'espansione reticolare del pentacene causata dall' inclinazione delle molecole (pochi mrad) a seguito dell'applicazione di V_{SG} e V_{SD}. Questo fenomeno è reversibile e supportato da simulazioni di dinamica molecolare e DFT.

Materiali organici derivati dei TTF sono ampiamente studiati per applicazioni sensoristiche [40–43]. I campioni costituiti da uno strato conduttore sottile su di una matrice polimerica sono stati forniti dal gruppo della Professoressa Rovira (ICMAB-CSIC, Spagna). Una camera per l'umidità adatta per effettuare misure di raggi X in simultanea con misure elettriche in atmosfera di umidità controllata è stata costruita e collocata sul goniometro del diffrattometro in laboratorio. Due finestre di kapton permettono al fascio di raggi X incidente di raggiungere il campione posizionato al centro della camera ed a quello scatterato di raggiungere il rilevatore. Questa configurazione ha consentito l'analisi di alcuni picchi caratteristici del materiale durante la variazione di umidità relativa (RH%) all'interno della camera monitorata da un termoigrometro. I risultati hanno dimostrato che la variazione di RH% influisce reversibilmente sulla struttura del film sottile: in particolare l'espansione reticolare correlata all'incremento di RH% suggerisce che le molecole d'acqua penetrano all'interno dei cristalliti modificandone i parametri reticolari.

In conclusione, in questa tesi vengono presentati esempi di multi-caratterizzazione ex-situ così come indagini strutturali in-situ ed in tempo reale su diversi materiali semiconduttori organici. In entrambi i casi, lo studio della stretta interconnessione tra proprietà strutturali, morfologiche ed elettriche dei sistemi ha portato ad una descrizione approfondita dei materiali stessi e dei dispositivi basati su di essi.

Questo manoscritto presenta i risultati di un dottorato di ricerca di 3 anni in cotutela tra l'Università di Ferrara e l'Università di Strasburgo con il supporto finanziario dell'Università Italo-Francese (Bando Vinci 2013). Il lavoro è stato svolto principalmente presso l'Istituto di Microelettronica e Microsistemi del Consiglio Nazionale delle Ricerche (IMM-CNR) di Bologna (Italia) e presso l'Istitut de Science et d'Ingénierie Supramoléculaires (ISIS) di Strasburgo (Francia).

Bibliography

[1] A. Tsumura, H. Koezuka and T. Ando. *Applied Physics Letters* **49(18)**, 1210–1212 (1986)

[2] T. Umeyama and H. Imahori. *Journal of Materials Chemistry A* **2(30)**, 11545–11560 (2014)

[3] S. Z. Bisri, T. Takenobu and Y. Iwasa. *Journal of Materials Chemistry C* **2(16)**, 2827–2836 (2014)

[4] A. Dodabalapur. *Materials Today* **9(4)**, 24–30 (2006)

[5] A. Facchetti. *Nature Materials* **12(7)**, 598–600 (2013)

[6] H. Sirringhaus. *Advanced Materials* **26(9)**, 1319–1335 (2014)

[7] C. Kim, A. Facchetti and T. J. Marks. *Science* **318(5847)**, 76–80 (2007)

[8] M. Novak, A. Ebel, T. Meyer-Friedrichsen, A. Jedaa, B. F. Vieweg, G. A. Yang, K. Voitchovsky, F. Stellacci, E. Spiecker, A. Hitsch and M. Halik. *Nano Letters* **11(1)**, 156–159 (2011)

[9] M. A. McCarthy, B. Liu, E. P. Donoghue, I. Kravchenko, D. Y. Kim, F. So and A. G. Rinzler. *Science* **332(6029)**, 570–573 (2011)

[10] M. E. Roberts, S. C. B. Mannsfeld, N. Queralto, C. Reese, J. Locklin, W. Knoll and Z. N. Bao. *Proceedings of the National Academy of Sciences of the United States of America* **105(34)**, 12134–12139 (2008)

[11] S. Colella, C. Ruzie, G. Schweicher, J. B. Arlin, J. Karpinska, Y. Geerts and P. Samori. *Chempluschem* **79(3)**, 371–374 (2014)

[12] S. Bauer, S. Bauer-Gogonea, I. Graz, M. Kaltenbrunner, C. Keplinger and R. Schwodiauer. *Advanced Materials* **26(1)**, 149–162 (2014)

[13] Y. H. Zheng and F. Wudl. *Journal of Materials Chemistry A* **2(1)**, 48–57 (2014)

[14] M. Cavallini, C. Albonetti and F. Biscarini. *Advanced Materials* **21(10-11)**, 1043–1053 (2009)

[15] A. Salleo, R. J. Kline, D. M. DeLongchamp and M. L. Chabinyc. *Advanced Materials* **22(34)**, 3812–3838 (2010)

[16] D. M. DeLongchamp, R. J. Kline, D. A. Fischer, L. J. Richter and M. F. Toney. *Advanced Materials* **23(3)**, 319–337 (2011)

[17] Z. Bao and J. Locklin. Organic Field Effect Transistors (CRC Press, 2007), 1st ed. edition

[18] C. Woll. Physical and Chemical Aspects of Organic Electronics (Wiley-VHC, Weinheim, 2009)

[19] G. De Luca, E. Treossi, A. Liscio, J. M. Mativetsky, L. M. Scolaro, V. Palermo and P. Samori. *Journal of Materials Chemistry* **20(13)**, 2493–2498 (2010)

[20] A. Liscio, V. Palermo, D. Gentilini, F. Nolde, K. Mullen and P. Samori. *Advanced Functional Materials* **16(11)**, 1407–1416 (2006)

[21] J. E. Anthony, A. Facchetti, M. Heeney, S. R. Marder and X. W. Zhan. *Advanced Materials* **22(34)**, 3876–3892 (2010)

[22] A. Dodabalapur. *Nature* **434(7030)**, 151–152 (2005)

[23] H. Yan, Y. Zheng, R. Blache, C. Newman, S. F. Lu, J. Woerle and A. Facchetti. *Advanced Materials* **20(18)**, 3393–+ (2008)

[24] B. Yoo, T. Jung, D. Basu, A. Dodabalapur, B. A. Jones, A. Facchetti, M. R. Wasielewski and T. J. Marks. *Applied Physics Letters* **88(8)** (2006)

[25] F. Liscio, S. Milita, C. Albonetti, P. D'Angelo, A. Guagliardi, N. Masciocchi, R. G. Della Valle, E. Venuti, A. Brillante and F. Biscarini. *Advanced Functional Materials* **22(5)**, 943–953 (2012)

[26] J. Soeda, T. Uemura, Y. Mizuno, A. Nakao, Y. Nakazawa, A. Facchetti and J. Takeya. *Advanced Materials* **23(32)**, 3681–+ (2011)

[27] R. C. Savage, E. Orgiu, J. M. Mativetsky, W. Pisula, T. Schnitzler, C. L. Eversloh, C. Li, K. Mullen and P. Samori. *Nanoscale* **4(7)**, 2387–2393 (2012)

[28] C. Piliego, F. Cordella, D. Jarzab, S. Lu, Z. Chen, A. Facchetti and M. A. Loi. *Applied Physics a-Materials Science & Processing* **95(1)**, 303–308 (2009)

[29] L. Ferlauto, F. Liscio, E. Orgiu, N. Masciocchi, A. Guagliardi, F. Biscarini, P. Samori and S. Milita. *Advanced Functional Materials* **24(35)**, 5503–5510 (2014)

[30] K. Blodgett. *Journal of American Chemical Society* **57**, 1007–1022 (1935)

[31] Y. Zhao, Y. L. Guo and Y. Q. Liu. *Advanced Materials* **25(38)**, 5372–5391 (2013)

[32] T. Lei, J. H. Dou and J. Pei. *Advanced Materials* **24(48)**, 6457–6461 (2012)

[33] H. Yan, Z. H. Chen, Y. Zheng, C. Newman, J. R. Quinn, F. Dotz, M. Kastler and A. Facchetti. *Nature* **457(7230)**, 679–U1 (2009)

[34] J. Rivnay, M. F. Toney, Y. Zheng, I. V. Kauvar, Z. H. Chen, V. Wagner, A. Facchetti and A. Salleo. *Advanced Materials* **22(39)**, 4359–+ (2010)

[35] S. Fabiano, C. Musumeci, Z. H. Chen, A. Scandurra, H. Wang, Y. L. Loo, A. Facchetti and B. Pignataro. *Advanced Materials* **24(7)**, 951–+ (2012)

[36] J. Rivnay, R. Steyrleuthner, L. H. Jimison, A. Casadei, Z. H. Chen, M. F. Toney, A. Facchetti, D. Neher and A. Salleo. *Macromolecules* **44(13)**, 5246–5255 (2011)

[37] A. Shehu, S. D. Quiroga, P. D'Angelo, C. Albonetti, F. Borgatti, M. Murgia, A. Scorzoni, P. Stoliar and F. Biscarini. *Physical Review Letters* **104(24)**, 246602 (2010)

[38] J. Rivnay, L. H. Jimison, J. E. Northrup, M. F. Toney, R. Noriega, S. F. Lu, T. J. Marks, A. Facchetti and A. Salleo. *Nature Materials* **8(12)**, 952–958 (2009)

[39] F. Liscio, C. Albonetti, K. Broch, A. Shehu, S. D. Quiroga, L. Ferlauto, C. Frank, S. Kowarik, R. Nervo, A. Gerlach, S. Milita, F. Schreibers and F. Biscarini. *Acs Nano* **7(2)**, 1257–1264 (2013)

[40] M. Mas-Torrent and C. Rovira. *Journal of Materials Chemistry* **16(5)**, 433–436 (2006)

[41] E. Laukhina, R. Pfattner, L. R. Ferreras, S. Galli, M. Mas-Torrent, N. Masciocchi, V. Laukhin, C. Rovira and J. Veciana. *Advanced Materials* **21**, 1–5 (2009)

[42] E. Laukhina, R. Pfattner, L. R. Ferreras, S. Galli, M. Mas-Torrent, N. Masciocchi, V. Laukhin, C. Rovira and J. Veciana. *Advanced Materials* **22(9)**, 977–+ (2010)

[43] L. R. Ferreras, R. Pfattner, M. Mas-Torrent, E. Laukhina, L. Lopez, V. Laukhin, C. Rovira and J. Veciana. *Journal of Materials Chemistry* **21(3)**, 637–640 (2011)

INTRODUCTION

The first report on an organic semiconductor (OSs) acting as active layer in a field-effect transistor is dated back to the 1986 [1]. From then on, OSs have gained more and more attention especially because of their versatility in material design that offers countless possibilities in building molecules with ad-hoc electronic properties suitable for various electronic devices, such as organic light emitting diodes (OLEDs), solar cells for organic photovoltaics (OPVs) [2], organic field-effect transistors (OFETs) and organic light emitting transistors (OLETs) [3]. The researchers' efforts and results have guided the transition of these devices from scientific curiosities to potentially important technologies for consumer electronics [4]. Their chemical tunabilty [5] coupled with the possibility of exploiting fast and inexpensive processing methods represents the main attractive feature for the idealization of a novel generation of low-cost and light-weight electronics based on printable and flexible devices [6–11]. Nowadays, for example, OSs are employed for the fabrication of various types of sensors, including robotic skin sensors [12], and they are also entering in the spintronic field [13]. The key to reach this goal is to synthesize OSs exhibiting high solubility in common solvents (to be easily processed) and high charge carriers mobility together with stability in air and during operational conditions [14]. Some OSs have already entered in the marketplace, for example as active layers in OLEDs used in TVs, displays and smartphones, but a lot in terms of environmental stability has still to be done especially regarding electron-transporting (n-type) OSs. Differently from their counterpart (p-type OSs), n-type organic materials are more sensitive to the environmental conditions and thus less stable. Despite the stability challenge, n-type OSs are essential for the developement of a complementary electronics that will enable to combine flexible substrates with restrained power consumptions [15–18].

Among the many factors influencing the behavior of an organic device, such as the device geometry, the type and thickness of the dielectric and the electrodes and the intrinsic properties of the organic material, the organization of the molecules on the substrate surface is certainly one of the most challenging. From the interactions between π-conjugated molecular cores, i.e. from the extent of molecular order in the bulk material [19], depends in fact the charge transfer between molecules. On the other hands, the intermolecular interactions also govern the solubility of the material influencing its processability. As a consequence, the structural order at the supramolecular level, the processing and the device performance result strongly intertwined [20–22].

The aim of this thesis is to contribute to the comprehension of the organic devices based on n-type and p-type small molecules and polymers by relating the structural and morphological features of the active films with the physical properties of the devices. Different approaches are exploited to face the challenge, including standard ex-situ structural methods and more complicated and unconventional in-situ and real-time ones.

An introduction on the generalities of OSs including the main charge transport methods known so far and a description of the OFETs operation principles, as well as the principal factors influencing their performance, is given in **Chapter 1**.
In **Chapter 2** the main techniques exploited for the fabrication and characterization of the material studied are described. Particular care was dedicated to the structural characterization techniques that include standard laboratory as well as synchrotron based X-rays measurements.
The results on the first multi-technique study are presented in **Chapter 3**. OFETs based on perylene derivatives isomers differentiated just by the shape of the lateral alkyl chains and deposited from solution were structurally, morphologically and electrically characterized. The results indicate how the capability of supramolecular organization on a surface and the charge transport can be affected by the introduction of chemical (structural) modifications.
Chapter 4 illustrates for the first time the fabrication and characterization of bilayer ambipolar devices based on solution processed polymeric active layers. In this case the deposition technique utilized imposes an orientation of the polymeric chains which results suitable for obtaining remarkable electrical performance.
Chapter 5 tackles and answers to a fundamental and unsolved question about OFETs. In this study a well known organic material (pentacene) was vacuum sublimated on the substrate and the device geometry was not optimized to obtain astonishing performance. The goal of the work was in fact to detect the effect of the electric field on the structure of the active layer of an OFET during the operation of the OFET itself. For this project an unconventional in-situ and real-time structural characterization based on synchrotron radiation was exploited.
Chapter 6 describes the preliminar results on the in-situ and real-time structural investigation of flexible thin films sensitive to the humidity variation. For this study, an adhoc experimental setup, which allows performing simultaneous structural and electrical measurements in a controlled atmosphere, was built. In this case a laboratory X-ray source was exploited and the preliminar results obtained pointed out the limits as well as the potentialities of the setup. Further optimizations to the apparatus need to be done in order to proceed with the project. Only in this case the organic thin films characterized were provided by the group of Prof. Rovira of the Institut de Ciéncia de Materials de Barcelona of the Consejo Superior de Investigaciones Cientifica (ICMAB-CSIC) (Spain).
The main conclusions for each single study presented, as well as the outlooks for future projects are summarized in the last chapter, **Chapther 7**.

Bibliography

[1] A. Tsumura, H. Koezuka and T. Ando. *Applied Physics Letters* **49(18)**, 1210–1212 (1986)

[2] T. Umeyama and H. Imahori. *Journal of Materials Chemistry A* **2(30)**, 11545–11560 (2014)

[3] S. Z. Bisri, T. Takenobu and Y. Iwasa. *Journal of Materials Chemistry C* **2(16)**, 2827–2836 (2014)

[4] A. Dodabalapur. *Materials Today* **9(4)**, 24–30 (2006)

[5] A. Facchetti. *Nature Materials* **12(7)**, 598–600 (2013)

[6] H. Sirringhaus. *Advanced Materials* **26(9)**, 1319–1335 (2014)

[7] C. Kim, A. Facchetti and T. J. Marks. *Science* **318(5847)**, 76–80 (2007)

[8] M. Novak, A. Ebel, T. Meyer-Friedrichsen, A. Jedaa, B. F. Vieweg, G. A. Yang, K. Voitchovsky, F. Stellacci, E. Spiecker, A. Hitsch and M. Halik. *Nano Letters* **11(1)**, 156–159 (2011)

[9] M. A. McCarthy, B. Liu, E. P. Donoghue, I. Kravchenko, D. Y. Kim, F. So and A. G. Rinzler. *Science* **332(6029)**, 570–573 (2011)

[10] M. E. Roberts, S. C. B. Mannsfeld, N. Queralto, C. Reese, J. Locklin, W. Knoll and Z. N. Bao. *Proceedings of the National Academy of Sciences of the United States of America* **105(34)**, 12134–12139 (2008)

[11] S. Colella, C. Ruzie, G. Schweicher, J. B. Arlin, J. Karpinska, Y. Geerts and P. Samori. *Chempluschem* **79(3)**, 371–374 (2014)

[12] S. Bauer, S. Bauer-Gogonea, I. Graz, M. Kaltenbrunner, C. Keplinger and R. Schwodiauer. *Advanced Materials* **26(1)**, 149–162 (2014)

[13] Y. H. Zheng and F. Wudl. *Journal of Materials Chemistry A* **2(1)**, 48–57 (2014)

[14] M. Cavallini, C. Albonetti and F. Biscarini. *Advanced Materials* **21(10-11)**, 1043–1053 (2009)

[15] J. E. Anthony, A. Facchetti, M. Heeney, S. R. Marder and X. W. Zhan. *Advanced Materials* **22(34)**, 3876–3892 (2010)

[16] A. Dodabalapur. *Nature* **434(7030)**, 151–152 (2005)

[17] H. Yan, Y. Zheng, R. Blache, C. Newman, S. F. Lu, J. Woerle and A. Facchetti. *Advanced Materials* **20(18)**, 3393–+ (2008)

[18] B. Yoo, T. Jung, D. Basu, A. Dodabalapur, B. A. Jones, A. Facchetti, M. R. Wasielewski and T. J. Marks. *Applied Physics Letters* **88(8)** (2006)

[19] Z. Bao and J. Locklin. Organic Field Effect Transistors (CRC Press, 2007), 1st ed. edition

[20] C. Woll. Physical and Chemical Aspects of Organic Electronics (Wiley-VHC, Weinheim, 2009)

[21] G. De Luca, E. Treossi, A. Liscio, J. M. Mativetsky, L. M. Scolaro, V. Palermo and P. Samori. *Journal of Materials Chemistry* **20(13)**, 2493–2498 (2010)

[22] A. Liscio, V. Palermo, D. Gentilini, F. Nolde, K. Mullen and P. Samori. *Advanced Functional Materials* **16(11)**, 1407–1416 (2006)

CHAPTER 1

CHARGE TRANSPORT PROPERTIES IN ORGANIC SEMICONDUCTING MATERIALS

1.1 Organic semiconductors

Organic semiconducting materials are principally composed by carbon atoms, together with oxygen and hydrogen atoms. The presence of single, double or triple carbon-carbon bonds depending on the hybridization, is the origin of these materials versatility. As visualized in Figure 1.1a, in the ground state the electron configuration of the carbon atom has four valence electrodes. The two electrons in the inner shell ($1s^2$) are core electrons, so they do not participate to the bonding process, whereas the other electrons (two in the $2s^2$ and other two in the $2p^2$ sub-shells) are valence electrons and play an active role in the formation of bonds. In order to have 4 possible bonds instead of simply 2, the carbon atom promotes one electron from the *s* shell to the *p* shell (Figure 1.1b).

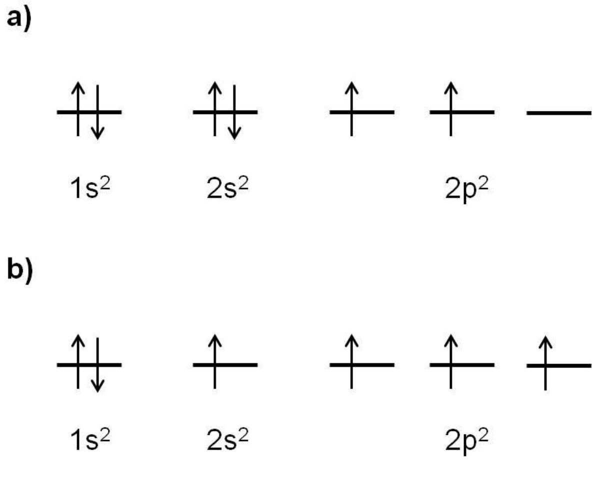

Figure 1.1: Electronic configuration of a carbon atom a) in the ground state and b) in the excited state.

The formation of this excited state gives rise to new atomic orbitals (AOs) deriving from the combination of *s* and *p* ones. This process is called *hybridization* because it involves the merging of the spherical *s* orbital with the elongated *p* orbital to create new AOs (Figure 1.2). AOs are functions that describe the quantum states of electrons. The bigger lobe of the hybridized AO is the one which most probably contains the unpaired valence electron. Depending on how many orbitals are mixed, there will be different kind of hybridizations.

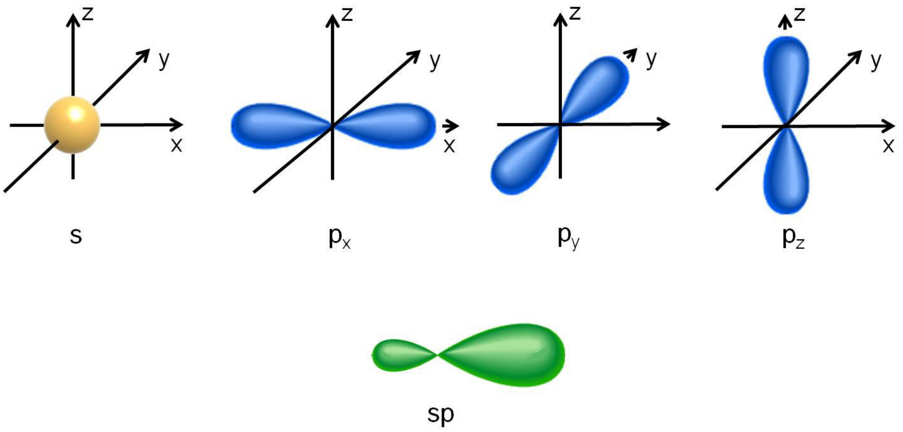

Figure 1.2: Representation of the spherical *s*, of the three elongated *p* and of the hybridized *sp* atomic orbitals.

1.1.1 sp^3 hybridization

The mixing of the *s* orbital with all the three *p* orbitals leads to the formation of four sp^3 hybridized orbitals which arrange in a tetrahedral geometry to maximize the distance between the charges (Figure 1.3). Each sp^3 orbital in fact contains one unpaired electron and it is thus available for a covalent bond.

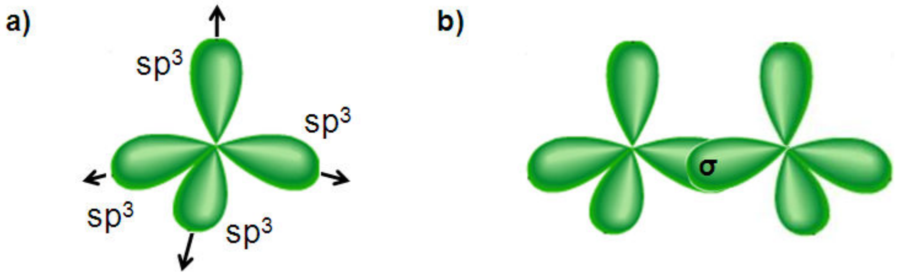

Figure 1.3: a) Representation of the tetragonal arrangement of four sp^3 hybridized AOs; b) sketch of a single carbon-carbon bond.

1.1.2 sp^2 hybridization

When the mixing includes the *s* orbital and two *p* orbitals, there is the formation of three sp^2 hybridized orbitals, which arrange in a planar triangular geometry perpendicularly crossed by the only left pure *p* orbital (Figure 1.4a). In a bond with another hybridized carbon atom, the head-to-head overlap between two sp^2 orbitals forms a σ bond, whereas the side-by-side overlap between two pure *p* orbitals forms a π bond (Figure 1.4b). The presence of a double bond connecting the carbon atoms arises from the constitution of these σ and π bonds (C=C).

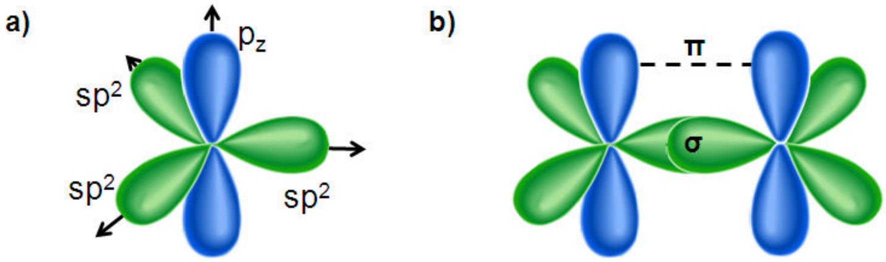

Figure 1.4: a) Representation of the planar arrangement of three sp^2 hybridized AOs; b) sketch of a double carbon-carbon bond.

1.1.3 *sp* hybridization

If instead the *s* orbital is merged with only one *p* orbital there is the formation of two *sp* hybridized orbitals which arrange in a linear configuration; the other two pure *p* orbitals dispose perpendicularly with respect to each other and to the two *sp* AO.

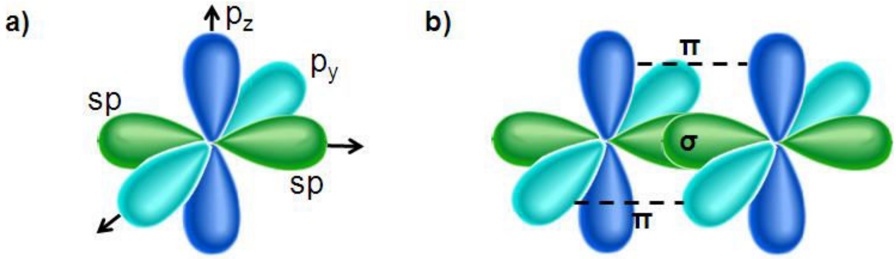

Figure 1.5: a) Representation of the linear arrangement of two *sp* hybridized AOs; b) sketch of a triple carbon-carbon bond.

In a bond with another *sp* hybridized carbon atom, the head-to-head overlap between two *sp* orbitals forms a σ bond, whereas the side-by-side overlap between the two pure *p* orbitals forms two π bonds. These two π bonds together with the σ one are responsible for the triple bond between the adjacent carbon atoms (C≡C).

Organic semiconducting materials are π-conjugated materials, due to the presence of alternating single-multiple carbon-carbon bonds. This allows for the overlapping of p AOs and consequently to the delocalization of π electrons throughout the extended system. According to the molecular orbitals (MOs) theory, the wave function Ψ describing a valence electron in a molecule is characterized by quantum numbers depending on the form and energy of the AOs (ψ) involved. This Ψ can be approximated as a linear combination of AO (LCAO), resulting in:

$$\Psi = \sum_n c_n \psi_n \tag{1.1}$$

If two atoms form a molecule, their AOs can combine in two ways:

$$\Psi = c_A \psi_A + c_B \psi_B \tag{1.2}$$

$$\Psi^* = c_A \psi_A - c_B \psi_B \tag{1.3}$$

The molecular orbital resulting from the first case is called (π) bonding MO (or highest occupied molecular orbital, HOMO), while the other one (π*) antibonding MO (or lowest unoccupied molecular orbital, LUMO). In general the number of MO is equal to the valence AOs. If the number of atoms forming the molecule increases, the HOMO and LUMO orbitals transform into valence and conduction bands containing the energy levels depending on the wave number *k*.

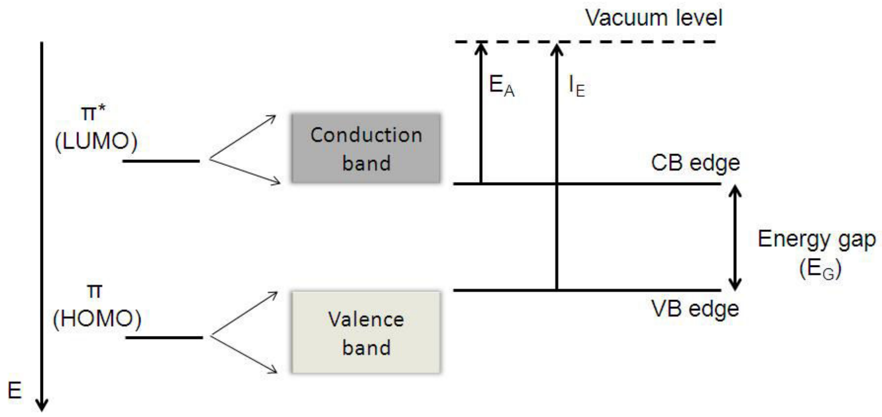

Figure 1.6: Band structure of an organic semiconductor deriving from the superposition of many bonding and antibonding molecular orbitals.

In organic materials, the greater the number of conjugated π-bonds, the smaller the π-π* (i.e. HOMO-LUMO) energy difference is, in such a way that the absorption of electromagnetic radiation in the UV-visible range or simply the thermal energy can promote electrons from the HOMO to the LUMO level.

Organic semiconductors are mainly classified into two big classes: small molecules and polymers. Both classes comprise materials which show conduction of holes (p-type) and other which show conduction of electrons (n-type). Here just a brief list of the most common small molecules and polymers is presented; more detailed information can be found in different reviews [1–6].

1.1.4 Small molecules

Organic small molecules are characterized by low molecular weight and are not prone to polymerization. They can easily be deposited via thermal evaporation, which ensures purification of the material at the expenses of cost and ease of processing, as well as from solution if properly functionalized. Due to their small size and fixed shape, they usually well organize on a surface and tend to form well-defined crystalline films. One of the most popular p-type small molecules in literature is pentacene, from the acenes family, that is composed by five benzene rings attached together. It strongly organizes in a herringbone structure forming polychristalline films with good holes mobility and stability but it is not soluble, so it can only be deposited by vacuum processes. To overcome the solubility issue, a functionalized pentacene (TIPS-PEN) has been synthesized by Anthony and co-workers [7] and mobilities up to 1 cm^2/Vs were obtained by Payne and co-workers [8]. Other popular families of p-type organic small molecule for OFETs applications are the oligothiophenes [9, 10] and the tetrathiafulvalene (TTF) derivatives. Among oligothiophenes, sexithiophene (6T) is one of the most studied in literature [11]. TTF derivatives have been extensively studied by Rovira and co-workers [12, 13] and show a wide variety of applications as well as good electrical behaviour in OFETs. Examples of the most performing n-type semiconducting molecules known in literature are fullerene (C60) [14, 15], and rylenes [16, 17] derivatives. The latter ones are polycyclic aromatic electron-transport materials with high electron affinities and among these, many naphtalene and perylene diimides derivatives (respectively NDIs and PDIs) have shown high electron mobility as well as good thermal and photochemical stability. Moreover, the possibility of functionalization with cyano and alkyl groups makes these materials optimal for solution process depositions.

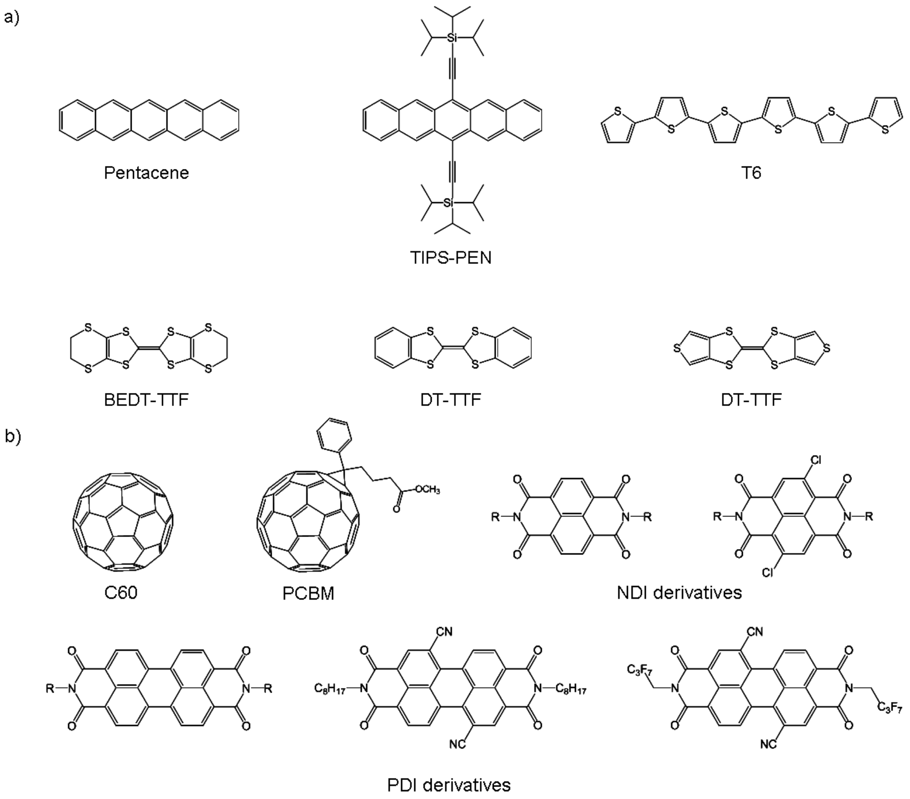

Figure 1.7: Examples of a) p-type and b) n-type small molecules.

1.1.5 Polymers

Conjugated polymers are composed of alternating single and double carbon bonds. Typically, they are characterized by a rigid π-conjugated backbone, where the charges are delocalized, and flexible insulating side-chains. The backbone represents the main pathway for charge transport which is then defined as intra-chain transport, while the side-chains hinder the intermolecular attractions making the material soluble and highly processable. Very often polymers organize on a surface in chains formed by repetitive units (or lamella) and the lamella of neighbouring chains can undergo partial π-orbitals overlap thus favouring charge transfer from one chain to the other (inter-chain transport). Polymers are much unwieldy than small molecules and have difficulty in packing and rearranging; they tend to form relatively small crystalline domains with large population of defects. Their large polydispersivity, i.e. the size of the molecular weight distribution's width, influences the formation of defects [18]. Poly(3-hexyl-thiophene) (P3HT) and poly(2,5-bis(3-alkylthiophen-2-yl)thieno[3,2-b]-Thiophene (PBTTT) are two of the most famous p-type polymers [19, 20]. Already in 1999 P3HT showed mobility values greater than 0.1 cm^2/Vs [21] and nowadays is employed for the fabrication and study of solar cells, and sensors [22]. Among the n-type polymers, poly[N,N′-bis(2-octyldodecyl)-naphtalene-1,4,5,8-bis(dicarboximide)-2,6-diyl]-alt-5,5′-(2,2′-bithiophene) (P(NDI2OD-T2)) is up to date one of the most widely studied for electronic applications, due to its outstanding electrical properties related to an unconventional face-on molecular packing [23].

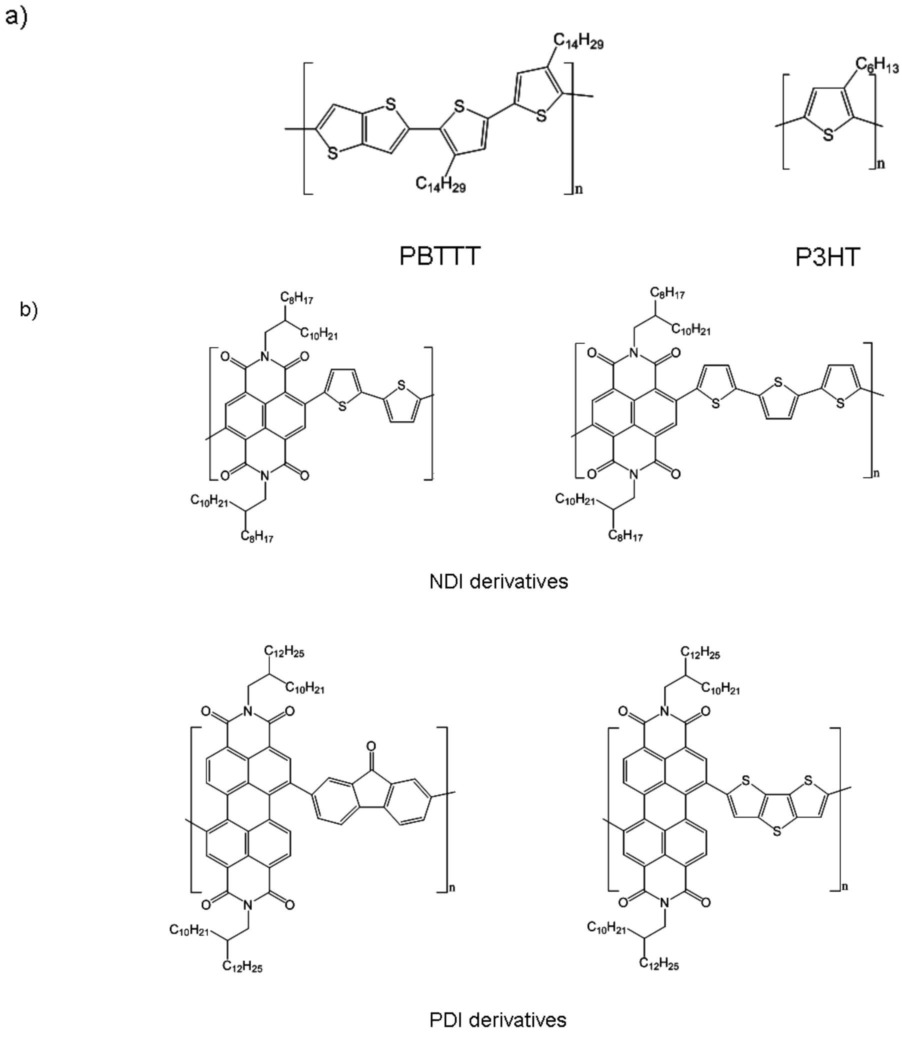

Figure 1.8: Examples of a) p-type and b) n-type organic plymers.

The predominance of publications regarding organic p-type materials is due to the ease of obtaining stable and performing devices based on p-type organics with respect to n-type ones. The main issues with n-type materials are: i) the big energy barrier between the electrode work function and the LUMO level of the molecule, ii) their high susceptibility to water and oxygen, iii) the electron trapping at the dielectric interface. To make transistors that carry electrons the LUMO level of the molecules needs to match the electrode work function so that charge injection from the metal contact to the organic semiconducting material becomes possible. The LUMO level must usually be lowered (i.e. the electron affinity increased) to match the work function of the gold and this can be achieved by adding strong electron withdrawing groups like fluorines, cyanos or diimides to the molecular core. The lowering of the LUMO also improves the air stability of the material by decreasing the trapping of charge carriers from H_2O or O_2. Another detrimental mechanism of charge trapping is the one happening at the dielectric surface. The most common dielectric used is the thermally grown SiO_2 which presents hydroxyl groups (OH) on the surface; these groups act as traps for the electrons, so the passivation of the surface by means of self-assembled monolayers (SAM) is an obliged step.

1.2 Charge transport models

Due to the wide variety of small molecules and polymers available, many models have been proposed to describe charge transport in conjugated materials, but a lot of work has still to be done to formulate a complete and consistent theory. In this section, a brief review of the origin of charge transport in inorganic materials [24–26] is recalled before introducing the main theories developed for organic materials [27–30]. It is in fact important to note that the main difference on transport mechanisms between inorganics and organics arises from the presence or absence of long-range crystalline order.

1.2.1 Inorganic materials: nearly free-electron model

The nearly free-electron model is an evolution of the quantum free electron model, which describes the motion of electrons in a metal by combining the classical Drude theory of motion and the quantum Fermi-Dirac statistics. To predict the presence of forbidden bands, and thus find an explanation for inorganic isolating and semiconducting materials, an important consideration has to be made: the electrons are nearly free, in the sense that they are slightly perturbed by the weak periodic potential deriving from the presence of atoms in the crystal lattice. The shape of the potential determines the exact solution of the Schröedinger equation for an electron in a crystal lattice, while the periodicity of the perturbation, i.e the presence of the lattice itself, gives the general shape of the nearly free-electron eigenfunction. This eigenfunction (Ψ) results in fact as a wave function whose amplitude is periodically modulated by the effective periodicity of the lattice

$$\Psi(x,t) = u_k(x)e^{i(kx-\omega t)} \tag{1.4}$$

with

$$u_k(x) = u_k(x+a) = u_k(x+na) \tag{1.5}$$

being *a* the the space periodicity of the lattice. Following the Kronig-Penney model, we can approximate the crystal potential in 1D ($V(x)$) as an array of rectangular potential wells and barriers reproducing the presence of the atoms. For wells that are close together, the eigenfunctions can penetrate the potential barriers and spread each single energy level (localized level) into a band (system of delocalized levels). Solving the Schröedinger equation within the Kronig-Penney model means to impose appropriate boundary conditions to Ψ; this restricts the energy solutions into allowed regions, which in turns give rise to the allowed bands. For energy values in the forbidden regions, i.e bands, the eigenfunctions decay exponentially. Thus the plot of energy as a function of the wave number *k* shows discontinuities occurring at particular *k* values:

$$k = \pm\frac{\pi}{a}, \pm\frac{2\pi}{a}, \pm\frac{3\pi}{a}, ... \tag{1.6}$$

with a always being the lattice periodicity in one direction. Each allowed band corresponds to solutions of the Schröedinger equation.

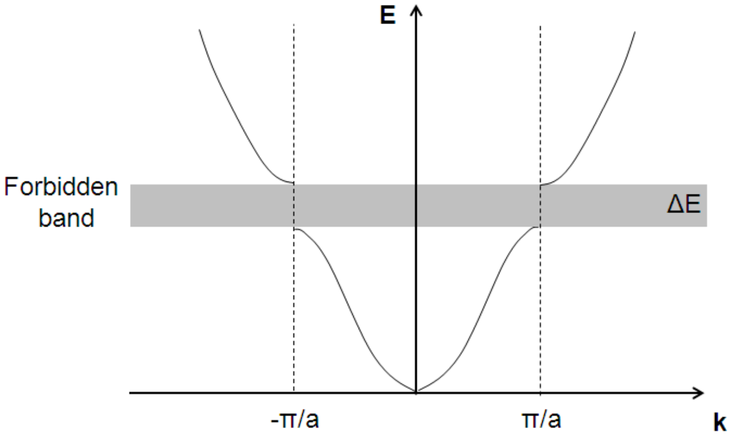

Figure 1.9: Energy behaviour as a function of the wave number **k**.

In inorganic semiconducting materials, there are two important bands to take into account, named *valence* and *conduction* bands, separated by a forbidden region of few eV, i.e. energy gap. The first one is filled with electrons while the second one is empty; thermal or optical excitations can promote charges from the valence to the conduction band allowing conductivity to take place under the application of an external electric field.

1.2.2 Organic materials: polarons

Organic semiconducting materials are characterized by less crystalline order with respect to their inorganic counterparts and the nearly free-electron model is no longer applicable; in particular the lack of long range periodicity forces the conduction to take place through thermal-activated hopping between localized energy levels [31]. Moreover, charge carriers in conjugated materials are of polaronic nature. *Polarons* are quasi-particles deriving from the electron-phonon coupling (or local coupling), i.e. interaction between electrons and quantized modes of vibrational energy arising from atoms' oscillations in the crystal (*phonons*). The charge carrier mobility of an organic material strongly depends on the electron-phonon coupling, other than on the electronic and phononic bandwidth and phonon energy. For weak local coupling the mobility displays bandlike temperature dependence ($\mu \propto T^{-n}$) in the whole range of temperatures. On the other hand, strong local couplings lead to three temperature dependent regimes:

- at low temperature the effect is similar to the case of weak local coupling, so the bandlike model is dominant;
- as the temperature increases, hopping becomes predominant;
- at high temperature the mobility decreases due to polarons dissociation and consequent charge scattering by thermal phonons.

In polymers the presence of high disorder usually hinders the polarons effect, so the charge transport results heavily affected by the nonlocal coupling, i.e. the modulation of the charge transport between adjacent sites (transfer integrals) by lattice phonons. This interaction is at the basis of a spontaneous symmetry breaking known as Peierls distortion [32, 33]. This effect is responsible for the occurrence of an alternation of the carbon-carbon bond lengths of the polyacetylene which ultimately leads to the opening of an energy gap [34].

1.2.2.1 Hopping model

The hopping model [35] assumes that in the presence of a large number of available hopping states (homogeneous distribution of density of states - DOS) at low temperature a carrier would hop to a distant site with energy comparable to the starting site rather than hopping to a close site with higher energy. In this picture, the material's conductivity depends exponentially on the temperature according to the relation:

$$\sigma = \sigma_0 exp[-(\frac{T_0}{T})^{\frac{1}{4}}] \tag{1.7}$$

with σ_0 and T_0 constants. Due to the lacking of long range order, in organic materials the DOS is assumed to be a Gaussian or an exponential function which depends on the electric field E and on the gate bias V_{SG} (see section 1.2) other than on temperature. The general field-dependence of the charge carrier mobility in organics is described by the Poole-Frenkel law:

$$\mu(E) = \mu(0) exp[\frac{q}{kT}\beta\sqrt{E}] \tag{1.8}$$

where $mu(0)$ is the mobility at zero electric field and β is the Poole-Frenkel factor:

$$\beta = \sqrt{\frac{q}{\pi\epsilon\epsilon_0}} \tag{1.9}$$

The dependence on the gate bias (V_{SG}) is related to the occupancy of the tail states of the Gaussian (or exponential) DOS. By the application of a gate bias, the accumulation of charges will fill up the lower states of the DOS; by the application of a higher gate bias, also states at higher energy will be occupied. This will favor the hopping from one site to another and thus improve the mobility.

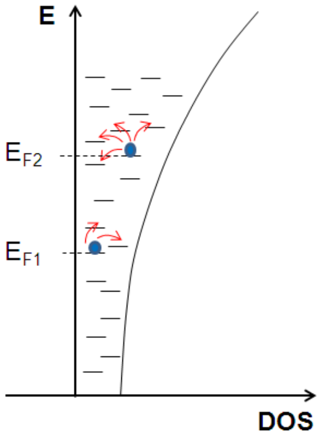

Figure 1.10: Representation of the gate-dependent charge carrier mobility. The Fermi level (E_F) increases due to the accumulation of more charges, i.e. to the increment of V_{SG}.

1.2.2.2 Variable range hopping model

Following the considerations for the simple hopping model, Vissenberg and Matters [36] developed a percolation variable range hopping (VRH) model primarily intended to apply to the study of the temperature dependence of charge transport in amorphous polymers and based on an exponential DOS. The calculated field-effect mobility results:

$$\mu = \frac{\sigma_0}{e} \left[\frac{(\frac{T_0}{T})^4 \sin(\frac{\pi T_0}{T})}{(2a)^3 B_c} \right]^{\frac{T_0}{T}} p^{\frac{T_0}{T}-1} \tag{1.10}$$

where σ_0 is the conductivity prefactor, a is the wavefunction overlap parameter between localized states, B_c is the critical value for percolation onset (~2.8), T_0 is the DOS width and p is the carrier concentration. Essentially in this model the mobility is governed by the DOS width and the overlap parameter.

1.2.2.3 Multiple trapping and release model

Multiple trapping and release model (MTR) was developed to describe the charge transport in amorphous silicon, but it turned out to be appropriate also for well-ordered organic materials such as polychrystalline organic films. It describes the charge transport occurring in materials characterized by highly conducting regions as well as local structural disorder (i.e defects and grain-boundaries). The baseline of the model is the assumption of a DOS divided in localized states below a band edge and a narrow band of delocalized states above the band edge: charge carriers traveling in the band are instantaneously trapped in the localized levels and subsequently thermally released.

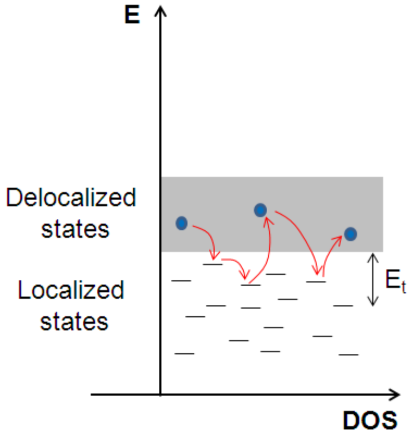

Figure 1.11: Representation of the MTR model. The charges in the delocalized states are trapped in localized states and subsequently deleased.

If the traps are homogeneously distributed, like in the case of polychrystalline films with a morphology characterized by relatively small grain size [37], the drift mobility μ_D resulting from the application of an external electric field is related to the mobility in the delocalized states μ_0 by the relationship:

$$\mu_D = \mu_0 \alpha e^{-\frac{E_t}{kT}} \tag{1.11}$$

where E_t is the energy gap between the trap state and the band edge and α is the ratio between the density of delocalized levels available for transport and the density of traps.

1.3 Organic field-effect transistors

Organic field-effect transistors (OFETs) are three terminal devices (source, drain and gate) with an organic semiconducting material as active layer and a dielectric which separates the gate electrode from the semiconductor [38]. The source electrode is usually grounded and the distance between source and drain is characterized by a width (W) and a length (L) defining the channel for charge transport.

Many configurations are possible, depending on the relative position of the three electrodes with respect to the organic semiconducting layer (Figure 1.13). During this thesis only two of them were exploited for the fabrication of organic devices: bottom gate-bottom contacts (BG-BC) and bottom gate-top contacts (BG-TC). In the first case source

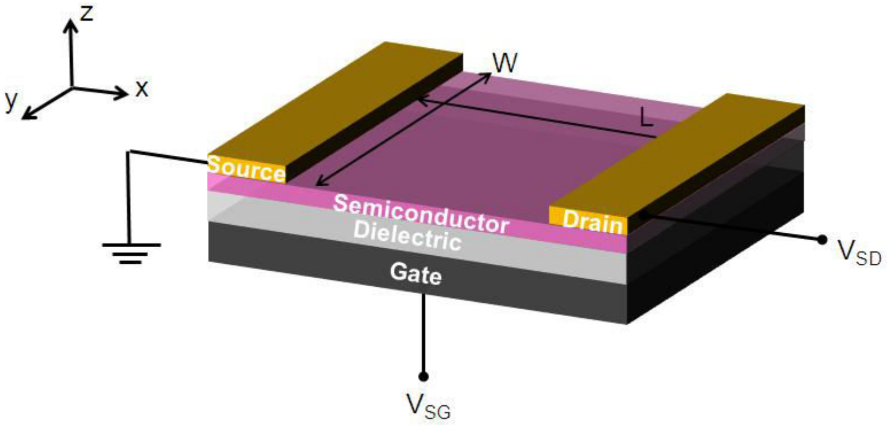

Figure 1.12: Sketch of an organic field-effect transistor (OFET).

and drain contacts are patterned directly on the dielectric layer and the deposition of the semiconducting material occurs on top of them, whereas in the second case the electrodes are thermally evaporated on top of the organic semiconductor.

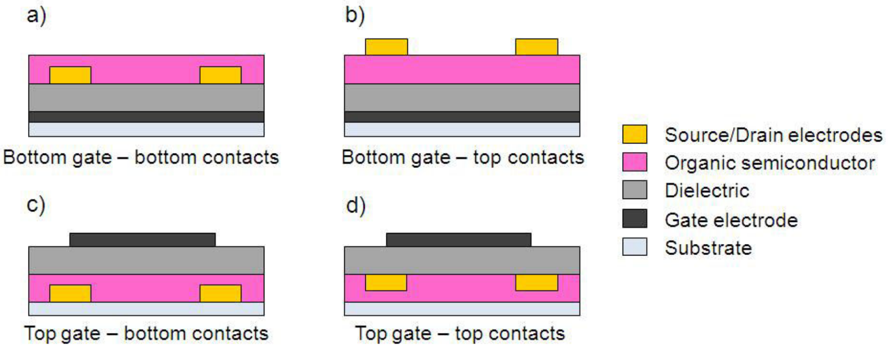

Figure 1.13: Different geometries of OFETs.

OFETs operate in accumulation regime. When a bias is applied to the gate (V_{SG}), an electric field perpendicularly crossing the dielectric is created; this field induces an accumulation of charges at the semiconductor-dielectric interface which gives rise to a current (I_{SD}) if a potential difference between source and drain electrodes is applied (V_{SD}). The amount of current detected depends on the number of charges accumulated in the channel (i.e. on the V_{SG}) and on the intensity of the source-drain bias. The lateral electric field generated by V_{SD} is assumed to be smaller than the transverse field generated by V_{SG} (gradual channel approximation). Two main regimes describe the operation of an OFET:

- $V_{SD} \ll (V_{SG} - V_{TH})$, linear regime;
- $V_{SD} \gg (V_{SG} - V_{TH})$, saturation regime;

where V_{TH}, called threshold voltage, indicates the minimum value of V_{SG} in order for the transistor to turn on. V_{TH} is related to charge trapping at the semiconductor-dielectric interface: the first carriers induced by the V_{SG} are in fact trapped, so they do not contribute to the formation of the channel. Only after the increasing of the applied V_{SG} beyond a certain threshold value the carriers can effectively be accumulated and form the conduction channel. Thinking about the transistor as a capacitor, after the application of a $V_{SG} > V_{TH}$ an amount of charge dq is accumulated in an area of width dx in a position distant x from the source. This dq then depends on the channel width (W), on the capacitance per unit area of the dielectric (C_i), on the voltage applied (V_{SG}) and the threshold voltage (V_{TH}) as well as on the potential in the position x induced by the application of V_{SD} (which is zero at the source and V_{SD} at the drain):

$$dq = -WC_i[V_{SG} - V_{TH} - V(x)]dx \tag{1.12}$$

From the definition of current and charge carrier mobility:

$$I = \frac{dq}{dt} = \frac{dq}{dx}\frac{dx}{dt} \tag{1.13}$$

$$\mu = \frac{v}{E_x} = \frac{dx}{dt}(-\frac{dV_x}{dx}) \tag{1.14}$$

the following expression can be derived:

$$I_{SD}dx = WC_i\mu[V_{SG} - V_{TH} - V(x)]dV \tag{1.15}$$

By integrating the last expression over the entire channel length (at the source $x = 0$ and at the drain $x = L$) and assuming the mobility constant, the following equation is obtained:

$$I_{SD} = \frac{W}{L}C_i\mu[(V_{SG} - V_{TH} - \frac{1}{2}V_{SD})V_{SD}] \tag{1.16}$$

which can be simplified into

$$I_{SD} = \frac{W}{L}C_i\mu[(V_{SG} - V_{TH})V_{SD}] \tag{1.17}$$

in the approximation of $V_{SD} \ll (V_{SG} - V_{TH})$. This equation describes the linear regime of the transistor (Figure 1.14a). By increasing V_{SD} there will be a point in which $V_{SD} = (V_{SG} - V_{TH})$ (called pinch off point) and after that the current start to saturate. The potential close to the drain falls to zero and a depletion region is formed (Figure 1.14b). The current becomes thus independent to further increasing in V_{SD} which only implies an expansion of the depletion region and a shift of the pinch off point closer to the source (Figure 1.14c). This is the saturation regime and the equation describing the current behaviour is the following:

$$I_{SD} = \frac{W}{2L} C_i \mu (V_{SG} - V_{TH})^2 \tag{1.18}$$

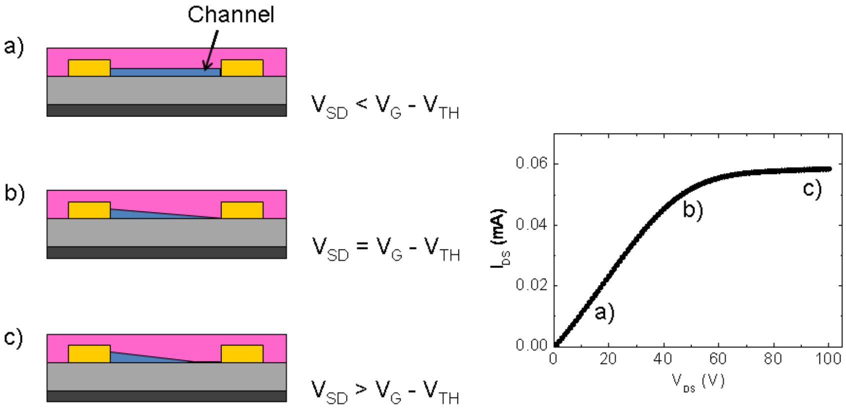

Figure 1.14: Opeating regimes in OFETs: the currrent first linearly increases with V_{SD} then gradually saturates approaching a constant value.

I_{SD} behaviour depends on two independent voltages and can be graphically visualized in two ways: the output characteristic (Figure 1.15a), where a set of drain currents as function of source-drain bias is plotted at various gate biases, and the transfer characteristic (Figure 1.15b), where the drain current is plotted as function of the gate bias.

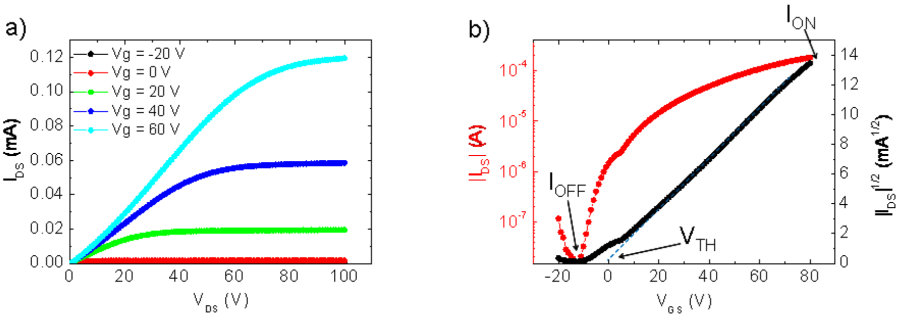

Figure 1.15: Example of a) output characteristic and b) transfer characteristic.

Parameter extraction mainly involves the extrapolation of the principal figure of merit (μ, V_{TH} and $\frac{I_{ON}}{I_{OFF}}$) from the OFET characteristics in linear or saturation regime. The charge carrier mobility, μ, is calculated from the linear and saturation regime expressions:

$$\mu_{LIN} = \frac{L}{W C_i V_{SD}} g_m \tag{1.19}$$

where

$$g_m = \frac{dI_{SD}}{dV_{SG}} \tag{1.20}$$

and

$$\mu_{SAT} = \left(\frac{d\sqrt{I_{SG}}}{dV_{SG}}\right)^2 \frac{2L}{WC_i} \tag{1.21}$$

Practically speaking, μ_{LIN} is calculated by fitting the linear part of the $I_{SD} - V_{SG}$ curve, while μ_{SAT} by fitting the linear part of the $\sqrt{I_{SD}} - V_{SG}$ curve. Even though it is the most reported value, the mobility in saturation regime is not constant because the density of charges varies considerably along the channel (Figure 1.14c) and thus the extracted value represents an average. It is often more prudent to extract the mobility in the linear regime where the density of charges is more uniform.

The threshold voltage, V_{TH}, indicates the voltage at which the charges starts accumulating and forming the channel and can be extracted from the intercept between the abscissa and the linear fit of the $I_{SD} - V_{SG}$ curve (in the linear regime) or the fit of the $\sqrt{I_{SD}} - V_{SG}$ curve in the saturation regime (Figure 1.15b blue dotted line). Ideally the V_{TH} value should be zero, but a non-zero value is very common in OFETs due to the large density of defects at the semiconductor/dielectric interface which act as traps for carriers.

The $\frac{I_{ON}}{I_{OFF}}$ indicates the difference between the device off state (where no current is flowing in the channel) and the on state (where the transistor is fully operating) and it is simply extracted from the ratio between the higher and lower current values in a semi-logarithmic plot $I_{SD} - V_{SG}$.

Contact resistance

A factor that could limit the prformance of an OFET is the presence of a high contact resistance (R_c), which is a measure of the ability of charge carriers to cross a metal-semiconductor interface. An OFET can be approximated to a device in which the conduction channel connecting the source and the drain electrodes is composed by a series of resistances [39, 40] (Figure 1.16). Two contributions give rise to the contact resistance at the electrodes: an internal resistance (R_i), originating from the energy mismatch between the work function of the metal and the HOMO (or LUMO) level of the organic material, and thus heavily dependent on the choice of the metal, and a bulk resistance (R_b), which represents the intrinsic resistance of the semiconductor to the injection/estraction of charges near the electrode. There is also another contribution one should take into account and it is the resistance arising from the entire transport channel (R_{ch}). The R_c value depends on the contact area between the metal electrode and the organic layer, thus on the device geometry. Small contact areas lead to remarkable R_c, thus to reduce this effect a geometry based on top-contacts with large contact areas is preferable.

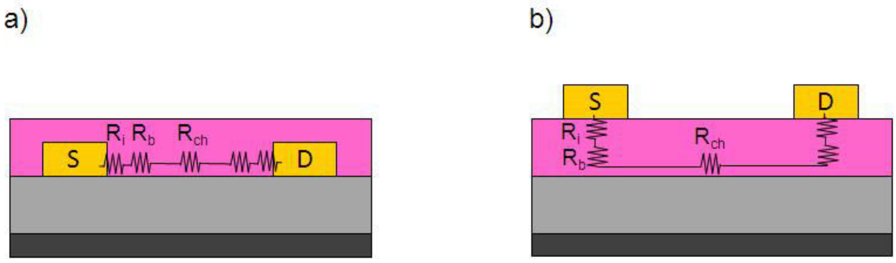

Figure 1.16: a) Bottom contacts and b) top contacts OFETs configurations showing the contributions of the contact resistances.

1.3.1 Ambipolar OFETs

Ambipolar transistors are devices able to transport both electron and holes depending on the bias applied to the electrodes. If the source electrode is held at ground, the definition of five distinct regimes depends on the relationship between V_{SG}, V_{SD}, V_{THh} (threshold voltage for the accumulation of holes) and V_{THe} (threshold voltage for the accumulation of electrons) [5, 41].

Unipolar linear regime for electrons

For $V_{SG} - V_{SD} > V_{THe}$, with the gate bias greater than the threshold voltage for electrons, and $V_{SG} - V_{SD} > V_{THh}$ the transistor operates in linear regime and only electrons are involved in the transport. The equation governing the current behaviour is thus eq 1.17 with the mobility and threshold voltage proper of electrons.

Unipolar saturation regime for electrons

Upon increasing of V_{SD} with the gate bias always greater than the threshold voltage for electrons, $V_{SG} - V_{SD}$ becomes smaller than V_{THe} but remains bigger than V_{THh}. In this situation the pinch-off of the channel constituted by electrons occurs and the saturation regime for n-type charges starts. The current thus obeys the eq 1.18 and it is dependent on $(V_{SG} - V_{TH})^2$.

Ambipolar regime

For $V_{SG} - V_{SD} < V_{THh}$ and always $V_{SG} > V_{THe}$ the gate electrode results more positive than the threshold voltage for electrons, so accumulation of negative charges occurs, but it also results more negative than the threshold voltage for holes, so accumulation of positive charges also occurs in the channel. Both types of charge carriers then contribute to the current which is defined as:

$$I_{SD} = \frac{W}{2L} C_i \mu_e (V_{SG} - V_{THe})^2 + \frac{W}{2L} C_i \mu_h (V_{SG} - V_{SD} - V_{THh})^2 \tag{1.22}$$

Ideally, the electrons will occupy the portion of the channel near the source electrode and the holes the opposite portion, the one close to the drain. In one point in the channel the charges will recombine, the position of this point depends on V_{SG}, V_{SD} and mobility ratio.

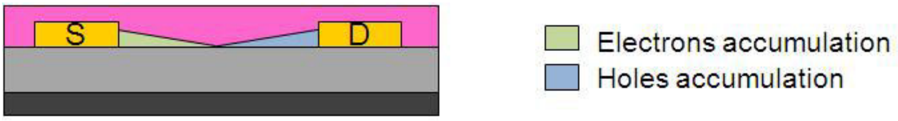

Figure 1.17: Sketch of the ambipolar regime.

Unipolar saturation regime for holes

The same considerations done in the case of electrons are valid also for holes, with appropriate changes in the potentials relationships. For $V_{SG} - V_{SD} < V_{THh}$ and V_{SG} bigger than V_{THh} but smaller than V_{THe}, a pinch-off of the channel occurs and the saturation regime for holes starts. The equation describing the current under these conditions is the same as the one for the case unipolar saturation regime for electrons with the substitution of μ_e, VSG and $VTHe$ with respectively μ_h, $(V_{SG} - V_{SD})$ and V_{THh}.

Unipolar linear regime for holes

For $V_{SG} - V_{SD} < V_{THh}$ and $V_{SG} < V_{THh}$ the current flowing in the channel is constituted by positive charges and depends linearly on $(V_{SG} - V_{SD})$; the transistor operates then in the linear regime for the holes.

The fabrication of ambipolar OFETs with high and balanced electron-hole mobilities is currently a research highlight due to their potential application in organic integrated circuits. The possibility of obtaining a simultaneous transport of both types of carriers would not only lead to a simplification in the design of complementary logic circuits, but would also reduce power dissipation and increase noise margins. Up to now there are three major groups of ambipolar OFETs: blends, single-component transistors and bilayers. In the first two cases the solution processability, which is the most desired requirement in organic electronic, is a standard, whereas in the third case, where the active part of the device is composed of two layers of different materials, the second layer is usually vacuum deposited on top of the first one because entire solution processed bilayers are still a great challenge [2, 42]. In chapter four it will be presented a study on polymeric ambipolar devices fabricated with a particular technique which allows the deposition of both n- and p-type layers from solutions.

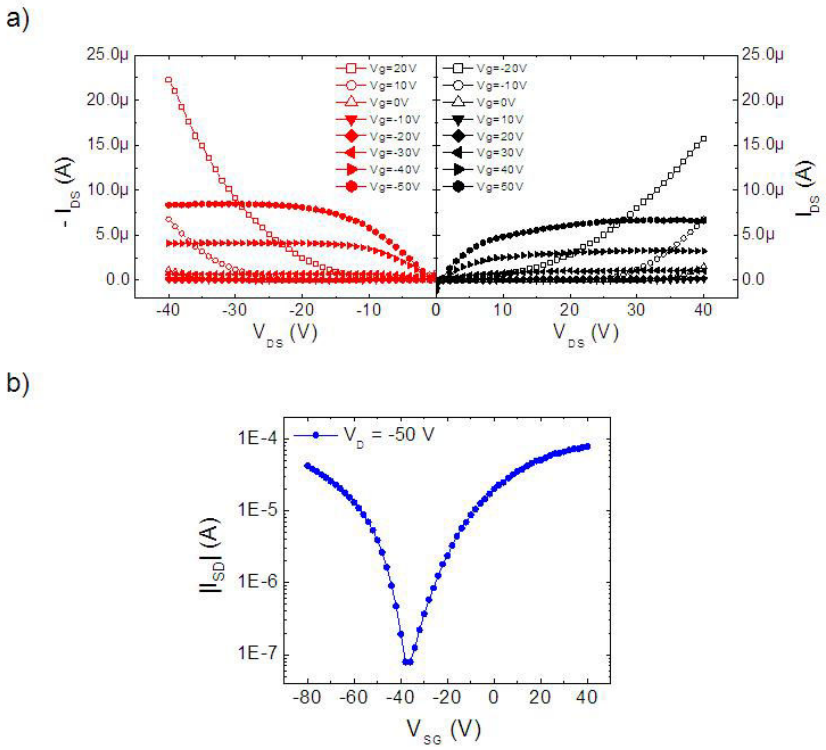

Figure 1.18: Examples of a) output and b) transfer curves of an ambipolar device.

1.4 Interfaces in organic devices

In an OFET there are at least two important interfaces playing a role in the correct operation of the device: the semiconductor-metal and the semiconductor-dielectric interface. The former is responsible for the injection and extraction of charge carriers from the electrodes, while the latter is related to the formation of the accumulation layer and the charge transport. In both cases, the use of self-assembled monolayers (SAM) represents a valuable solution for the optimization of the devices performance. SAMs are organic assemblies which spontaneously organize from solution or from gas phase onto the desired surface. A detailed review about the preparation, characterization and tailoring properties of SAMs can be foud in ref. [43].

1.4.1 Semiconductor-metal

For an efficient charge injection from a metal electrode into the active part of an OFET, the work function of the metal has to match the HOMO (or LUMO) energy level of the organic material [44–46]. In organic electronics, the description of the energy levels, and thus injection barriers, work function (ϕ), Fermi energy (E_F), ionization energy (I_E) and electron affinity (E_A), of a particular metal-organic system are commonly referred to the vacuum level (also named Mott-Schottky limit). This view implies that the energy level values of the two separated materials result unaltered when they are brought one on top of the other. In reality when an organic material is put in contact with a metal surface an interface dipole which causes a shift of the metal work function is created; this shift is called *interface dipole barrier*. The occurrence of the interface dipole is due to the mutual interaction between the molecules of the organic material and the electronic density at the metal surface; this interaction produces changes in the electrostatic potential. The metal in fact has two contributions: the bulk chemical potential and the surface dipole due to the presence of an electron distribution at the free surface. The presence of the organic material on the metal surface pushes back the surface metal electron density (*push-back effect*) and creates an interface dipole which reduces the vacuum level of the metal. The quantification of this vacuum level shift ($\Delta\phi$) depends on the metal-semiconductor pair and can be approximated by the Helmoltz equation:

$$\Delta\phi = \frac{eN\mu}{\epsilon\epsilon_0} \tag{1.23}$$

where $\Delta\phi$ is the shift in work function e is the electron charge, N is the dipole surface density, μ is the dipole moment perpendicular to the surface, ϵ is the dielectric constant and ϵ_0 is the vacuum permittivity. In the fabrication of bottom contacts OFETs, the creation of an interface dipole which alters the metal work function when an organic material is put in contact with it is exploited to tune the charge injection barrier. In effect, by using electron-poor SAMs the electrode work function is increased favoring holes injection, whereas by adopting electron-rich SAMs the electrode work function is decreased thus facilitating the electron injection.

SAMs characterized by alkyl chains with thiol end groups have a strong affinity to transition metals like gold (Au), ensuring the formation of a SAM layer strongly attached to the metal surface, so they are frequently used in the functionalization of the source and drain electrodes of an OFET. In chapter three of this thesis it is given an example of electrodes functionalization, done by using 1 mM undecanethiols $(CH_3(CH_2)_9CH_2SH)$ in ethanol (C_2H_6O). Pre-patterned samples were cleaned by acetone and isopropanol and then dried with nitrogen and exposed to ozone treatment for 5 minutes. Immediately after the ozone treatment the samples were immersed in the thiols solution and let rest for 12 hours before rinsing them with abundant C_2H_6O. This type of treatment lowered the Au work function of $\backsim$0.3 eV, thus improving the electrons charge injection.

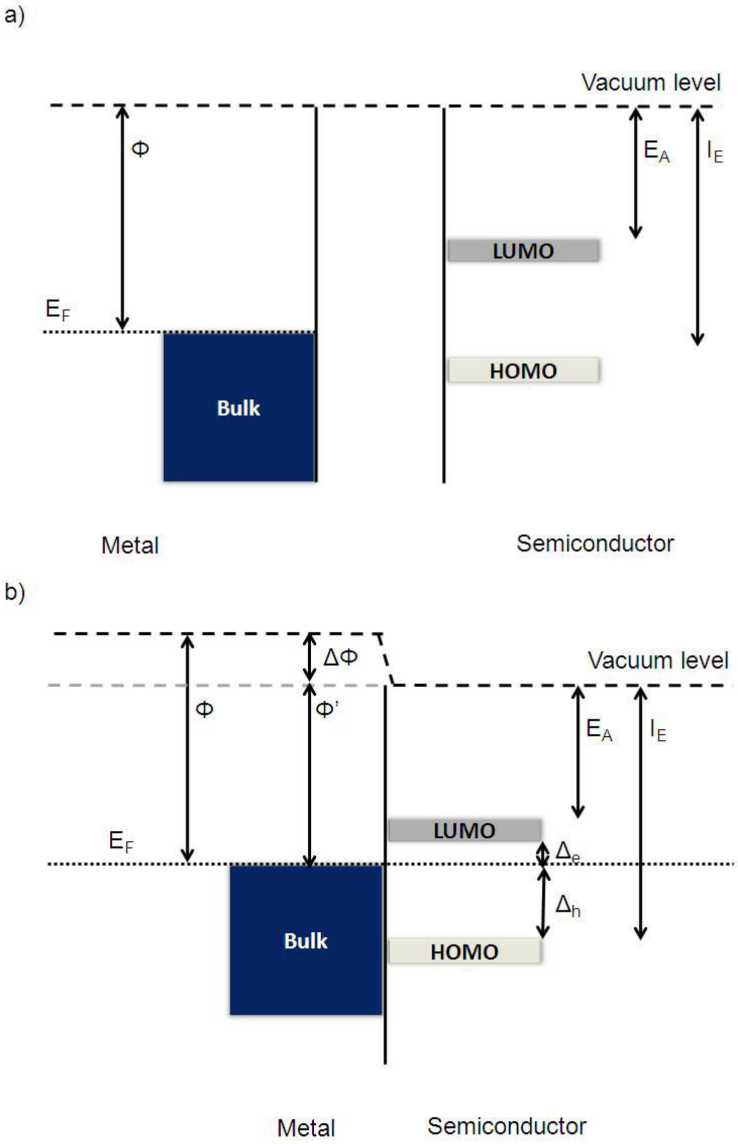

Figure 1.19: Sketch of the energy levels of a semiconductor-metal pair a) before and b) after the contact. The variations of the metal work function (ϕ) and in the injection barriers (Δe and Δh) are exaggerated to better visualize the process.

1.4.2 Semiconductor-dielectric

In OFETs the quality of the semiconductor-dielectric interface highly influences the charge transport since the accumulation of charges and the consequent formation of the channel occurs within the very first few nanometers of the organic material close to the dielectric. During this thesis the dielectric used in the OFETs fabrication was silicon oxide (SiO_2) thermally grown on a doped silicon gate. SiO_2 presents a large number of OH groups on the surface that act as electron traps. This charge trapping can be detrimental for the transport properties of n-type organic materials. In these cases, passivation of the SiO_2 surface by means of a SAM changes the dielectric surface energy and prevents the electron trapping coming from the hydroxyl groups [47, 48]. The variation of the dielectric surface energy contributes to a different arrangement of the organic material deposited on top, which could also affect the charge transport. In this thesis two molecules for the dielectric functionalization were used in different studies (Figure 1.20): hexamethyldisilazane, or HMDS ($[(CH_3)_3Si]_2NH$) and octatrichlorosilane, or OTS ($CH_3(CH_2)_{16}CH_2SiCl_3$). In the former case, 70 μL of HMDS were spin-coated on silicon substrates with 230 nm of SiO_2 as dielectric, whereas in the latter case, the substrates were immersed in a solution with OTS and toluene for 12 hours.

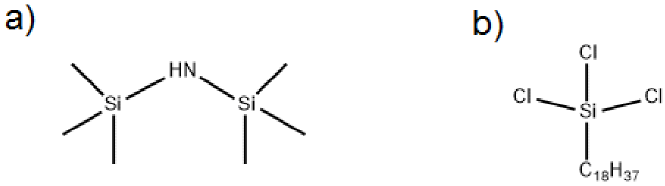

Figure 1.20: a) HMDS and b) OTS chemical structures.

1.5 Correlation between structural and electrical properties

A comprehensive description of charge transport in OFETs is still lacking primarily because of the immeasurable quantity of organic materials available and secondly due to the wide variety of parameters that can play a crucial role. As pointed out in this chapter, the choice of device geometry, as well as the semiconductor-insulator and the semiconductor-metal interfaces are among those. Also, the semiconducting layer deposition technique, its growth mechanism, its morphology and grain size as well as its crystallinity have important consequences on the charge transport mechanism governing the device. By Sirringhaus and co-workers [48] it has been recently pointed out that the description of charge transport in high-mobility molecular semiconductors at room temperature lays somewhere in between the ordered inorganic band-like conduction and the molecular hopping behaviour characteristic of disordered organic materials. With polymers, which present a higher degree of disorder than small molecules, the picture is even more complicated. Charge transport in these materials is strongly influenced by the polymer molecular weight [49] and it is governed by the simultaneous presence of polarons and structural and electronic disorder. Even though there are studies on the subject [50], the individual manifestation of these two contribution in OFETs performance is still unknown. Rivnay and co-workers [51–53] came up with the extrapolation of a parameter which quantifies the parachrystalline disorder (i.e. statistical fluctuation of individual lattice spacings) in polymeric OFETs. This parameter is called parachrystallinity factor

(g) and can been extracted from high resolution X-ray diffraction data:

$$g = \sqrt{\frac{\Delta q}{2\pi q_0}} \tag{1.24}$$

where Δq is the full width at half maximum of the Bragg reflection under investigation whose position is indicated by q_0. For OFETs the structural characterization of the organic semiconductor is fundamental to give a deep insight on the occurring charge transport mechanism, which is usually highly anisotropic [54–57]. Knowing the packing arrangement and the orientation of the molecules (or polymers) with respect to the main direction of charge transport is in fact essential for the deep physical understanding of the OFET performance [29, 30, 58].

1.6 Bibliography

[1] M. Mas-Torrent and C. Rovira. *Chemical Society Reviews* **37(4)**, 827–838 (2008)

[2] Y. Zhao, Y. L. Guo and Y. Q. Liu. *Advanced Materials* **25(38)**, 5372–5391 (2013)

[3] A. C. Arias, J. D. MacKenzie, I. McCulloch, J. Rivnay and A. Salleo. *Chemical Reviews* **110(1)**, 3–24 (2010)

[4] J. E. Anthony, A. Facchetti, M. Heeney, S. R. Marder and X. W. Zhan. *Advanced Materials* **22(34)**, 3876–3892 (2010)

[5] J. Zaumseil and H. Sirringhaus. *Chemical Reviews* **107(4)**, 1296–1323 (2007)

[6] J. S. Brooks. *Chemical Society Reviews* **39(7)**, 2667–2694 (2010)

[7] J. E. Anthony, J. S. Brooks, D. L. Eaton and S. R. Parkin. *Journal of the American Chemical Society* **123(38)**, 9482–9483 (2001)

[8] M. M. Payne, S. R. Parkin, J. E. Anthony, C. C. Kuo and T. N. Jackson. *Journal of the American Chemical Society* **127(14)**, 4986–4987 (2005)

[9] A. Mishra, C. Q. Ma and P. Bauerle. *Chemical Reviews* **109(3)**, 1141–1276 (2009)

[10] D. Fichou. *Journal of Materials Chemistry* **10(3)**, 571–588 (2000)

[11] M. A. Loi, E. Da Como, F. Dinelli, M. Murgia, R. Zamboni, F. Biscarini and M. Muccini. *Nature Materials* **4(1)**, 81–85 (2005)

[12] M. Mas-Torrent and C. Rovira. *Journal of Materials Chemistry* **16(5)**, 433–436 (2006)

[13] E. Laukhina, R. Pfattner, L. R. Ferreras, S. Galli, M. Mas-Torrent, N. Masciocchi, V. Laukhin, C. Rovira and J. Veciana. *Advanced Materials* **22(9)**, 977–+ (2010)

[14] Y. J. He and Y. F. Li. *Physical Chemistry Chemical Physics* **13(6)**, 1970–1983 (2011)

[15] A. Varotto, N. D. Treat, J. Jo, C. G. Shuttle, N. A. Batara, F. G. Brunetti, J. H. Seo, M. L. Chabinyc, C. J. Hawker, A. J. Heeger and F. Wudl. *Angewandte Chemie-International Edition* **50(22)**, 5166–5169 (2011)

[16] X. G. Li, C. Y. Xiao, W. Jiang and Z. H. Wang. *Journal of Materials Chemistry C* **1(45)**, 7513–7518 (2013)

[17] X. W. Zhan, A. Facchetti, S. Barlow, T. J. Marks, M. A. Ratner, M. R. Wasielewski and S. R. Marder. *Advanced Materials* **23(2)**, 268–284 (2011)

[18] I. Kymissis. Organic Field Effect Transistors: Theory, Fabrication and Characterization (Springer, 2009)

[19] J. E. Northrup. *Physical Review B* **76(24)** (2007)

[20] T. Liu and A. Troisi. *Advanced Functional Materials* **24(7)**, 925–933 (2014)

[21] H. Sirringhaus, P. J. Brown, R. H. Friend, M. M. Nielsen, K. Bechgaard, B. M. W. Langeveld-Voss, A. J. H. Spiering, R. A. J. Janssen, E. W. Meijer, P. Herwig and D. M. de Leeuw. *Nature* **401(6754)**, 685–688 (1999)

[22] K. Manoli, L. M. Dumitru, M. Y. Mulla, M. Magliulo, C. Di Franco, M. V. Santacroce, G. Scamarcio and L. Torsi. *Sensors* **14(9)**, 16869–16880 (2014)

[23] J. Rivnay, M. F. Toney, Y. Zheng, I. V. Kauvar, Z. H. Chen, V. Wagner, A. Facchetti and A. Salleo. *Advanced Materials* **22(39)**, 4359–+ (2010)

[24] R. Eisberg and R. Resnik. Quantum Physics of Atoms, Molecules, Solids, Nuclei and Particles (John Wiley and Sons, 1985), second edition edition

[25] R. E. Hummel. Electronic Properties of Materials, Fourth Edition (2011)

[26] N. W. Ashcroft and N. D. Mermin. Solid State Physics (Saunders College/Harcourt Brace College Publisher, 1976)

[27] V. Coropceanu, J. Cornil, D. A. da Silva, Y. Olivier, R. Silbey and J. L. Bredas. *Chemical Reviews* **107(4)**, 926–952 (2007)

[28] G. Horowitz. *Advanced Materials* **10(5)**, 365–377 (1998)

[29] R. A. Street, J. E. Northrup and A. Salleo. *Physical Review B* **71(16)** (2005)

[30] H. Sirringhaus. *Advanced Materials* **17(20)**, 2411–2425 (2005)

[31] D. Monroe. *Physical Review Letters* **54(2)**, 146–149 (1985)

[32] V. Y. Krivnov and A. A. Ovchinnikov. *Zhurnal Eksperimentalnoi I Teoreticheskoi Fiziki* **90(2)**, 709–723 (1986)

[33] S. Tretiak, S. Kilina, A. Piryatinski, A. Saxena, R. L. Martin and A. R. Bishop. *Nano Letters* **7(1)**, 86–92 (2007)

[34] W. P. Su, J. R. Schrieffer and A. J. Heeger. *Physical Review Letters* **42(25)**, 1698–1701 (1979)

[35] E. A. Davis and N. F. Mott. *Philosophical Magazine* **22(179)**, 0903–0922 (1970)

[36] M. C. J. M. Vissenberg and M. Matters. *Physical Review B* **57(20)**, 12964–12967 (1998)

[37] G. Horowitz and M. E. Hajlaoui. *Advanced Materials* **12(14)**, 1046–1050 (2000)

[38] Z. Bao and J. Locklin. Organic Field Effect Transistors (CRC Press, 2007), 1st ed. edition

[39] D. Braga and G. Horowitz. *Advanced Materials* **21(14-15)**, 1473–1486 (2009)

[40] L. Burgi, T. J. Richards, R. H. Friend and H. Sirringhaus. *Journal of Applied Physics* **94(9)**, 6129–6137 (2003)

[41] M. S. Kang and C. D. Frisbie. *Chemphyschem* **14(8)**, 1547–1552 (2013)

[42] P. Cosseddu and A. Bonfiglio. *Applied Physics Letters* **97(20)** (2010)

[43] J. C. Love, L. A. Estroff, J. K. Kriebel, R. G. Nuzzo and G. M. Whitesides. *Chemical Reviews* **105(4)**, 1103–1169 (2005)

[44] T. Laiho and J. A. Leiro. *Applied Surface Science* **252**, 6304 (2005)

[45] J. P. Hong, A. Y. Park, S. Lee, J. Kang, N. Shin and D. Y. Yoon. *Applied Physics Letters* **92(14)** (2008)

[46] B. H. Hamadani, D. A. Corley, J. W. Ciszek, J. M. Tour and D. Natelson. *Nano Letters* **6(6)**, 1303–1306 (2006)

[47] T. Umeda, D. Kumaki and S. Tokito. *Journal of Applied Physics* **105(2)** (2009)

[48] H. Sirringhaus, T. Sakanoue and J. F. Chang. *Physica Status Solidi B-Basic Solid State Physics* **249(9)**, 1655–1676 (2012)

[49] F. P. V. Koch, J. Rivnay, S. Foster, C. Muller, J. M. Downing, E. Buchaca-Domingo, P. Westacott, L. Y. Yu, M. J. Yuan, M. Baklar, Z. P. Fei, C. Luscombe, M. A. McLachlan, M. Heeney, G. Rumbles, C. Silva, A. Salleo, J. Nelson, P. Smith and N. Stingelin. *Progress in Polymer Science* **38(12)**, 1978–1989 (2013)

[50] J. F. Chang, H. Sirringhaus, M. Giles, M. Heeney and I. McCulloch. *Physical Review B* **76(20)** (2007)

[51] J. Rivnay, S. C. B. Mannsfeld, C. E. Miller, A. Salleo and M. F. Toney. *Chemical Reviews* **112(10)**, 5488–5519 (2012)

[52] J. Rivnay, R. Noriega, R. J. Kline, A. Salleo and M. F. Toney. *Physical Review B* **84(4)** (2011)

[53] J. Rivnay, R. Noriega, J. E. Northrup, R. J. Kline, M. F. Toney and A. Salleo. *Physical Review B* **83(12)** (2011)

[54] L. H. Jimison, A. Salleo, M. L. Chabinyc, D. P. Bernstein and M. F. Toney. *Physical Review B* **78(12)** (2008)

[55] A. Salleo, R. J. Kline, D. M. DeLongchamp and M. L. Chabinyc. *Advanced Materials* **22(34)**, 3812–3838 (2010)

[56] D. M. DeLongchamp, R. J. Kline, D. A. Fischer, L. J. Richter and M. F. Toney. *Advanced Materials* **23(3)**, 319–337 (2011)

[57] A. Salleo. *Materials Today* **10(3)**, 38–45 (2007)

[58] R. Noriega, J. Rivnay, K. Vandewal, F. P. V. Koch, N. Stingelin, P. Smith, M. F. Toney and A. Salleo. *Nature Materials* **12(11)**, 1037–1043 (2013)

CHAPTER 2

FABRICATION TECHNIQUES AND CHARACTERIZATION METHODS

In this chapter the main deposition methods of the studied organic materials together with the principal characterization techniques used during this thesis are described. Particular relevance is dedicated to the physical description of the X-rays based techniques, which supply the structural properties of the materials under exam.

2.1 Fabrication techniques

2.1.1 Spin-coating

The spin-coating is a well established fast and low-cost deposition technique for solution based organic semiconducting materials. The material is first solubilized in a low boiling point solvent (typically chloroform, $CHCl_3$) and the solution of the desired concentration is then spread on a substrate fixed on a disk which is rotated at a fixed speed of several thousands of revolution per minute (rpm) for the desired time. During the rotation of the substrate the majority of the solution is swept off, the solvent evaporates and the residual material tends to deposit uniformly on the surface. Important parameters to be optimized in a deposition by spin coating are the solution concentration, the rotating speed of the substrate and the time of the process, which are related by the following relationship [1]:

$$d = \sqrt{\frac{\eta}{4\pi\rho\omega^2 t}} \tag{2.1}$$

where d is the thickness of the film, η and ρ are respectively the viscosity coefficient and density of the solution, ω is the angular velocity and t the spinning time. If the solvent is volatile enough and the material is well-solubilized in it, this technique allows the production of very homogeneous thin-films, slightly thicker close to the edge of the substrate.

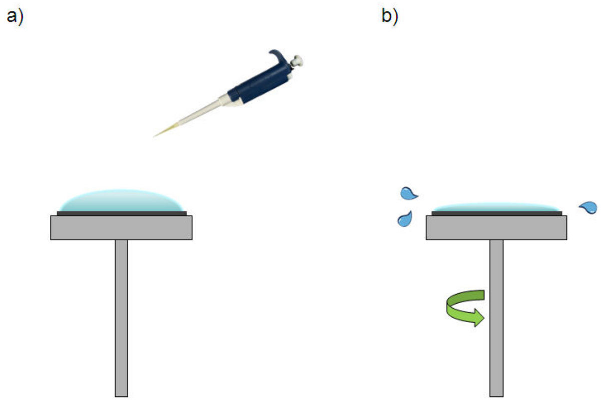

Figure 2.1: Sketch of the spin-coating deposition technique: a) a certain volume of the solution containing the organic material is dropped on the sbstrate surface positioned on a rotating sample holder; b) when the sample is rotated at the desired speed, the material deposits uniformly on the substrate surface while the solution excess is swept off.

2.1.2 Langmuir-Schaefer

The Langmuir-Schaefer (LS) deposition technique is a variant of the Langmuir-Blodgett (LB) method [2],[3],[4],[5], which involves the creation of a monomolecular film at the air-water interface, called Langmuir film. The LS approach is generally used when dealing with polymers due to the high rigidity of the polymeric chains. The apparatus for LS depositions (Figure 2.2) consists of a teflon trough equipped with mobile barriers, a Wilhelmy plate connected to an electrobalance and a mechanical arm to perform the film transfer.

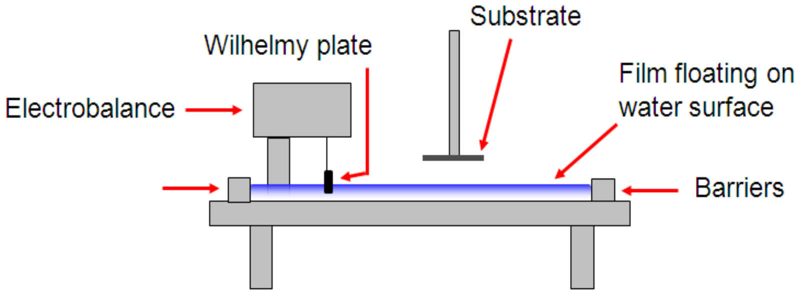

Figure 2.2: Sketch of the Langmuir-Schaefer apparatus.

The trough is filled with ultra-clean deionized water having a resistivity of 18.5 MΩcm to avoid ions-contamination coming from minerals present in common water; on the water surface a small quantity of the organic material dissolved in a volatile solvent is gently dropped. After the evaporation of the solvent the material is compressed by slowly closing the barriers and undergoes different phase transitions as indicated in Figure 2.3.

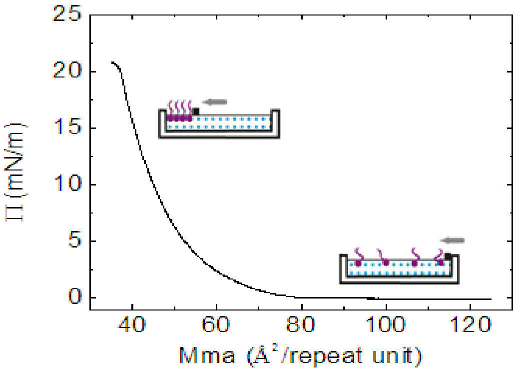

Figure 2.3: Example of isotherm, i.e. plot of the surface pressure *vs* the mean molecular area, before a deposition by LS technique. In the inital phase the molecules are widely dispersed on the water surface and the surface pressure measured by the Wilhelmy plate is negligible; then, by compressing the film thanks to the mobile barriers, the molecules are forced to get close to each other and organize on the water surface in a compact way and this increases the surface tension.

At the beginning, the film is in a 2D-gas state, where the molecules are barely interacting due to the large distance between them; the surface pressure in this phase can be estimated by the equation of state for ideal gases:

$$PV = nRT \tag{2.2}$$

which in the case of a very thin film uniformly covering all the surface area of the trough becomes:

$$PA = nRT \tag{2.3}$$

where P is the pressure, A is the area of the trough, n is the moles number, R is the ideal gas constant and T is the temperature (in Kelvin). When the compression of the barriers increases, the distance between the molecules decreases leading to the liquid phase in which molecules are loosely packed; when the molecules receive enough compression, they reach the solid phase in which they are closely packed in a film. If the barriers compression continues, the molecules start to organize in bi- or even tri-dimensional structures causing an abrupt decreasing of the surface pressure (collapse point). The solid phase is the phase in which the deposition can take place: the surface pressure is in fact high enough to ensure sufficient cohesion in the monolayer, avoiding it to fall apart during the transfer on the solid substrate; in LS technique the deposition is performed by gently putting in contact a solid substrate with a hydrophilic surface (like for example glass, quartz or silicon) with the film floating on the water-air interface, a process named *kissing* of the water. During the deposition the pressure is held constant by feedback from a pressure monitor. This technique exploits the surface tension γ (or free energy excess per unit area) at the air-water interface which originates from the fact that the water molecules at the surface experience a total net force different from zero, which is instead the case of the water molecules in the bulk. More precisely, one is interested in the surface pressure Π, which is defined as the difference between the surface tension of the clean subphase (γ_0) and the one of the same subphase covered with molecules (γ):

$$\Pi = \gamma_0 - \gamma. \tag{2.4}$$

The surface pressure is measured by means of the Wilhelmy plate (Figure 2.4); this plate is partially immersed in the subphase and experiences the following force:

$$F_0 = m_p g + \gamma_0 \cos\theta p - m_l g \tag{2.5}$$

where m_p is the mass of the plate, θ is the contact angle of the liquid on the solid plate surface, p is the perimeter of the plate and m_l is the liquid mass moved by the partially immersed plate. Then the surface pressure is deduced by measuring the change in the force acting on the plate with (F) and without (F_0) a molecular film present on the water surface:

$$\Pi = \gamma_0 - \gamma = \frac{F_0 - F}{p}. \tag{2.6}$$

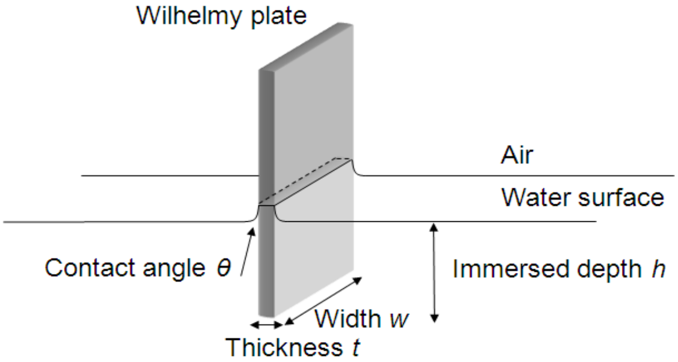

Figure 2.4: Sketch of the Wilhelmy plate partialy immersed in the deionized water which fills the trough.

2.1.3 Organic molecular beam deposition

Thermal sublimation of organic materials under high vacuum (HV) or ultra high vacuum (UHV) is called organic molecular beam deposition (OMBD) and it is a well exploited technique to fabricate highly ordered thin-films [6],[7],[8]. The film growth is governed by two key parameters, the substrate temperature T_{SUB} and the deposition rate Φ. The substrate surface must be flat (low roughness), homogeneous and inert (low surface energy) to guarantee a good adhesion and growth of the thin-film. The standard setup used for OMBD is mainly composed by a pre-chamber, a growth-chamber, a Knudsen cell, a quartz microbalance, a shutter and a sample-holder. The substrate is fixed on the sample-holder and inserted in the pre-chamber to go from atmospheric pressure to 10^{-3} mbar, then with a mechanical arm it is transferred inside the growth-chamber and let it rest until the pressure reaches at least 10^{-8} mbar (UHV). When the pressure is low enough, the temperature of the Knudsen cell containing the organic material is increased until the material sublimation starts; when the quartz microbalance in the growth-chamber measures a rate Φ stable at the desired value, the shutter protecting the substrate is removed and the material starts depositing. The degree of impurities present in the film depends on the quality of the vacuum and the deposition rate: the higher the vacuum and the lower the rate, the better the film grows.

2.1.4 Electrodes deposition

In this thesis both bottom-gate bottom-contacts and bottom-gate top-contacts geometries were exploited to fabricate OFETs. In the first case substrates with thermic SiO_2 and already pre-patterned electrodes were purchased and directly used after a standard cleaning procedure, while in the second case the fabrication of the metal electrodes was performed by physical vapor deposition in vacuum on top of the organic semiconducting material. The procedure for the electrodes deposition is as follows: first pellets of the chosen metal are placed in a crucible and heated up to their evaporation temperature, then, the condensation of the material on the substrate forms a film with the desired pattern thanks to shadow masks. The low pressure ($< 10^-6$ mbar) in the deposition chamber allows a straight line path between the crucible and the substrate, while the vacuum environment avoids the contamination of the source material (for example oxidation).

2.2 Characterization methods

Although the material deposition, the device architectures and the scientific goal of the studies presented in this thesis were different, the same multi-technique approach, based on the interconnection of structural, morphological and electrical characterizations was adopted. In some particular cases the structural evolution of critical parameters had to be followed directly in the same place where a specific process was happening and exactly during the same time-scale of the process itself, situation addressed like in-situ and real-time. In other more common cases, the structural investigation was performed ex-situ, that is on samples not undergoing any process.

2.2.1 Structural characterization

X-rays are electromagnetic waves with wavelength between 0.01 and 10 nm corresponding to an energy range of 0.1-100 keV and for this reason are good candidates for probing condensed matter at atomic level. The main X-rays techniques exploited in the study of organic thin-films for devices applications are:

- *X-ray Reflectivity* (XRR), for the evaluation of roughness, density and thickness of single- or multi-layer films;
- *out-of-plane measurements*: specular scan, i.e. $\theta - 2\theta$ scan, for the determination of the lattice periodicity in direction perpendicular to the film surface and rocking curve scan (RC), i.e. θ scan, for the quantification of the crystalline domains misorientation with respect to the surface normal;
- *in-plane measurement*: grazing incidence X-ray diffraction (GIXRD), for the determination of molecular orientation, crystal domain size and periodicity in the direction parallel to the film surface.

2.2.1.1 X-ray Reflectivity

XRR is a technique for studying surfaces and probing the structure of single- and multilayered thin film materials of hard and soft condensed matter. It allows the electron density profile along the surface normal, the layer thickness and the surface/interface roughness to be quantitatively evaluated [9],[10]. It can be applied to the study of thin layers surfaces and interfaces without any constrictions on the crystalline level, which means that measurements on amorphous, semiconductors, metals or polymers can be carried out. However few limitations, intrinsic of the method, have to be considered:

- the surface/interface of the sample needs to be extremely flat and smooth to avoid destructive interference of the outgoing X-rays;
- the film thickness has to be smaller than a few hundreds of nm to guarantee a correct interpretation of the coming out signal;
- the sample properties (thickness, density and roughness) have to be laterally homogeneous because the XRR mediates all the signals coming from the entire sample.

For X-rays the refractive index of air ($n = 1$) is higher than the refractive index of condensed matter (n_x), expressed by the relation:

$$n_x = 1 - \delta - i\beta \tag{2.7}$$

where δ and β represent respectively the deviation from unity and the linear absorption coefficient of the material and are very small quantities (10^5 - 10^6). Since the real part of this refractive index is slightly below unity, total external reflection occurs when an X-ray beam is impinging on a flat surface with an incident angle below a critical value (θ_c). The Snell law of refraction (depicted in Figure 2.5) indicates what happens to an electromagnetic radiation which passes through materials with different densities (i.e. refractive indices):

$$n_1 \sin\theta_i = n_2 \sin\theta_t \tag{2.8}$$

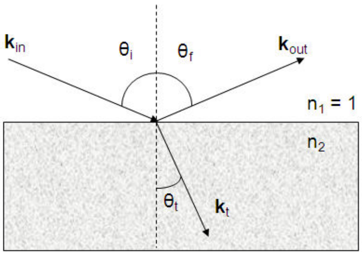

Figure 2.5: Sketch of the Snell law.

In X-ray geometry the angles are measured with respect of the sample surface, so the Snell law becomes:

$$\frac{1}{n_2} = \frac{\cos(\theta_t)}{\cos(\theta_i)} \tag{2.9}$$

and in the limit of θ_i and θ_t going toward zero, we can expand the cosine function with Taylor series:

$$\cos(x) \approx \left(1 - \frac{x^2}{2}\right) \qquad \text{for} x \to 0. \tag{2.10}$$

Neglecting the absorption ($\beta \approx 0$), the angle of the plane wave transmitted into the medium can be approximated with:

$$\theta_t = \sqrt{\theta_i^2 - 2\delta} \tag{2.11}$$

therefore total external reflection (i.e. $\theta_t = 0$) will be observed when the incidence angle fulfills the condition $\theta_i^2 \leq 2\delta$; the critical angle is thus defined as:

$$\theta_c = \sqrt{2\delta}. \tag{2.12}$$

On the other hand, when absorption is taken into account ($\beta > 0$), the angle of the transmitted wave becomes:

$$\theta_t = \sqrt{\theta_i^2 - 2\delta - 2i\beta}. \tag{2.13}$$

XRR data at fixed wavelength are obtained by simultaneously changing the coupled incidence (θ_i) and scattering (θ_f) angles, where θ_i and θ_f angles are measured from the surface plane. At the beginning of the measurement, when θ_i is very small, the incident wave is totally reflected (Figure 2.6a), but when the incident angle exceeds the critical angle of total external reflection ($\theta_i > \theta_c$, Figure 2.6b) part of the incident beam penetrates into the medium and the reflected intensity drops according to the Fresnel law.

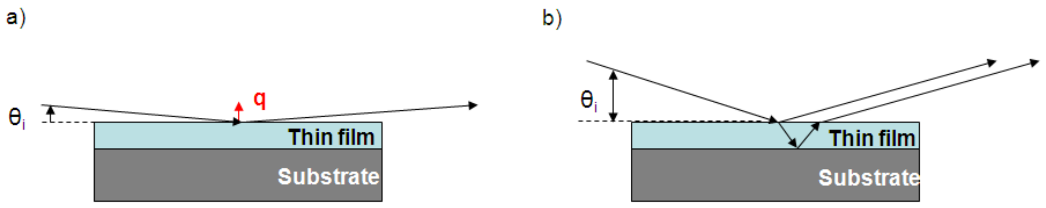

Figure 2.6: a) Sketch of the total external reflection taking place when $\theta_i < \theta_c$ and b) transmission and subsequent reflection from different layers when $\theta_i > \theta_c$ in X-ray reflectivity measurements.

This law describes the transmission and reflection of an electromagnetic wave when crossing a medium of different refractive indexes by calculating the expressions for the reflection (r) and transmission (t) coefficients:

$$r_{//} = \frac{E^r_{//}}{E^i_{//}} = \left[\frac{n_i\cos(\theta_t) - n_t\cos(\theta_i)}{n_i\cos(\theta_t) + n_t\cos(\theta_i)}\right] \tag{2.14}$$

$$t_{//} = \frac{E^t_{//}}{E^i_{//}} = \left[\frac{2n_i\cos(\theta_i)}{n_i\cos(\theta_t) + n_t\cos(\theta_i)}\right] \tag{2.15}$$

$$r_{\perp} = \frac{E^r_{\perp}}{E^i_{\perp}} = \left[\frac{n_i\cos(\theta_i) - n_t\cos(\theta_t)}{n_i\cos(\theta_i) + n_t\cos(\theta_t)}\right] \tag{2.16}$$

$$t_{\perp} = \frac{E^t_{\perp}}{E^i_{\perp}} = \left[\frac{2n_i\cos(\theta_i)}{n_i\cos(\theta_i) + n_t\cos(\theta_t)}\right] \tag{2.17}$$

where $E^i_{//}$ ($E^i_{\perp}$) is the amplitude of the incoming electric field with a parallel (perpendicular) polarization with respect to the medium surface, while E^r and E^t are the amplitudes of the electric field which respectively represent the reflected and transmitted electromagnetic wave. If the sample consists on a layer onto a substrate of different electron density, X-rays reflected from different interfaces do interfere and intensity oscillations occur, named Kiessig fringes. Figure 2.7 shows a typical simulated XRR profile for single layer system.

From a qualitative point of view, the layer thickness, t, can be easily estimated from the Kiessig fringes period by means of the following equation:

$$t = \frac{2\pi}{\Delta q} \tag{2.18}$$

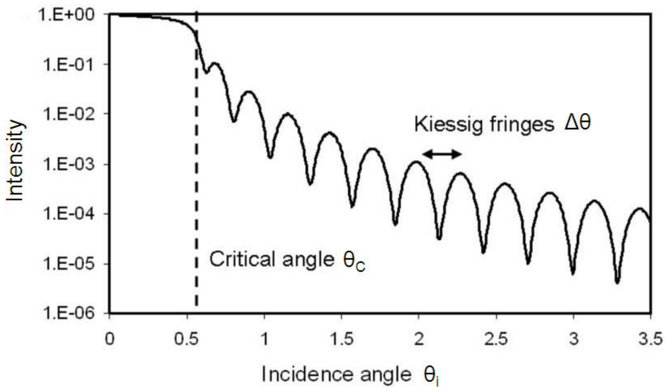

Figure 2.7: Example of Kiessig fringes in XRR measuremetns

where $\Delta q = \frac{4\pi}{\lambda}\left[\sin(\theta_2) - \sin(\theta_1)\right]$ is the difference of scattering vector (defined in eq. 2.29) with λ the wavelength of the electromagnetic radiation and θ_1 and θ_2 the angular positions of two adjacent maxima.

The mass density of the material can also be evaluated if the chemical composition is known and constant. The electron density ρ of a layer is in fact strictly related to the θ_c for that particular layer by the following relation:

$$\theta_c^2 = 2\rho\lambda. \tag{2.19}$$

The θ_c is experimentally read off as the value where the reflectivity is dropped to 50% of its value at the plateau of external reflection.

From a more quantitative point of view, the reflected X-ray beam has to be considered as the beam resulting from constructive interference of multiple reflections (i.e. multiple interfaces, Figure 2.8).

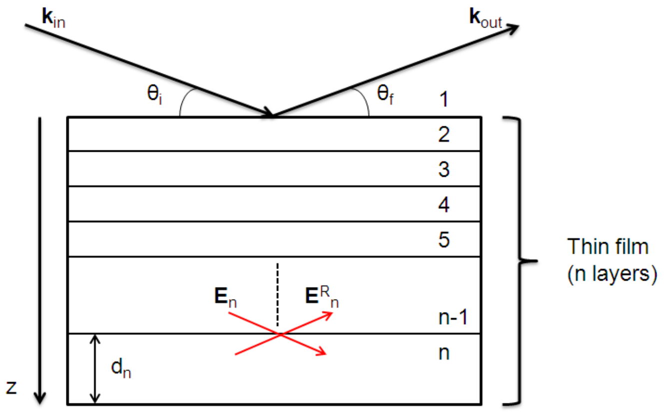

Figure 2.8: Sketch of the multi-layer film model.

The electron density profile, the thickness and the surface/interface roughness of each layer can be calculated by exploiting a fitting procedure based on Parratt's recursive formula [11]:

$$R_{n-1,n} = a_{n-1}^4 \frac{R_{n,n+1} + F_{n-1,n}}{R_{n,n+1}F_{n-1,n} + 1} \tag{2.20}$$

where $R_{n-1,n}$ and $R_{n,n+1}$ are the reflection coefficients respectively at the interface between the $(n-1)$-th and the n-th layer and the n-th and the $n+1$-th layer, while $F_{n-1,n}$ is the Fresnel coefficient of the interface between the $(n-1)$-th and the n-th layer. An algorithm which minimizes a χ^2 merit function based on the square of the difference between experimental and calculated curves is also present.

2.2.1.2 X-ray diffraction

X-ray diffraction [12],[13] is a powerful non destructive technique generally exploited for the structural characterization of a wide variety of materials. The cardinal point of this technique is the coherent elastic scattering of radiation from ordered lattice planes, which is summarized in the Bragg's law:

$$2d\sin(\theta) = n\lambda \tag{2.21}$$

where θ and λ are respectively the incident angle and the wavelength of the incoming electromagnetic wave, while d is the interplanar spacing of lattice planes of the same family.

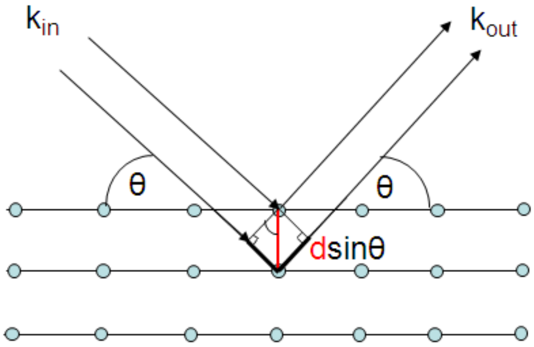

Figure 2.9: Sketch of the geometrical derivation of Bragg's law

A convenient way to describe diffraction is by referring to the reciprocal space. Each sample is represented by its crystal lattice which is the periodic repetition of the same unit in 3D. In real (or direct) space the crystal lattice is generated by three fundamental axes $(\vec{a}, \vec{b}, \vec{c})$ and has a corresponding lattice in reciprocal space which is described by other axes $(\vec{a'}, \vec{b'}, \vec{c'})$ defined as below:

$$\vec{a'} = \frac{(\vec{b} \times \vec{c})}{(\vec{a} \cdot \vec{b} \times \vec{c})} \tag{2.22}$$

$$\vec{b'} = \frac{(\vec{c} \times \vec{a})}{(\vec{a} \cdot \vec{b} \times \vec{c})} \tag{2.23}$$

$$\vec{c'} = \frac{(\vec{a} \times \vec{b})}{(\vec{a} \cdot \vec{b} \times \vec{c})}. \tag{2.24}$$

In the reciprocal space a lattice plane is represented by a node which is identified by the vector $\vec{G}$ defined as:

$$\vec{G}_{hkl} = h\vec{a'} + k\vec{b'} + l\vec{c'} \tag{2.25}$$

where h, k, l (Miller indexes) are integers and represent a plane in the crystal with intercepts $\frac{1}{h}$, $\frac{1}{k}$, $\frac{1}{l}$ respectively with the axes $\vec{a}$, $\vec{b}$ and $\vec{c}$. (hkl) defines a family of planes whose intercepts are $\frac{n_1}{h}$, $\frac{n_2}{k}$, $\frac{n_3}{l}$, that is integer multiples of the original one, and the distance between any two adjacent planes in the same family is d_{hkl}. An equivalent way to describe diffraction in reciprocal space is referring to the Laue conditions:

$$\vec{q} \cdot \vec{a} = 2\pi h \tag{2.26}$$

$$\vec{q} \cdot \vec{b} = 2\pi k \tag{2.27}$$

$$\vec{q} \cdot \vec{c} = 2\pi l \tag{2.28}$$

where $\vec{q}$ is the scattering vector and represents the difference between the incoming and outgoing wave vectors:

$$\vec{q} = \vec{k}_{out} - \vec{k}_{in} \tag{2.29}$$

The three Laue conditions need to be verified if we want diffraction to take place and this can be achieved by the scattering vector:

$$\vec{q} = h\vec{a'} + k\vec{b'} + l\vec{c'} \tag{2.30}$$

which indicates that constructive interference will occur provided that the difference in wave vectors is a vector of the reciprocal space. Bragg condition is thus satisfied when $\vec{q}$ intersects a reciprocal lattice point whose position is defined by the general lattice vector $\vec{G_{hkl}}$:

$$q_B = |\vec{q}_B| = \frac{4\pi}{\lambda}\sin(\theta_B) = 2\pi|\vec{G}_{hkl}| \tag{2.31}$$

The possible diffraction conditions can be visualized by means of the Ewald sphere geometrical construction (Figure 2.10).

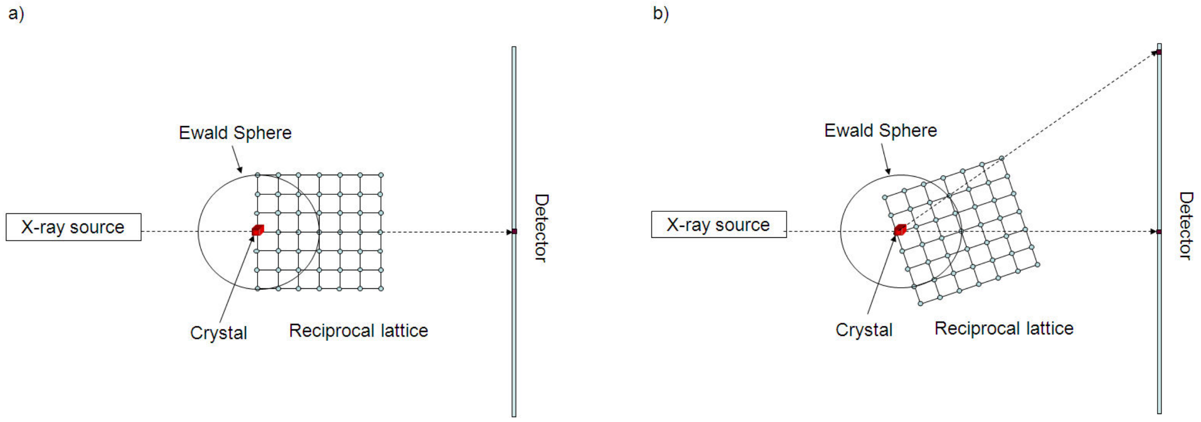

Figure 2.10: Representation of a) the Ewald sphere construction and b) the diffraction from the Ewald sphere.

This is an ideal sphere centered on a point of the reciprocal space considered as the crystal center and characterized by a radius of $\frac{1}{\lambda}$ and a shell not infinitely thin, but related to the instrumental accuracy of the experimental setup. In this geometry the reciprocal lattice has its origin at the point lying simultaneously on the Ewald sphere and on the incoming beam. To simulate a diffraction experiment, we can consider the reciprocal lattice rotating (in the experiment either the sample or the X-ray source is moving in order to change the incident angle of the incoming radiation); when a node of the reciprocal lattice crosses the Ewald sphere, the Bragg's law is respected and we observe non-zero diffracted intensity on the detector.

According to the kinematical approximation, the intensity of the spots on the detector (I_{hkl}) is proportional to the amplitude of the diffracted wave as it is described by the following equations [14]:

$$I_{hkl} = |A_{diff}|^2 \tag{2.32}$$

$$I_{hkl} = |A_0 \left(\frac{e^2}{mc^2 R_0} \right) F(\vec{q}) S_{Na}(\vec{q} \cdot \vec{a}) S_{Nb}(\vec{q} \cdot \vec{b}) S_{Nc}(\vec{q} \cdot \vec{c})|^2 \tag{2.33}$$

where A_0 represents the amplitude of the incoming electromagnetic wave, R_0 is the distance sample-detector, $F(\vec{q})$ is the structure factor, i.e. the Fourier transform of the electron density of one unit cell of the crystal, and S_{Nj} ($j = a, b, c$) are called N-slit interference functions and are defined as:

$$S_{Nj} = \sum_{n=0}^{N-1} e^{i\vec{q} \cdot n\vec{j}}. \tag{2.34}$$

These functions are sharply peaked at $q = \frac{2\pi m}{j}$ and describe a periodic array of δ functions with a spacing of $\frac{2\pi}{j}$. They are responsible for the fact that the diffracted intensity from a crystal comes along specific directions.

Usually, diffraction from single crystals is exploited to solve the structure of the material under exam; the unit cell parameters can be determined from the positions and intensities of the Bragg spots. The intensity is in fact related to the structure factor, which contains information about the position of each of the N atoms in the unit cell and it is defined as:

$$F(\vec{q}) = \sum_{j=1}^{N} f_j e^{2\pi i \vec{q}\cdot\vec{r_j}} \tag{2.35}$$

where f_j is the atomic form factor of the j-th atom and r_j is the vector indicating the position of the j-th atom inside the unit cell.

Unfortunately, the synthesis of single crystals from organic materials is not always possible, so one is forced to use the X-ray diffraction from powder to solve the structures. The main structural results exhibited in this thesis are represented by X-ray diffraction from thin-films. In these cases, the diffraction conditions are obtained by conveniently orienting the sample surface with respect to the incident X-ray beam. Rarely the crystalline structure of the organic material under investigation can be determined, but from the diffraction of different lattice planes the crystalline order as well as the molecular organization in the surface plane and along the surface normal can be determined.

2.2.1.3 Specular scan

In the specular scan, or $\theta/2\theta$ scan, the angle of the incoming and outgoing radiation are coupled: as the incoming beam impinges with an angle θ with respect to the sample surface, the detector collects the scattered intensity at an angle of 2θ. In this geometry the incident beam is specularly diffracted from the surface (here the name *specular scan*) and the scattering vector $\vec{q}$ is directed along the surface normal $\vec{n}$ (Figure 2.11). In this particular geometry one is sensitive to the distance between lattice planes parallel to the surface. The full width at half maximum of the diffracted peaks ($\Delta(2\theta)$) is correlated with the coherent length $L_\perp$ along the film growing direction according to the Scherrer law:

$$L_\perp = \frac{K\lambda}{\Delta(2\theta)\cos(\theta_B)}, \tag{2.36}$$

where K is a constant generally equal to 0.9 and θ_B is the angle position of the Bragg reflection.

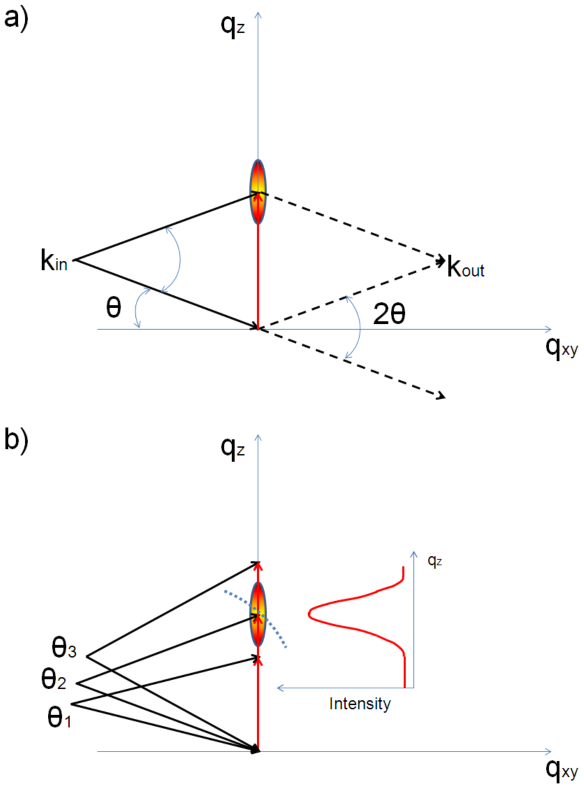

Figure 2.11: Sketch of the $\theta/2\theta$ scan: a) representation of the incoming and outgoing wave vectors and the Bragg spot to probe; b) evolution of the scattering vector in the reciprocal space during the $\theta/2\theta$ scan and representation of the related intensity profile.

2.2.1.4 Rocking curve

Rocking curves (RCs) are recorded by varying the x-rays incident angle, while the detector position is kept constant at the Bragg position $2\theta_B$ (Figure 2.12). In this case the incident angle is called ω to differentiate the type of measurement from the $\theta/2\theta$. In this way information about the mosaicity of the film are obtained. The mosaicity is the quantification of the diffracting domains misorientation with respect o the surface normal.

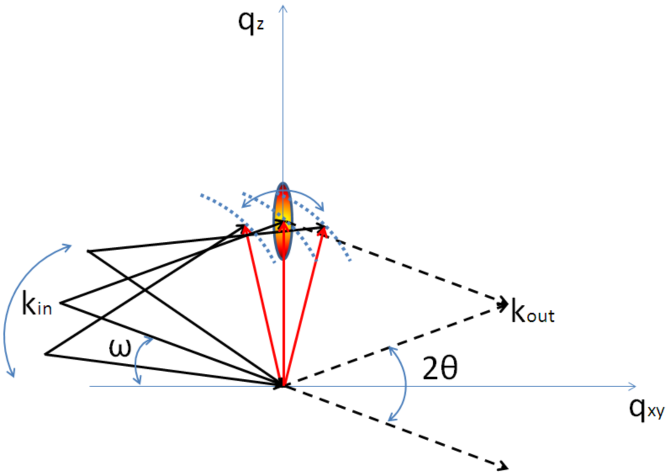

Figure 2.12: Sketch of the RC scan: the incident angle ω is varied while the angle of the detector is kept at constant position $2\theta_B$.

2.2.1.5 Grazing Incidence X-ray Diffraction

Grazing Incidence X-Ray Diffraction (GIXRD) [15], [16], [17] is a technique based on diffraction and on the extreme surface sensitivity of incident X-rays close to the critical angle for total external reflection (θ_c). In GIXRD setup the angle of the incoming radiation θ_i is kept at very small constant value while the angle of the detected radiation $theta_f$ scans the 2ϕ range.

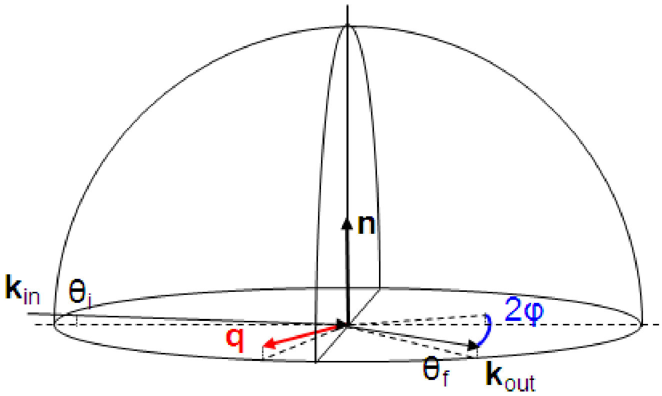

Figure 2.13: Sketch of GIXRD measurement.

In this configuration the incident and diffracted wave vectors are confined in a plane almost parallel to the surface, in such a way that the scattering vector $\vec{q}$ is always nearly perpendicular to the surface normal $\vec{n}$. Since in diffraction the structure of the sample is always probed in the $\vec{q}$ direction, GIXRD probes the interplanar spacing of lattice planes vertically inclined with respect to the sample surface.

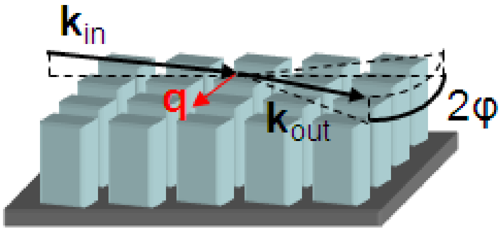

Figure 2.14: Sketch of GIXRD measurement: the scattering vector probes the distance between lattice planes almost parallel to the surface normal.

In GIXRD geometry, the incident angle is usually optimized to increase the scattering from the film surface and reduce the contribution of the substrate. The quantity which is normally taken into account to evaluate the portion of the surface probed by the radiation is the penetration depth (Λ), approximated as:

$$\Lambda \approx \frac{\lambda}{2\pi\sqrt{\theta_c^2 - \theta_i^2}} \tag{2.37}$$

2.2.1.6 Laboratory source *vs* synchrotron

The X-rays sources exploited in this thesis are two: a Smartlab-Rigaku diffractometer (installed at IMM-CNR of Bologna) and the synchrotron radiation (ELETTRA facility in Trieste, Italy, and ESRF facility in Grenoble, France).

The diffractometer is based on a rotating copper anode ($\lambda = 1.54180\mathring{A}$), a sample stage able to move in the x-y plane and a point detector. The sketch of the main parts of the diffractometer is presented in Figure 2.15. The electrons produced by thermoionic effect from a tungsten filament (cathode) heated by an electric current hit the rotating copper anode which then emits X-rays. With respect to the fixed anode, the rotating one helps dispersing the heat of the incoming cathodic beam and thus enables to perform long scans at high intensity. Nevertheless, a water cooling system refrigerates the anode preventing overheating. The incident optics is characterized by a paraboloidal synthetic multilayer mirror coupled with a germanium (Ge) channel-cut crystal which monochromizes and collimates the divergent beam generated from the X-ray source into a parallel beam and a width-limiting slit which restricts the width of the sample area irradiated by the X-rays. The receiving optics is characterized by another Ge channel-cut crystal called analyzer, a receiving soller slit and a detector. A soller slit is a set of metal foils placed at constant intervals and it suppresses the divergence of the X-ray beam and thus determines the scattered beam angular resolution by extracting only the X-rays parallel to the gaps between the metal foils. For this particular diffractometer the soller slit is designed to be inserted vertically or horizontally. The detector is a scintillation counter and it is positioned on the receiving arm of the diffractometer which can move both in the out-of-plane (z) and in-plane (x-y) directions.

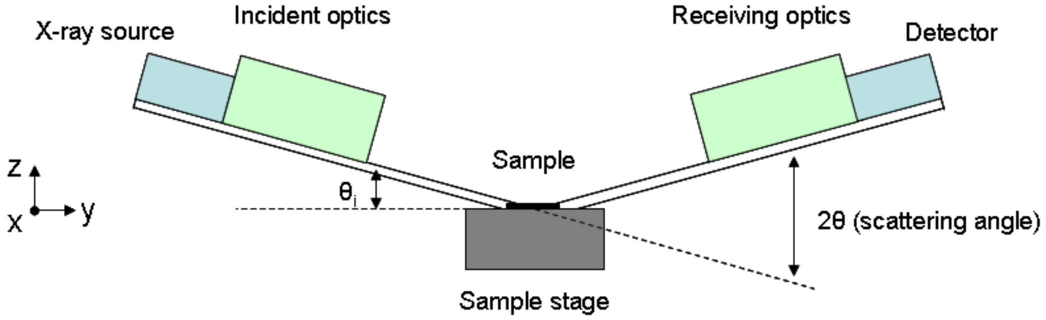

Figure 2.15: Sketch of the diffractometer setup.

The synchrotron radiation is generated by the acceleration of ultra-relativistic electrons through a magnetic field. Electrons emitted by an electron gun are first pre-accelerated in a linear accelerator and then transmitted to a circular one (booster synchrotron) where they are accelerated to reach energies typically in the GeV range. After reaching the desired relativistic energy, these electrons are injected into a large storage ring where they can circulate in a vacuum environment close to the speed of light. During their traveling inside the storage ring, the electrons path is guided by a series of alternating magnets: the bending magnets, which maintain the electrons on their circular orbit, and the insertion devices, which instead force the electron beam to follow a wavy trajectory. Each time the electrons pass through a magnet, they change direction which translates into the emission of X-rays. These x-ray beams are directed towards beamlines that surround the entire storage ring. Such electromagnetic radiation is characterized by:

- high flux, i.e. high number of photons which allows rapid experiments or use of weakly scattering materials;
- high brilliance [photons/($s\ mrad^2\ mm^2\ 0.1\%BW$)]: high number of photons per second, per angular divergence, per cross-sectional area of the beam, per 0.1% of the wavelength bandwidth; it basically indicates how many photons can be concentrated in a small area;
- high collimation, i.e. small angular divergence of the beam.

Organic materials are characterized by very low density and disorder, so their scattered intensity is usually very low. Moreover to achieve information in real-time the acquisition time scale has to be of the order of the time scale evolution of the physical parameter intended to follow. For these reasons the use of synchrotron radiation is required. However the high photon flux and the strong beam collimation can be responsible for a quick sample damaging, which has to be limited by choosing proper experimental conditions and it has to be evaluated during the data analysis. On top of that, the access to synchrotron facilities has not to be taken for granted and the simple reproduction of an experiment, just to prove the accuracy and the reproducibility of the obtained results, can happen after one year from the first experiment. On the other hand the open access to a conventional laboratory diffractometer allows performing experiments on a wide set of samples at the expenses of long acquisition time.

The recording of the diffracted radiation depends on the type of detector. Usually in a laboratory there is a punctual or linear detector mounted onto the receiving arm of the diffractometer, while in more advanced facilities based on synchrotron radiation, there is a 2D detector. In the first case the data collection proceeds by continuously increasing the out-of-plane scattering angle 2θ (or the in-plane scattering angle 2ϕ), i.e. continuously moving the detector, in order to obtain what is called a diffracted intensity profile as a function of the angular position of the detector. In the second case, a 2D detector is mounted along the direction of the incoming beam and does not need to be moved during the data collection. The only thing to do is to select the distance of the detector from the sample before performing the measurement which means select the portion of the reciprocal space to investigate and consequently the resolution of the image. This type of detector is especially needed for GIXRD measurements because one can probe a big portion of the reciprocal space in few seconds instead of collecting a single intensity profile in several hours.

The presence of a 2D detector in GIXRD geometry allows the observation not only of reflections coming from lattice planes almost parallel to the surface normal, but, especially for polycrystalline materials like organics, also other reflections coming from lattice planes tilted from the surface normal direction. These reflections are generated by a misorientation of the crystalline domains and they occur in a region of the reciprocal space which is nominally forbidden for the GIXRD geometry (along the $\vec{q}_z$ direction). In Figure 2.16 it is sketched the effect of domain misorientation on the 2D-GIXRD diffraction pattern. In the case of a polycrystalline film the diffraction pattern presents a ring, because it collects the diffracted intensity coming from all the crystalline domains randomly oriented, or an arc (spot) in the direction, if the majority (entirety) of the crystalline domains have a preferred orientation.

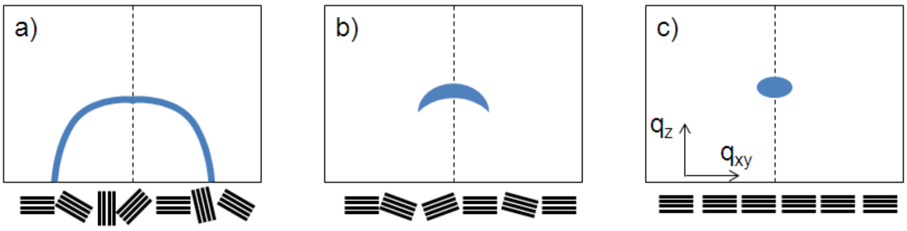

Figure 2.16: Schematic of diffraction patterns from a polycrystalline sample with a) randomly oriented crystalline domains, b) slghtly misoriented crystalline domains along the $\vec{q}_z$ direction, c) highly oriented crystalline domains along the $\vec{q}_z$ direction.

In order to correctly visualize the portion of the reciprocal space really probed, each GIXRD image coming from a 2D detector (Figure 2.17a) has first to be transformed from pixels to angles with the following relationship

$$\theta = \frac{1}{2} arctg \left(\frac{(x - x_0)0.172}{D} \right) \tag{2.38}$$

where $(x - x_0)$ represents the distance of a point in pixels from the position of the direct X-ray beam on the image, 0.172 is the expression of the pixel size in mm and D is the beam-sample distance in mm. After this first step, the axes of the image can be converted from diffraction angles to the corresponding scattering vectors(Figure 2.17b) by using the following calibration matrix [18]:

$$\vec{q} = \vec{k}_{out} - \vec{k}_{in} \begin{pmatrix} \cos(\theta_f)\cos(2\phi) - \cos(\theta_i) \\ \cos(\theta_f)\sin(2\phi) \\ \sin(\theta_f) + \sin(\theta_i) \end{pmatrix}$$

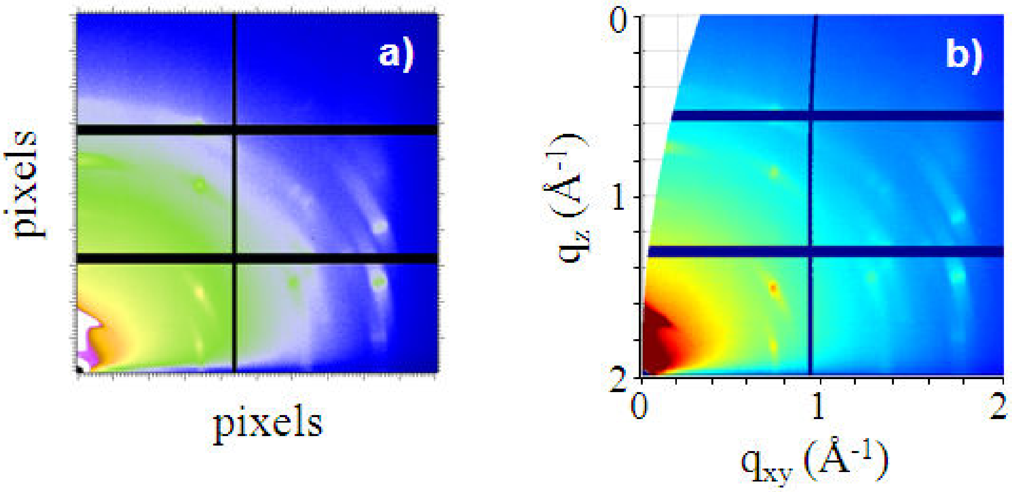

Figure 2.17: Example of conversion of a a) 2D-GIXRD image as visualized on the detector to b) the correct representation of the reciprocal space probed.

If we refer to crystalline surfaces, which represent an ideal situation if compared to polycristalline ones, it is possible to consider three different cases (Figure 2.18): i) a surface of one single 2D monolayer of atoms; ii) a single 2D monolayer on top of a bulk substrate; iii) a truncated crystal.

As previously mentioned, the diffracted intensity can be described within the kinematical approximation by using eq 2.33. If the $\vec{c}$ axes is taken along the surface normal, the case of the solely surface of just a 2D monolayer can be described by observing that the function $S_{Nc}(\vec{q} \cdot \vec{c})$ reduces to 1. This indicates that the diffraction is independent from

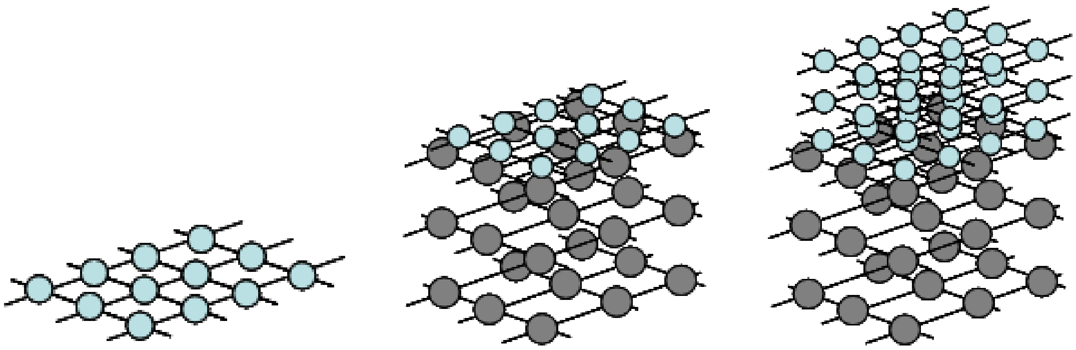

Figure 2.18: Schematic of a) a surface, b) an ideal surface onto a crystal, c) a truncated crystal

the component of the scattering vector perpendicular to the surface. As a result in the reciprocal space the diffraction intensity is non-zero just along *rods*: these rods are very peculiar characteristic of diffraction from a surface. In much more realistic cases the diffraction pattern is not made by simple rods because the surface is not perfectly 2D and it is on top of a crystal bulk, which gives its own contribution to the diffraction. In fact, what is normally observed is a combination of rods and spots (or elongated spots) and a transformation from rods into spots when the surface thickness is increased (Figure 2.19).

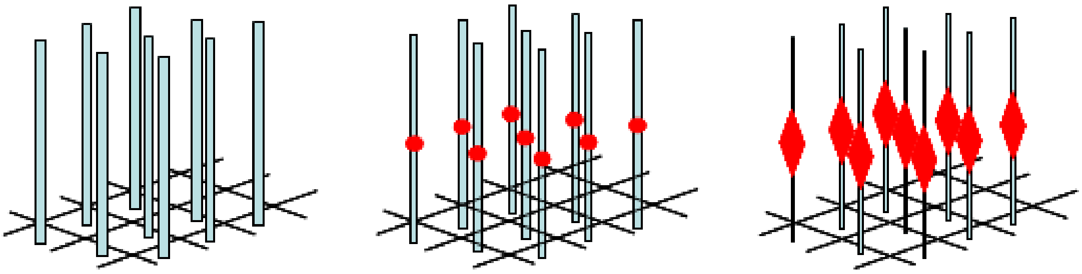

Figure 2.19: Schematic of diffraction pattern coming from a) a surface, b) an ideal surface onto a crystal, c) a truncated crystal

Organic thin films are usually polycrystalline films, and their electrical properties depend on the crystalline level and the orientation of crystalline domains. In this cases 2D-GIXRD measurements give an enormous amount of information.

2.2.2 Morphological characterization

Atomic Force Microscopy is a scanning probe technique used to obtain images of the film surface topography up to the nm scale. The AFM operating principle is based on a *cantilever* with a fixed elastic constant and a nanoscopic sharp *tip* which interacts with the sample surface at the atomic level. Dealing with relatively soft materials like organic semiconducting thin-films, all the AFM images presented in this thesis were recorded in tapping mode (TM-AFM). In TM-AFM the cantilever oscillates periodically at a frequency near the resonant one. The tip intermittently touches the sample' surface and moves through all the selected area thanks to a piezo which governs the motion in the 2D $x-y$ plane. A laser beam focused on the backside of the cantilever is reflected on a photodiode which detects the cantilever deflections due to the tip-surface interaction. The surface topography alters the cantilever's oscillation amplitude which is restored by a feedback loop connected to another piezo that adjusts the cantilever's position in the z-axis direction. Therefore, the tip scans line by line a surface area of several μm^2 and provides a 3D map of the surface topography by collecting point by point the cantilever's variation in the vertical z-axis direction.

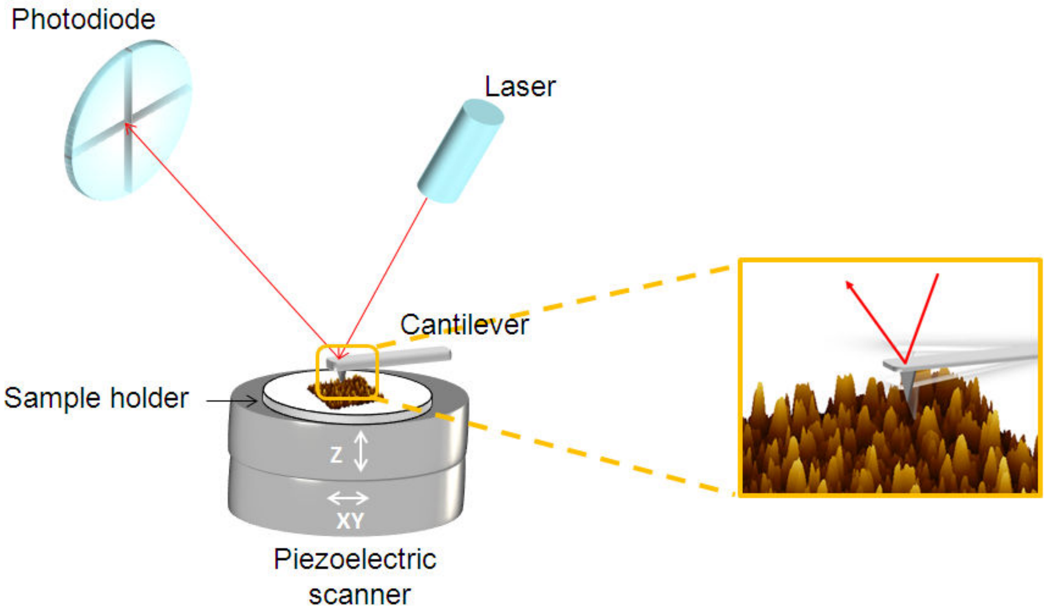

Figure 2.20: Sketch of the AFM apparatus with a zoom illustrating the oscillating cantilever.

2.2.3 Electrical characterization

The electrical characterization of the devices was performed using a Keithley 2636A dual channel sourcemeter as semiconductor parameter analyzer (Figure 2.21a) controlled by associated software. The devices to be characterized were placed on a Cascade Microtech M150 probe station (Figure 2.21b). All the device studied in this thesis were bottom-gate, thus the plate of the probe station on which the devices were placed was used for contacting the gate electrode. All the measurements were done in a glove box (Jacomex) in over-pressure of nitrogen and with oxygen and water levels lower than 5 ppm.

Figure 2.21: a) Keithley 2636A semiconductor parameter analizer, b)Cascade Microtech M150 probe station for electrical characterization.

2.2.4 Optical characterization

The optical characterization of molecules in solution as well as spin-coated on high-quality quartz substrates was performed by collecting UV-vis absorbance spectra using a V-670 Jasco double-beam spectrophotometer (Figure 2.22) equipped with a single monochromator (wavelength range: 190-2700 nm), a Xenon lamp as source light and a photomultiplier tube as detector.

Figure 2.22: V-670 Jasco spectrophotometer and relative software.

Basically, a UV/Vis spectrophotometer compares the light intensity incident on the sample (I_0) with the one transmitted by the sample itself (I). The absorbance (A) is in fact defined as follows:

$$A = log\frac{I_0}{I} \tag{2.39}$$

The extent of the absorption of UV-vis radiation is proportional to the number of molecules capable of undergoing the observed electronic transition. In this thesis, absorbance spectra were performed to extrapolate the energy gap (E_G) value of two compounds both in solution and film forms (Chapter 3). E_G was estimated from the position of the most intense absorbance peak, corresponding to the 0-0 electronic transition, by using the following relationship:

$$E = \frac{hc}{\lambda} \tag{2.40}$$

where h is the Planck constant, c is the speed of light and λ is the radiation wavelength.

2.3 Bibliography

[1] T. Ohara, Y. Matsumoto and H. Ohashi. *Physics of Fluids a-Fluid Dynamics* **1(12)**, 1949–1959 (1989)

[2] I. Langmuir. *Journal of American Chemical Society* **39**, 1848–1906 (1917)

[3] I. Langmuir and V. J. Schaefer. *Journal of American Chemical Society* **60**, 2803–2810 (1938)

[4] K. Blodgett. *Journal of American Chemical Society* **57**, 1007–1022 (1935)

[5] K. Ariga, Y. Yamauchi, T. Mori and J. P. Hill. *Advanced Materials* **25(45)**, 6477–6512 (2013)

[6] F. Schreiber. *Physica Status Solidi a-Applied Research* **201(6)**, 1037–1054 (2004)

[7] S. Kowarik, A. Gerlach and F. Schreiber. *Journal of Physics-Condensed Matter* **20(18)** (2008)

[8] J. A. Venables, G. D. T. Spiller and M. Hanbucken. *Reports on Progress in Physics* **47(4)**, 399–459 (1984)

[9] P. Colombi, D. K. Agnihotri, V. E. Asadchikov, E. Bontempi, D. K. Bowen, C. H. Chang, L. E. Depero, M. Farnworth, T. Fujimoto, A. Gibaud, M. Jergel, M. Krumrey, T. A. Lafford, A. Lamperti, T. Ma, R. J. Matyi, M. Meduna, S. Milita, K. Sakurai, L. Shabel'nikov, A. Ulyanenkov, A. Van der Lee and C. Wiemer. *Journal of Applied Crystallography* **41**, 143–152 (2008)

[10] A. v. d. Lee. *Solid State Sciences* **2**, 257–278 (2000)

[11] L. G. Parratt. *Physical Review* **95(2)**, 359–369 (1954)

[12] N. W. Ashcroft and N. D. Mermin. Solid State Physics (Saunders College/Harcourt Brace College Publisher, 1976)

[13] R. Eisberg and R. Resnik. Quantum Physics of Atoms, Molecules, Solids, Nuclei and Particles (John Wiley and Sons, 1985), second edition edition

[14] I. K. Robinson. *Physical Review B* **33(6)**, 3830–3836 (1986)

[15] H. Dosch, B. W. Batterman and D. C. Wack. *Physical Review Letters* **56(11)**, 1144–1147 (1986)

[16] H. Dosch. *Physical Review B* **35(5)**, 2137–2143 (1987)

[17] P. Dutta. *Current Science* **78(12)**, 1478–1483 (2000)

[18] S. Lilliu, T. Agostinelli, E. Pires, M. Hampton, J. Nelson and J. E. Macdonald. *Macromolecules* **44(8)**, 2725–2734 (2011)

CHAPTER 3

A COMPARATIVE STUDY ON OFETS BASED ON TWO PERYLENE DI-IMIDE DERIVATIVES

In this chapter a multitechnique structural study on two alkyldiimide perylene derivatives for OFET applications is reported.

3.1 Introduction

Among various n-type Organic semiconducting small molecules, perylene alkyl-diimide (PDIs) derivatives have demonstrated good air stability, processability and high charge carrier mobility [1–8]. The functionalization of the perylene core by cyano groups lowers the LUMO energy, thus preventing the formation of oxygen-related electron traps and enhancing the solubility of the materiel by slightly decreasing the core planarity [9, 10]. Solubility can be further improved by introducing appropriate side-chains [8, 11]. For this purpouse, branched alkyl side-chains are widely adopted in literature to modify the steric hindrance of polyaromatic molecules [8, 12]. Moreover, favourable π-π stacking interactions can be obtained if a 3.4-3.5 $\AA$ interlayer separation is reached; also in this case, the length, the shape and the polarity of the alkyl residues play a fundamental role. For example, variation of the alkyl chain branching point was recently found to be an effective strategy for tuning the molecular packing and enabling high charge transport mobilities [13]. In this chapter it is presented how the introduction of chemical modifications, such as a branching point in the alkyl chain design, affects the capability of supramolecular organization on a surface and consequently the charge transport of a small molecule.

3.2 Experimental

3.2.1 Active Materials

N′-bis(n-octyl)-dicyanoperylene-3,4:9,10-bis(dicarboxyimide) (PDI8CN2) and N,N′-bis-(2-ethylhexyl)-1,7-dicyanoperylene-3,4:9,10-bis(dicarboxyimide) (N1400) molecules were used as received from Polyera and BASF, respectively. The two derivatives are isomers and only differ in the shape of the alkyl side-chains (Figure 3.1): linear for PDI8CN2 and branched for N1400.

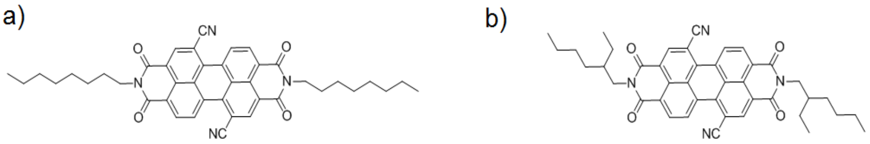

Figure 3.1: Chemical structure of a) PDI8CN2 and b) N1400.

PDI8CN2 is a well-known air-stable n-type organic small molecule featuring mobilities as high as 0.2 cm^2/Vs [7, 14–16], whereas N1400 is an emerging n-type material characterized by high processability [17]. The melting temperatures T_m for both compounds were determined by monitoring by optical microscopy at which temperature the powder starts melting. The T_m extracted values amount to (302 ± 3) °C and (310 ± 3) °C for PDI8CN2 and N1400, respectively. The test on the solubility in chloroform ($CHCl_3$) of the two compounds gave values around 2 mg/mL for PDI8CN2 and 5 mg/mL for N1400. As already mentioned, the big diversity in solubility arises from the different conformation of the side chains.

3.2.2 Device fabrication

All the substrates (pre-patterned bottom gate-bottom contact devices with 230 nm of silicon oxide as dielectric, Fraunhofer IPMS, Dresden, Germany) were cleaned in ambient conditions by acetone and isopropanol and then dried off using a gentle nitrogen flow. The device surface was functionalized by HMDS as descripted in chapter 1. Thin-films of PDI8CN2 and N1400 were prepared by spin-coating for 30 sec at 1000 rpm 190 μL of solution at various concentrations in $CHCl_3$ onto the substrates. For each concentration considered, three identical devices were prepared; the first one was used as-prepared, the second one was thermally annealed at 110 °C for 5 hours and the last one underwent electrodes functionalization by means of undecanethiols (see section 1.3.1). Preparation, annealing and source-drain functionalization were carried out in nitrogen environment.

3.2.3 Characterization methods

3.2.3.1 Structural characterization

2D-GIXRD images were collected at the beamline XRD1 of ELETTRA synchrotron facility (Trieste, Italy) by using a wavelength of 1 $\AA$ and a beam size of 200x200 μm^2. The incident angle of the X-ray beam, α_i, was chosen below and close to the critical angle to discriminate the contribution to the diffraction pattern coming from the upper layers of the organic film and that coming from the substrate. The 2D-GIXRD diffraction patterns were recorded using a 2D camera (Pilatus detector) placed normal to the incident beam direction. XRRs were performed using a SmartLab Rigaku diffractometer in a parallel beam geometry equipped with a CuK_α (λ = 1.5418 $\AA$) rotating anode followed by a parabolic mirror to collimate the incident beam and a series of variable slits (placed before and after the sample position) to obtain an acceptance of 0.02°. The crystal structure of N1400 was retrieved by laboratory powder diffraction data, ab-initio indexing and structure solution and refinement methods, using a conventional Bragg-Brentano parafocussing geometry.

3.2.3.2 Morphological characterization

Topographical AFM characterization was carried out in intermittent contact mode in air environment making use of a Smena, NT-MDT (Moscow, Russia) and a Veeco Dimension 3100 operating on a Nanoscope IV control unit.

3.2.3.3 Electrical characterization

The electrical behaviour of the devices was thested in nitrogen atmosphere by collecting output and transfer characteristics and comparing the mobility and threshold voltage values obtained in saturation regime.

3.3 Results and discussion

3.3.1 The structures of the bulk

The knowledge of the packing features of these molecules within the crystal represents the starting point to understand the charge transport mechanism occurring in the organic semiconductor. Figures 2a-b show the comparison between the crystal structure of bulk PDI8CN2, taken from ref. 15, and that of N1400.

The latter has been here determined by means of ab-initio X-ray powder diffraction methods using a rigid body description for the whole molecule, flexible at the C-C torsion angles of the alkyl residues. The analysis of powder XRD measurements revealed that N1400 self-assembles into triclinic crystals belonging to space group P-1; the cell parameters are a = 6.302(1), b = 8.8095(7); c = 16.557(3) $\AA$, α = 88.322(8), β = 84.60(1), γ = 110.63(1)°. The synthesis of this species leads to the formation of a mixture of four stereoisomers, two RR/SS and RS/SR enantiomeric pairs, with R or S having 50% of probability on either side. The overall crystal packing is only marginally affected by the relative disposition of the S (or R) ethyl residues within very flexible alkyl chains. Substituted perylene tetracarboxylic diimides tend to tightly pack with closely stacked cores at distances typically lying in the 3.40-3.50 $\AA$ range [18]: PDI8CN2 molecules are

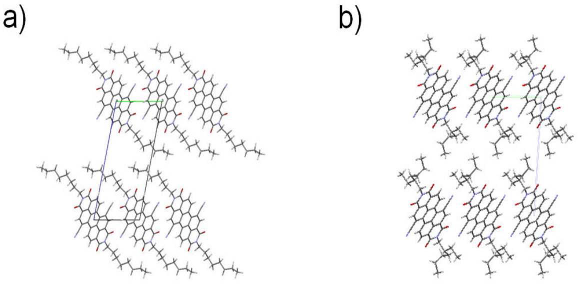

Figure 3.2: Schematic drawings of the crystal structure viewed down [100] of a) PDI8CN2 15 and b) N1400. In the latter case, for sake of simplicity, only one of the four possible diastereoisomers (R,S or meso), disordered within the crystals, is shown.

in fact separated by 3.40 $\AA$, while in N1400 the distance among parallel polyaromatic cores is slightly increased (up to 3.54 $\AA$). The high solubility of N1400 compound can be also attributed to the occurrence of multiple "distinct" stereoisomers, which determine anomalously high solubility levels, as if thermodynamically independent components were present. This effect is also found in conglomerates of enantiomorphic crystals [19] and atropisomeric molecules stabilized by hindered rotations [20].

3.3.2 The structures of the films

3.3.2.1 Grazing incidence X-ray diffraction

The thin-films of PDI8CN2 and N1400 prepared by spin-coating a 1.9 mg/mL solution from chloroform onto a hexamethyldisilazane (HMDS)-treated SiO_x surface were first characterized by 2D-GIXRD in order to investigate the effect of the substrate-adsorbate interaction during the film formation. Although the two structures show some similarities in the bulk, the presence of branched side chains in N1400 hinders the crystallization process. This is clearly visible by comparing the numerous Bragg spots observed in the 2D-GIXRD images collected for the PDI8CN2 film (Figure 3.3a) with the only one present for the N1400 film (Figure 3b).

By indexing Bragg spots, we can establish that PDI8CN2 films grow according to a 2D-powder-like structure adopting edge-on packing where $\pi - \pi$ stacking is lying parallel to the film plane. From the Bragg spots positions the same cell parameters of the bulk phase are extracted [15], in the limit of the technique resolution. This similarity is related to the pronounced thermodynamic stability of the PDI8CN2 crystal structure which prevents the formation of a (distinct) thin-film phase induced by the substrate interaction, as already shown for evaporated films [15], even during fast and non-equilibrium growth process as spin casting [21]. On the other hand, only one Bragg spot is observed in the 2D-GIXRD image collected for the N1400 film (Figure 3.3b). This spot corresponds to the

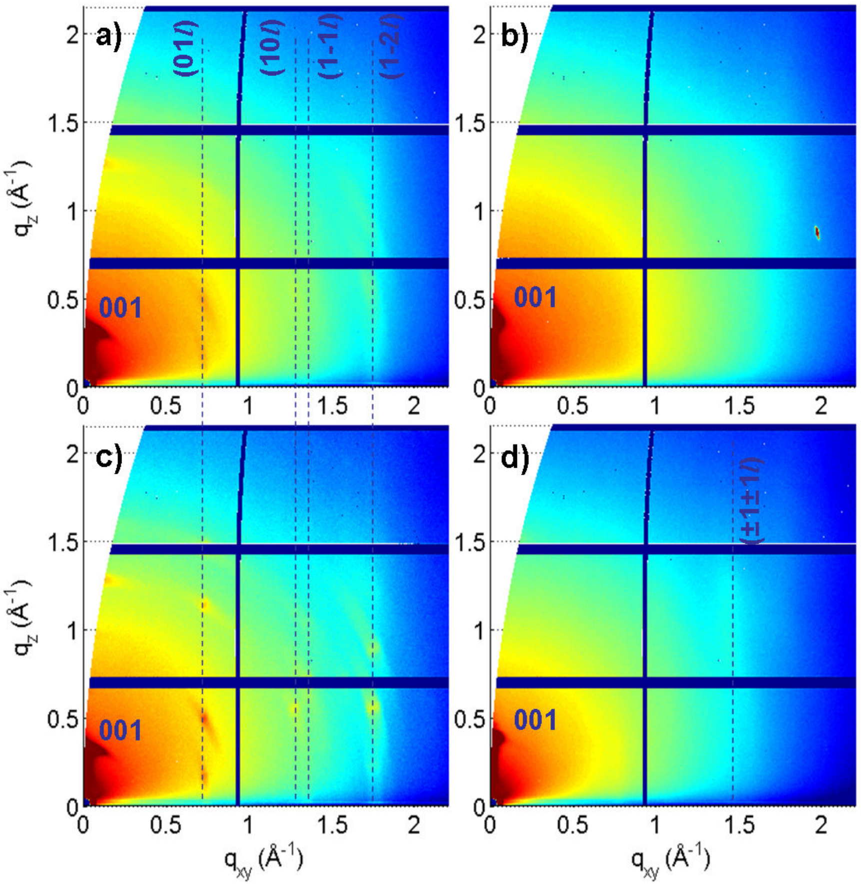

Figure 3.3: 2D-GIXRD images at incident angle 0.1° of thin-films spin-coated on HMDS-treated substrates. As-cast: a) PDI8CN2, and b) N1400. Thermal treated at 110 °C for 5 hours: c) PDI8CN2, and d) N1400. All the images have the same intensity log-scale.

(001) reflection, which, being in the out-of-plane direction (q_z), reveals that molecules are oriented with their longer axis almost normal to the surface, as found for the PDI8CN2 (i.e. ab plane parallel to the surface). The position of (001) gives a d_{001} spacing value, i.e. the monolayer thickness, equals to 18 $\AA$, more than 1 $\AA$ higher than the bulk value, i.e. d_{001}(bulk) = 16.46 $\AA$. The higher monolayer thickness could be ascribed to i) a tilting of the average polyaromatic molecular planes towards c, the normal to the film surface (the ab plane), or ii) a tilting and/or a stretching of the alkyl chains. Moreover, no trace of (even partial) crystallinity in the in-plane structure, dominated by the π-π stacking, is observed. Figures 3.3c and 3.3d report the 2D-GIXRD images recorded after annealing the samples at 110 °C for 5 hours. The intensity of Bragg peaks increases in both films, providing evidence for an increased crystallinity as induced by the thermal treatment. In the case of PDI8CN2, the lateral size of the crystallites, evaluated from the peak width along q_{xy} direction, using the Scherrer-formula [22] and taking into account the

beam footprint as described in ref [23], increases from 8 to 14 nm. In the case of N1400 a new, very weak Bragg rod appears after annealing (Figures 3.3d), again assigned to the growth of larger coherent domains in ab. Moreover, after annealing d_{001} decreases towards the bulk phase value (17 $\mathring{A}$). This structural transition is more pronounced for a thicker N1400 film, where several Bragg spots appear after the annealing (Figure 3.4).

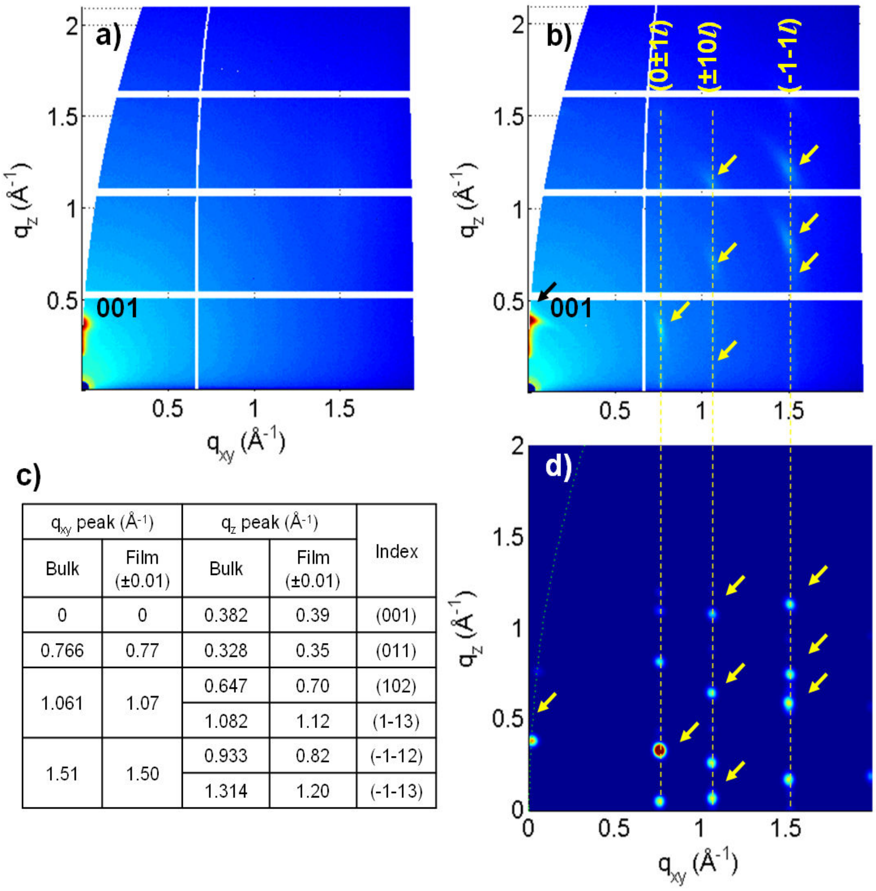

q_{xy} peak (Å^{-1})		q_z peak (Å^{-1})		Index
Bulk	Film (±0.01)	Bulk	Film (±0.01)	
0	0	0.382	0.39	(001)
0.766	0.77	0.328	0.35	(011)
1.061	1.07	0.647	0.70	(102)
		1.082	1.12	(1-13)
1.51	1.50	0.933	0.82	(-1-12)
		1.314	1.20	(-1-13)

Figure 3.4: 2D-GIXRD images collected on a thick film of N1400 prepared by spin coating a) before and b) after annealing. c) Tabulated data and indexing for peaks observed from b). d) 2D-GIXRD simulation using bulk phase structure and assuming [001] texturing with a small degree of misorientation.

Figures 3.4a and 3.4b show the 2D-GIXRD images collected for a 30 nm thick N1400 film before and after thermal annealing at 110 °C, respectively. Five new Bragg reflections appear after annealing, as the result of the crystallization process. Their positions were extracted (Figure 3.4c) and compared with those of the diffraction pattern simulated assuming a polycrystalline film with the bulk crystal structure (Figure 3.4d). No differences are observed between the values of the in-plane component of momentum transfer (q_{xy}), meaning that the in-plane cell parameters, a, b and γ correspond exactly to those of the bulk phase. Although the insufficient amount of reflections does not allowed the cell parameter to be determined, the good agreement between the simulated and the experimental images, in particular, of their spot intensities, made it possible to establish that the molecular packing in the film tends to the same as the powder bulk phase. These findings suggest that during the fast spin-coating process, N1400 molecules self-organize in a metastable phase with lower crystalline order. The explanation is strictly related with the alkyl chains morphology. Kinetic effects dominate the crystallization process during the spin coating deposition. Since the deposition parameters are the same for both molecules (isomers), the same amount of thermal energy is available for molecular motions. Given that the π-π staking in the crystal structure of both isomers is similar, because of the strong $\pi - \pi$ interaction between aromatic cores, the rotational energy barrier of the isomer with branched alkyl chains is expected to be greater than that with linear ones, resulting in slower molecular motions (this effect can be justified by the spherical hindrance of the branched alkyl chains). Therefore, we suppose that under kinetic regime, i.e. a non-equilibrium process, the isomer with branched alkyl chains does not have enough energy and time to self-assemble in the ″bulk″ structure and a new metastable phase is formed, which is further stabilized by the entropic contribution provided by the conformational disorder of the branched alkyl chains.

3.3.2.2 Rocking curves

The presence of a structural disorder is partially healed by thermal annealing treatments, as also confirmed by rocking curves measurements (Figure 3.5), which leads to a molecular rearrangement towards the bulk phase.

Figure 3.5a reports the comparison between the specular scans performed on PDI8CN2 and N1400 [1.9 mg/mL] films after thermal annealing. The reflectivity behaviour at smaller q is superimposed on a series of Bragg reflections induced by the layered structure of the films. Rocking curves measurements were performed around the 001 and 004 reflections and plotted in Figure 3.5b and 3.5c, respectively, for both films. The scans reveal a broad and a sharp component, both dependent on the Miller index L. The sharp component is the Bragg signal from the average lattice whose FWHM is the measure of the misorientation degree of the crystalline domains. For both films its value is 0.02° that is equals to the angular resolution, meaning that both films have high [001] texturing. The intensity of the sharp component damps when L increases, due to the presence of static disorder [24]. This behaviour is much more pronounced in N1400 film, as expected for the configurational disorder introduced by the asymmetric branched chains. The broad component represents the diffuse scattering, arising from the presence of misfit dislocations. The lager peak width observed for N1400 may be ascribed from the larger amount of defects.

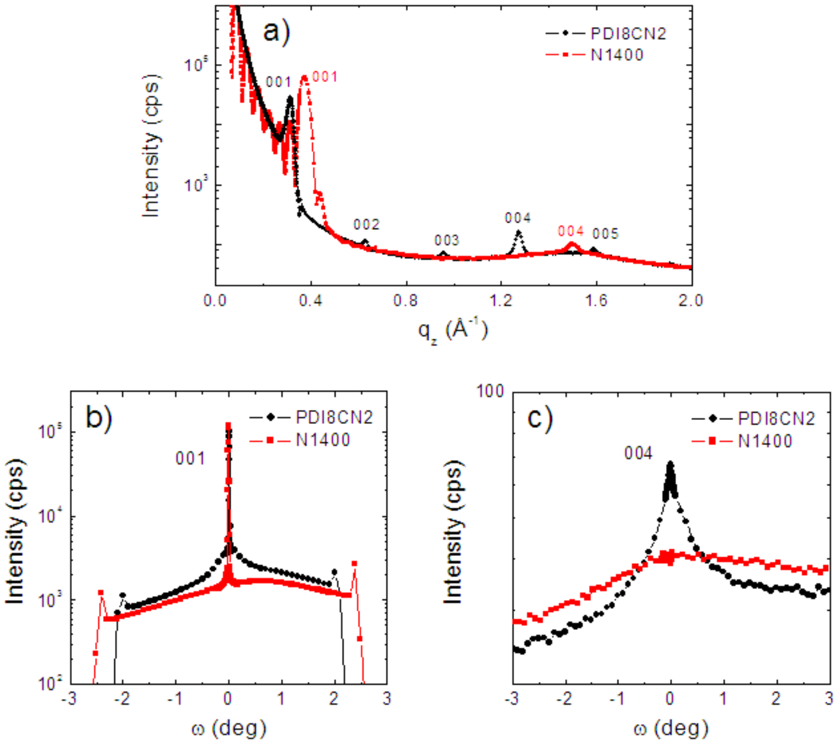

Figure 3.5: a) Specular scans performed on [1.9 mg/mL] PDI8CN2 and N1400 films after thermal annealing. RC intensities at b) 001 and c) 004 reflections.

3.3.2.3 X-ray reflectivity

A quantitative analysis of the film microstructure was performed by carrying out X-Ray Reflectivity (XRR) measurements on films prepared from solutions with different concentrations (from 0.2 to 1.9 mg/mL). The XRR curves recorded for PDI8CN2 and N1400 films before and after annealing are displayed in Figure 3.6a and 3.6b, respectively.

Apart from the N1400 film at the lowest concentration, all XRR curves reveal the presence of the (001) Bragg peak, which progressively intensifies and narrows upon annealing, due to the growth of the crystalline domains along the film thickness, similar to what observed in the 2D-GIXRD experiments for the lateral crystallite dimension. After annealing, the peak position does not change for PDI8CN2 films, whereas it shifts toward the bulk value for N1400 films, confirming the occurrence of the thermally activated phase transition claimed from 2D-GIXRD analysis (Figure 3.3b, 3.3d). The evidence of molecular rearrangement in N1400 films is particularly significant for the film grown from the lowest concentration, where the (001) reflection appears only after annealing. XRR curves also contain information about the film morphology. The Kiessig fringes, i.e. the oscillations observed at low momentum transfer, are characteristic of a film with a rather smooth surface, and its frequency is directly proportional to the film thickness [25, 26]. By fitting these oscillations until $q_z = 0.2\ Å^{-1}$, making use of a single-layer model on top

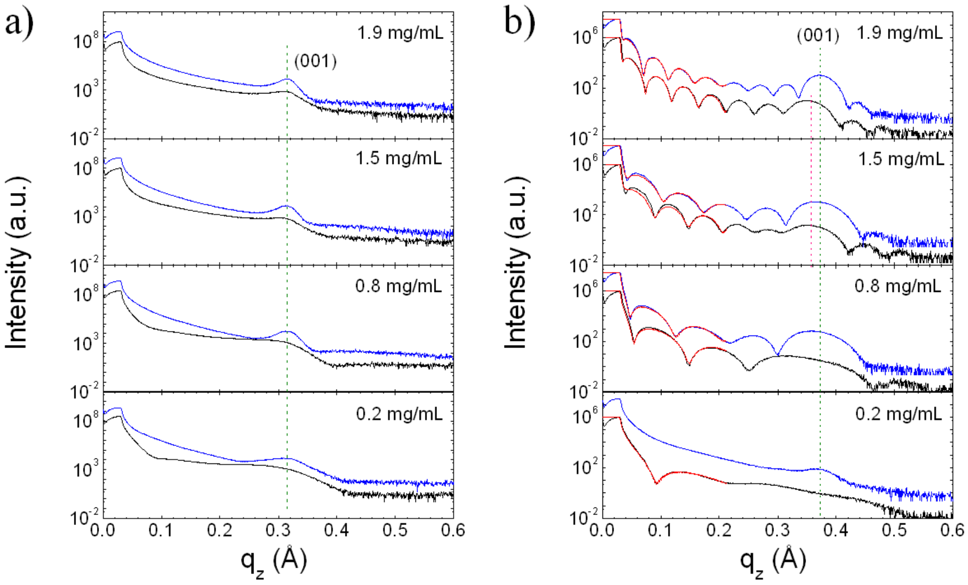

Figure 3.6: XRR curves collected for a) PDI8CN2 and b) N1400 films prepared at various concentrations. Black and blue lines are the data from the as-cast and the annealed film, respectively. Red lines are the fitting curves of Kissieg fringes. Dashed vertical lines indicate the (001) peak position before and after annealing.

of the substrate within the Parratt formalism [26, 27], the thickness and surface roughness (σ_{SURF}) values were extracted. Table 3.1 reports the values of film thickness and surface roughness (σ_{SURF}), extracted by fitting the Kissieg fringes using Parratt formalism [27], the inter-layer spacing (d_{001}) calculated from the Bragg peak position and the vertical crystalline domain size evaluated from the FWHM of Bragg peak or from Laue oscillation period, when present. For all PDI8CN2 films XRR do not show Kissieg fringes, highlighting a 3D island growth with a σ_{SURF} above several nanometres, therefore undetectable by XRR. Conversely, N1400 films are characterized by surfaces with roughnesses on the order of a few $\AA$ only. Film thickness linearly increases with concentration (from 2.9 nm to 12 nm) due to the larger amount of molecules deposited on the surfaces during the casting. When films are annealed, σ_{SURF} slightly increases. This variation is more pronounced at the lowest concentration, where Kissieg fringes disappear after annealing, suggesting a transition from 2D to 3D morphology.

	Concetration [mg/mL]	Thickness (nm)	σ_{surf} (nm)	d_{001} (nm)	D_{perp} (nm)
N1400	1.9	12.06(5)	0.37(2)	1.80(1)	12(3)
	1.5	10.52(3)	0.12(7)	1.79(1)	13(3)
	0.8	6.21(2)	0.12(3)	-	-
	0.2	2.9(2)	0.8(3)	-	-
N1400 after annealing	1.9	11.9(2)	0.34(2)	1.69(1)	12(3)
	1.5	8.06(7)	0.39(2)	1.71(1)	8(3)
	0.8	7.18(9)	0.74(4)	1.74(2)	7(3)
	0.2	-	-	1.72(1)	14(2)
PDI8CN2	1.9	-	-	2.03(2)	17(2)
	1.5	-	-	2.08(4)	15(3)
	0.8	-	-	2.1(1)	11(3)
	0.2	-	-	-	-
PDI8CN2 after annealing	1.9	-	-	2.00(1)	30(1)
	1.5	-	-	2.00(1)	27(2)
	0.8	-	-	2.01(1)	25(2)
	0.2	-	-	2.05(2)	13(2)

Table 3.1: Results of the XRR analysis on N1400 PDICN2 spin-coated films at different concentrations. The errors are reported in the brackets.

3.3.3 The morphology of the films

The microstructure of the films was corroborated by analysing the Atomic Force Microscopy (AFM) images recorded for all films before and after thermal annealing. The AFM images are collectively reported in Figure 3.7, together with the root mean square roughness (σ_{RMS}) values determined for each film as the standard deviation of the film height distribution averaged over three topographic images with a lateral size of 10 μm. For all the concentrations, AFM images of PDI8CN2 films confirm the presence of 3D islands. These consist of rounded-shape grains of several hundreds of nanometers in size, whose average sizes increase with the concentration from 250 nm to 420 nm as deduced from grains analysis. However, they do not appear being drastically modified by the thermal treatment, apart from the [0.2 mg/mL] case, where the lateral size dimension doubles. On the other hand, the morphology of N1400 as-cast films is characterized by very smooth surface whose σ_{RMS}, in the limit of the technique resolution, is comparable with the one extracted from XRR. Thermal treatment induces a morphological change that depends on concentration. For the [1.9 mg/mL] film, σ_{RMS} and grain size remain constant, whereas, when concentration decreases a dewetting phenomenon appears. Dewetting is a well known process [28] occurring when a thin film grows in a metastable phase and the molecules move upon heating, aggregating in a more stable

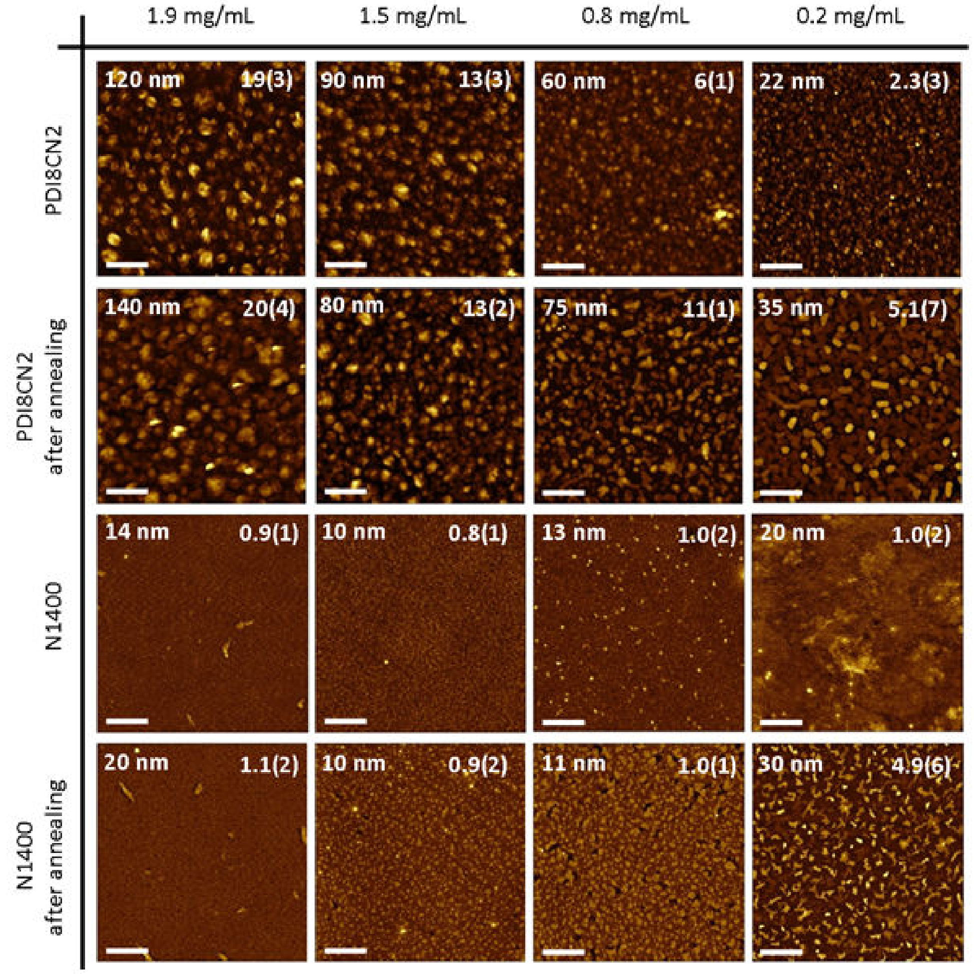

Figure 3.7: AFM images of spin-coated samples at different concentrations of PDI8CN2 and N1400 as-cast and annealed. The white ticks at the bottom correspond to 2 μm. The height of the colour bar (i.e. Z-scale) and σ_{RMS} values, both expressed in nm, are reported as in-set on top-left and top-right, respectively. σ_{RMS} variances are in brackets

phase in the form of islands; this process also leads to formation of holes, which later grow to form dewetted regions. The driving force for this process is the minimization of the total energy of the free surfaces of both the film and substrate, as well as of the film-substrate interface. The rate of dewetting accelerates with lowering the film thickness. Therefore, at lowest concentration thermal treatment transforms the 2 MLs thick film into well-separated 3D crystallites 20 nm high, where molecules are arranged in bulk phase. When concentration increases, the molecular diffusivity decreases and the dewetting phenomenon decreases. The presence of configurational disorder within the N1400 films (that is, the random occurrence of branched side chains of R or S chirality) can be considered being responsible for the growth of the metastable phase; on the contrary, in the case of PDI8CN2, the limited configurational space that can be explored during film growth induces the formation of a unique (stable) phase, less prone to dewetting.

3.3.4 Transport properties of the films

3.3.4.1 Evaluation of the HOMO and LUMO levels

To have a comparison of the energetic levels of the two molecules, absorbance spectra and cyclic voltammetry measurements were performed.

The results of the irradiation experiments are shown in Figure 3.8. The spectra of the two molecules in solution with $CHCl_3$ (Figure 3.8a and 3.8b) are identical and show three peaks in the range 450-570 nm which correspond to the first three electronic (vibronic) transitions (0-0, 0-1 and 0-2 transitions). From the positions of the most intense peaks of the absorbance spectra which correspond to the 0-0 transitions (λ = 524 nm) the semiconductor energy band gap was calculated (E_G = 2.36 eV). After spin-coating 190 μL of a solution onto quartz-substrates, the absorbance spectra show a redshift of the characteristics, slightly more evident in the case of N1400, which contributes to lower the energy band gap of the semiconductors (E_G = 2.25 eV for PDI8CN2 and E_G = 2.19 eV for N1400). From cyclic voltammetry measurements the LUMO level of the two compounds resulted to be 4.1 eV and consequently the HOMO values were estimated to be 6.35 and 6.29 for PDI8CN2 and N1400 respectively.

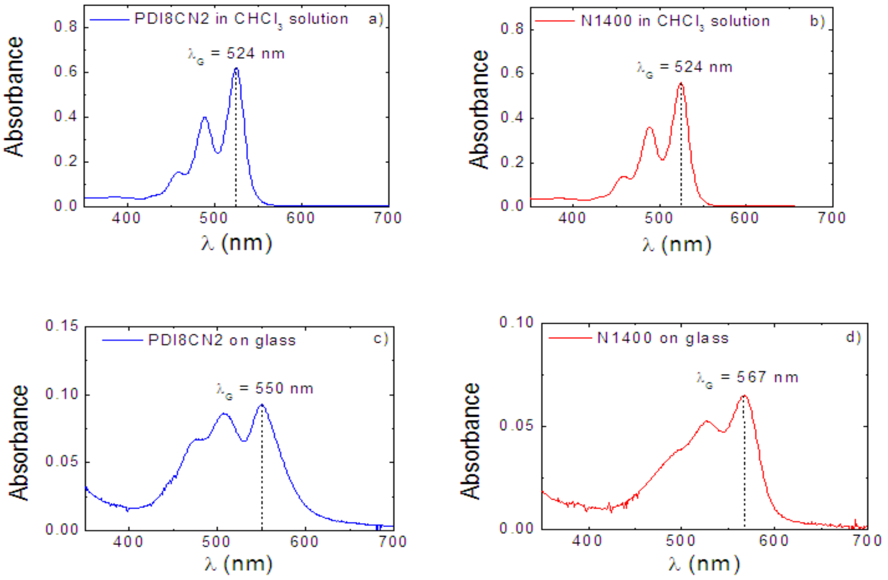

Figure 3.8: Absorbance spectra of PDI8CN2 and N1400 respectively a-b) in solution and c-d) spin-coated on glass substrates.

3.3.4.2 Electrical results on not-functionalized electrodes

The influence of all the structural and morphological characteristics on the electrical properties was investigated by recording output and transfer curves of the OFETs before and after thermal treatment. Figure 3.9 reports the mobility extracted in saturation regime (μ_{sat}) and the threshold voltage (V_{TH}) values as a function of devices channel length (L).

The as-cast PDI8CN2 devices exhibit slightly higher values of μ_{sat} with respect to N1400 ones, because the superior crystalline order observed in these films facilitates the charge carrier transport within the domains. Large and negative V_{TH} are observed in the films before the annealing with PDI8CN2 devices, a behaviour that can be attributed to the numerous traps between not well-connected 3D islands forming the film. Consistently with the structural and morphological findings highlighted above, upon thermal annealing V_{TH} exhibits only a mild (positive) shift for PDI8CN2 devices whilst a remarkably large shift leading to a $V_{TH} \sim 0$ V is observed in N1400 devices. This can be clearly ascribed to a better ability of the N1400 *vs* PDI8CN2 molecules to re-assemble in a thermodynamically stable packing upon annealing. The post-annealing 2D fashion architecture of the N1400 certainly heals the various inter-grain traps centers giving rise to a large threshold voltage. Further, pre-annealing negative sign of V_{TH} could stem from the above-mentioned inter-grain defects that require a higher gate voltage value in order to fill all the trap levels with electrons before a conductive channel is formed. Interestingly, the mobility and threshold voltage variation upon annealing was not concentration-dependent as shown

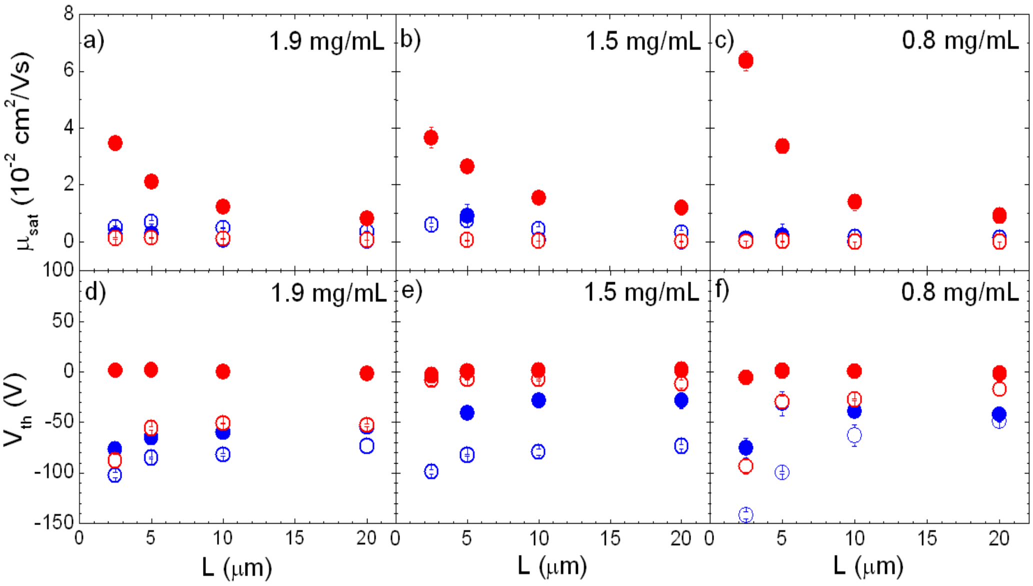

Figure 3.9: Plots of a-c) μ_{sat} and d-f) V_{TH} *vs* channel length (L) of thin-films spin-coated on HMDS-treated SiO_x. Blue and red circles refer to PDI8CN2 and N1400 devices, respectively. Empty and filled circles represent the as-cast devices and the devices after thermal annealing, respectively.

in Figure 3.9. For N1400, a steep decrease of the mobility with increasing the channel length is also observed which cannot be directly correlated with a contact resistance phenomenon. This latter would lead to a mobility decrease with decreasing L given that the channel resistance scales with L whilst the parasitic contact resistance component does not change with the channel length. We ascribed this trend to the increasing occurrence of grain-to-grain hopping events with the increasing of the channel length; this is in line with AFM imaging observations revealing grain sizes typically exceeding 1 μm (after annealing). An additional improvement coming from a better reorganization of the N1400 molecules at the interface with the electrodes after the annealing step is represented by the disappearance of a parasitic resistive contribution that would manifest itself in the transfer curves at high (positive) gate voltages with an unexpected current decrease. In this region the undesired resistive contribution coming from the electrodes (R_c) can become comparable with the channel resistance (R_{ch}) that decreases with driving the device at progressively higher voltages after the V_{TH} is reached. These two beneficial factors clearly dictate the improved performances of the branched-alkyl chains derivative with respect to PDI8CN2. An additional point can be made related to the more pronounced tendency of the threshold voltage to reduce upon increasing the channel length. As the inter-electrodic distance decreases, i.e. L becomes smaller, the corresponding charge density in the (bulk) region of the semiconductor between source and drain contact increases. Provided that charge density ρ and potential ϕ_s are linked by Poisson's equation, the injected amount of charges will induces shift in the electrostatic potential, which requires compensation through a shift in V_{TH} to shut the conduction off. Loosely speaking, to turn off the transistor, the space charge transferred from the electrodes into the bulk of the semiconductor needs to be compensated by an equal and opposite amount of charge accumulated in the channel which translates into a shift in V_{TH}. By and large, the improvement in the OFET performance for both molecules as a result of thermal annealing treatments can be clearly ascribed to the enhanced crystallinity within the films. However, such an improved performance in OFETs observed on the two different molecular films can be explained in view of two markedly different reasons. On the one hand in PDI8CN2 films the crystalline grains increase in size and quality, reducing the grain boundaries density and thus the charge trapping; on the other hand the 3D morphology hinders the percolation between crystalline grains of two separated islands. This explains why after the annealing OFETs based on PDI8CN2 show a mild improve. In contrast, the 2D morphology of N1400 films retain upon annealing allows the charge transport to percolate between the crystalline grains stabilized upon annealing. This is the reason of the strong improvement of the OFET characteristics in N1400 devices. Table 3.3 and 3.4 show examples of electrical characterizations for both molecules before and after annealing at three different concentrations. In the case of N1400-based device it is evident how, independently from the concentration used, the annealing improves the electrical performance by increasing the current I_{SD}, shifting V_{TH} towards 0 V and straightening the transfer characteristics also at high V_{SG} values. On the contrary, the effect of the annealing for PDI8CN2 devices is not so beneficial since it generally lowers the I_{SD} and just slightly shifts V_{TH} towards less negative values.

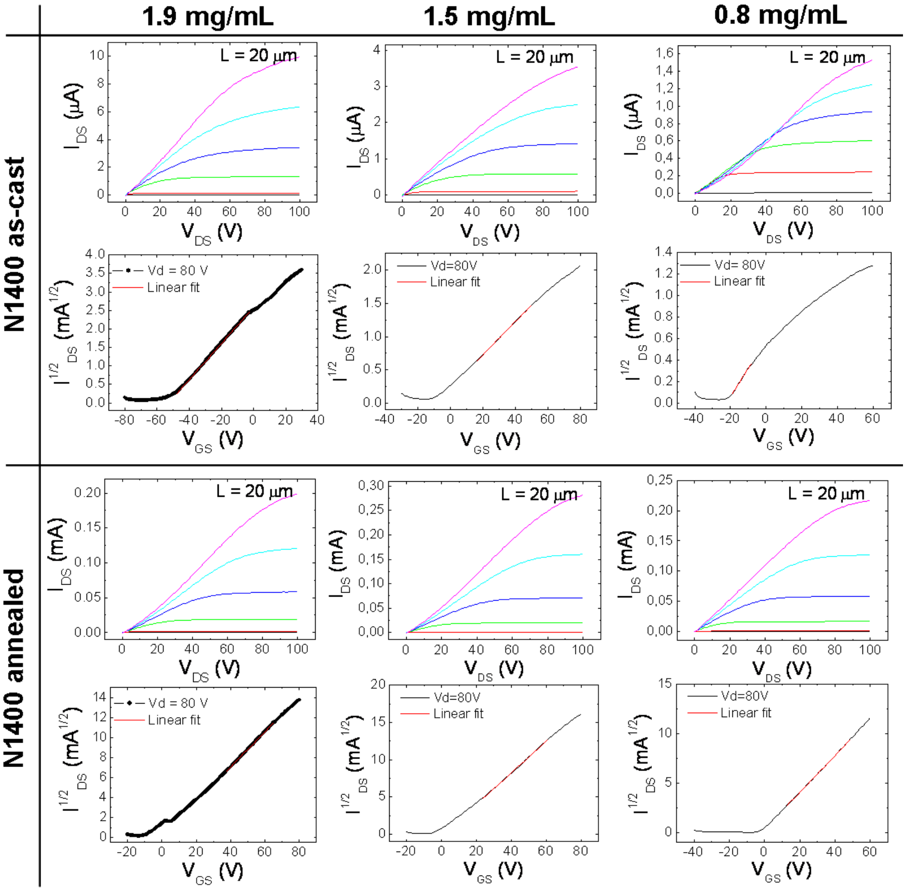

Table 3.3. Examples of output and transfer curves of N1400-based devices before and after annealing at different concentrations; for all the devices L = 20 μm, W = 10 mm.

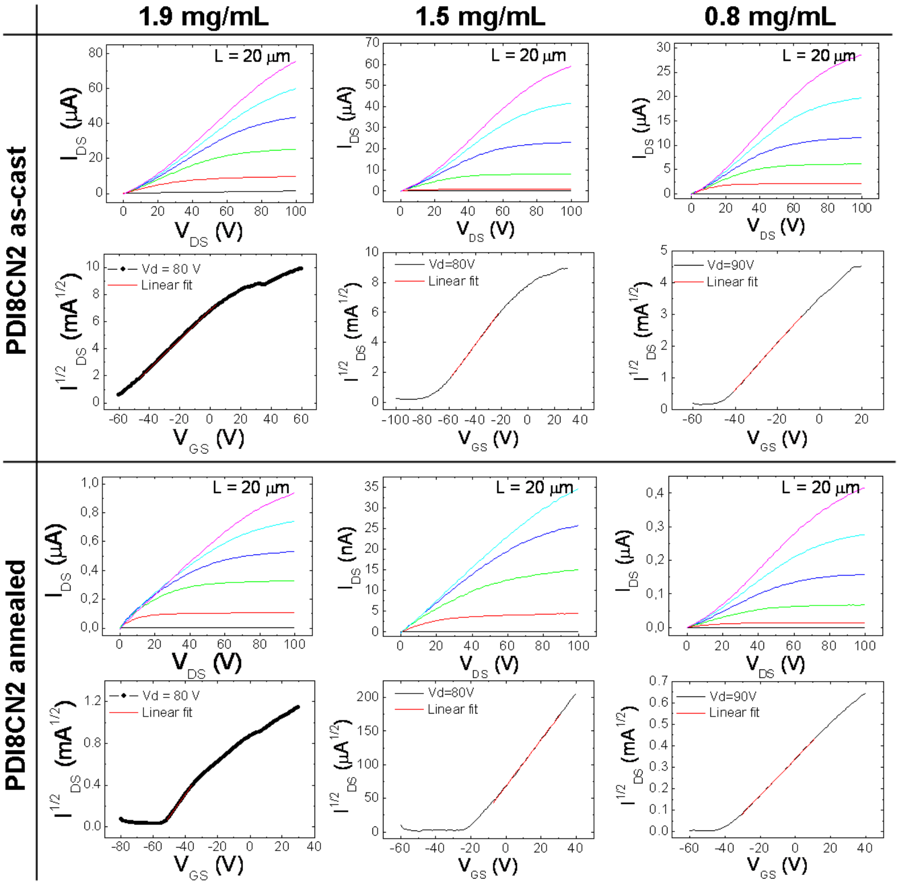

Table 3.4. Examples of output and transfer curves of PDI8CN2-based devices before and after annealing at different concentrations; for all the devices L = 20 μm, W= 10 mm.

3.3.4.3 Electrical results on functionalized electrodes

The source and drain contacts functionalization by means of undecanethiols was performed as described in chapter 1. As schematized in Figure 3.10, this SAM lowers the work function of the gold (Au) electrodes thus favoring the electrons injection from the metal into the LUMO of the molecules.

In Figure 3.11 the mobility calculated in saturation regime (μ_{SAT}) and the threshold voltage (V_{TH}) values as a function of devices channel length (L) are reported. Upon functionalization, the devices which experience a visible improvement of the charge carriers mobility are the PDI8CN2 ones, while the N1400 ones result poorly affected. This behaviour is coherent with what reported so far, because even though the injection barrier is lowered in both cases, the charge transport is still much more difficult in a metastable and disordered film such as N1400 than in a well ordered and compact PDI8CN2 film. The improvements in the threshold voltage values after the electrodes treatment are instead visible in both types of devices. This is most likely due to the fact that a bigger number of charges can overcome the injection barrier and thus traps are filled much faster than

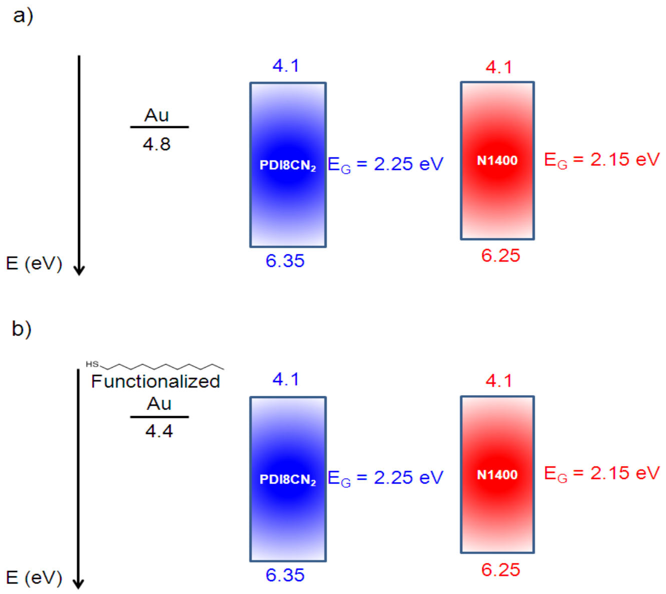

Figure 3.10: Sketch of the HOMO and LUMO energy levels of the two molecules with respect to the gold (Au) work function a) before and b) after the contacts functionalization.

in the untreated devices. Nevertheless, for PDI8CN2 films these values remain slightly higher than for N1400 ones because of their 3D morphology which is responsible for the presence of a high density of charge traps at the grain boundaries.

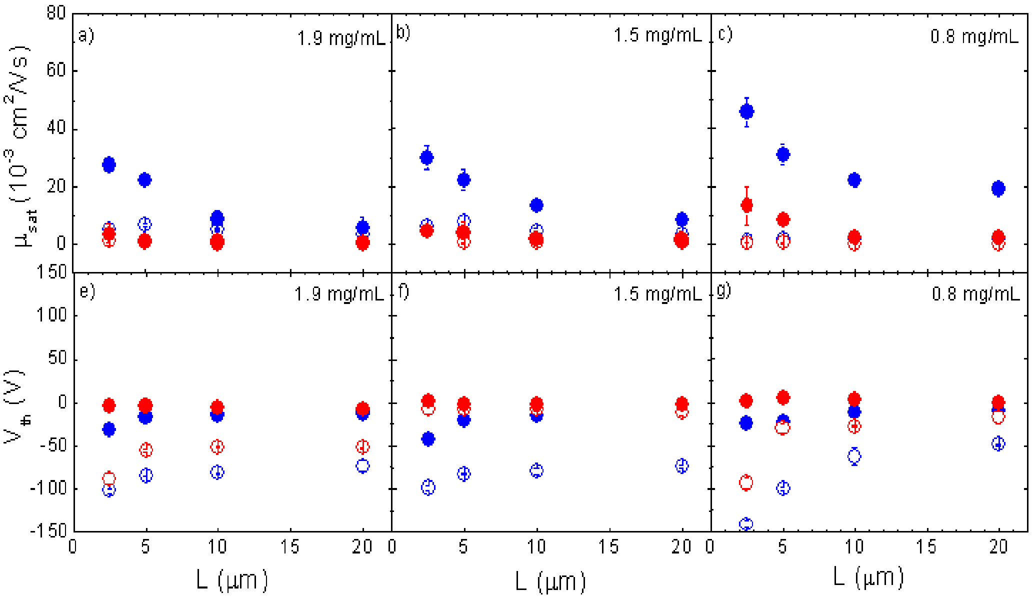

Figure 3.11: Plots of a-c) μ_{sat} and d-f) V_{TH} *vs* channel length (L) of thin-films spin-coated on HMDS-treated SiO_x. Blue and red circles refer to PDI8CN2 and N1400 devices, respectively. Empty and filled circles represent the as-cast devices and the devices after source-drain functionalization, respectively.

3.4 Conclusions

The effect of alkyl side chains architecture of two perylene-diimide derivatives on structure, morphology and electrical properties of spin-coated films was investigated. The responses of the as-casted devices were first compared with annealed ones and then with electrodes functionalized ones. Both X-ray and spectroscopical investigations revealed that the substitution of linear side chains with branched ones, introduces four "distinct" stereoisomers, making the molecules more soluble and therefore increasing their processability. This configurational disorder makes the crystallization process more difficult with respect to the case of molecules with linear side-chains (which self-assembles in the crystal structure optimal for charge transport) and favours the 2D-growth mode. These structural and morphological characteristics, ascribed to branched side chains, enable a phase transition by an ordinary post-deposition thermal treatment which strongly improves the transport properties of thin-film devices. These findings suggest that synthesizing highly processable molecules with strong supramolecular rearrangement capabilities during optimized classical post-growth processes can be more efficient than improving the charge carrier mobility at the expense of solubility.

3.5 Bibliography

[1] R. Schmidt, J. H. Oh, Y. S. Sun, M. Deppisch, A. M. Krause, K. Radacki, H. Braunschweig, M. Konemann, P. Erk, Z. A. Bao and F. Wurthner. *Journal of the American Chemical Society* **131(17)**, 6215–6228 (2009)

[2] C. Piliego, D. Jarzab, G. Gigli, Z. H. Chen, A. Facchetti and M. A. Loi. *Advanced Materials* **21(16)**, 1573–1576 (2009)

[3] R. T. Weitz, K. Amsharov, U. Zschieschang, E. B. Villas, D. K. Goswami, M. Burghard, H. Dosch, M. Jansen, K. Kern and H. Klauk. *Journal of the American Chemical Society* **130(14)**, 4637–4645 (2008)

[4] Y. G. Wen and Y. Q. Liu. *Advanced Materials* **22(12)**, 1331–1345 (2010)

[5] C. Piliego, F. Cordella, D. Jarzab, S. Lu, Z. Chen, A. Facchetti and M. A. Loi. *Applied Physics a-Materials Science & Processing* **95(1)**, 303–308 (2009)

[6] M. L. Tang, J. H. Oh, A. D. Reichardt and Z. N. Bao. *Journal of the American Chemical Society* **131(10)**, 3733–3740 (2009)

[7] J. Rivnay, L. H. Jimison, J. E. Northrup, M. F. Toney, R. Noriega, S. F. Lu, T. J. Marks, A. Facchetti and A. Salleo. *Nature Materials* **8(12)**, 952–958 (2009)

[8] R. C. Savage, E. Orgiu, J. M. Mativetsky, W. Pisula, T. Schnitzler, C. L. Eversloh, C. Li, K. Mullen and P. Samori. *Nanoscale* **4(7)**, 2387–2393 (2012)

[9] B. A. Jones, A. Facchetti, M. R. Wasielewski and T. J. Marks. *Journal of the American Chemical Society* **129(49)**, 15259–15278 (2007)

[10] N. S. An, Y. N. Shi, J. Q. Feng, D. P. Li, J. Gao, Y. L. Chen and X. Y. Li. *Organic Electronics* **14(4)**, 1197–1203 (2013)

[11] P. Samori, A. Fechtenkotter, F. Jackel, T. Bohme, K. Mullen and J. P. Rabe. *Journal of American Chemical Society* **123(46)**, 11462–11467 (2001)

[12] K. Balakrishnan, A. Datar, T. Naddo, J. L. Huang, R. Oitker, M. Yen, J. C. Zhao and L. Zang. *Journal of the American Chemical Society* **128(22)**, 7390–7398 (2006)

[13] F. J. Zhang, Y. B. Hu, T. Schuettfort, C. A. Di, X. K. Gao, C. R. McNeill, L. Thomsen, S. C. B. Mannsfeld, W. Yuan, H. Sirringhaus and D. B. Zhu. *Journal of the American Chemical Society* **135(6)**, 2338–2349 (2013)

[14] F. Liscio, C. Albonetti, K. Broch, A. Shehu, S. D. Quiroga, L. Ferlauto, C. Frank, S. Kowarik, R. Nervo, A. Gerlach, S. Milita, F. Schreibers and F. Biscarini. *Acs Nano* **7(2)**, 1257–1264 (2013)

[15] F. Liscio, S. Milita, C. Albonetti, P. D'Angelo, A. Guagliardi, N. Masciocchi, R. G. Della Valle, E. Venuti, A. Brillante and F. Biscarini. *Advanced Functional Materials* **22(5)**, 943–953 (2012)

[16] B. A. Jones, A. Facchetti, M. R. Wasielewski and T. J. Marks. *Advanced Functional Materials* **18(8)**, 1329–1339 (2008)

[17] M. Cavallini, P. D'Angelo, V. V. Criado, D. Gentili, A. Shehu, F. Leonardi, S. Milita, F. Liscio and F. Biscarini. *Advanced Materials* **23(43)**, 5091–5097 (2011)

[18] P. Zugenmaier, J. Duff and T. L. Bluhm. *Crystal Research and Technology* **35(9)**, 1095–1115 (2000)

[19] H. Lorenz and A. Seidel-Morgenstern. *Thermochimica Acta* **382(1-2)**, 129–142 (2002)

[20] G. Giannini, F. Cuppo, L. Fontanive, N. D'Amelio, A. Cesaro, A. Maiocchi and F. Uggeri. *Journal of Thermal Analysis and Calorimetry* **103(1)**, 89–94 (2011)

[21] D. T. Duong, M. F. Toney and A. Salleo. *Physical Review B* **86(20)** (2012)

[22] B. E. Warren. X-ray diffraction (Dover, New York, 1990)

[23] D. M. Smilgies. *Journal of Applied Crystallography* **42**, 1030–1034 (2009)

[24] B. Nickel, R. Barabash, R. Ruiz, N. Koch, A. Kahn, L. C. Feldman, R. F. Haglund and G. Scoles. *Physical Review B* **70(12)**, 125401 (2004)

[25] H. Kiessig. *Ann. Phys.* **10**, 769 (1931)

[26] P. Colombi, D. K. Agnihotri, V. E. Asadchikov, E. Bontempi, D. K. Bowen, C. H. Chang, L. E. Depero, M. Farnworth, T. Fujimoto, A. Gibaud, M. Jergel, M. Krumrey, T. A. Lafford, A. Lamperti, T. Ma, R. J. Matyi, M. Meduna, S. Milita, K. Sakurai, L. Shabel'nikov, A. Ulyanenkov, A. Van der Lee and C. Wiemer. *Journal of Applied Crystallography* **41**, 143–152 (2008)

[27] L. G. Parratt. *Physical Review* **95(2)**, 359–369 (1954)

[28] C. V. Thompson. *Annual Review of Materials Research, Vol 42* **42**, 399–434 (2012)

CHAPTER 4

AMBIPOLAR OFETS BASED ON SOLUTION PROCESSED POLYMERIC BILAYERS

In this chapter the fabrication and characterization of ambipolar devices based on the superposition of n-type and p-type polymeric layers deposited from solution is presented. At first, the caracterization of OFETs based on the single polymeric layers was carried out to define the general behavior of the materials.

4.1 Introduction

In recent years, the fast evolution on design and characterization of n-type organic materials has moved more and more attention towards the fabrication of ambipolars OFETs. Moreover, the incorporation of n- and p-channel in the same structure opens up the field of organic light emitting field-effect transistors (OLETs) that combine electrical switching and light emission in the same device [1–3]. Ambipolars can be fabricated by using single organic materials presenting both electrons and holes transport [4], binary blends [5] or bilayer structures. Recently it has been demonstrated an ambipolar device based on parallel nanofibers of p- and n-type conducting polymers acting as isolated channels for holes and electrons to avoid charge recombination [6]. Among bilayer ambipolars there are several examples [7] in literature which follow the pioneering cases of Dodabalapur and co-workers [8–11]. From then on, many advances have been made also thanks to device optimization, that includes the fabrication of source and drain electrodes with different metals to improve charge injection for both carriers [12]. Up to now, all the studies presented on ambipolar bilayes rely on vacuum deposited organic materials. The deposition of both p- and n-type layer from solution with a technique allowing to control the film thickness thus represents an enormous improvement in view of large area fabrication and compatibility with flexible substrates.

4.2 Experimental

4.2.1 Active Materials

The commercial polymers adopted for this study are P(NDI2OD-T2), i.e. poly[N,N′-bis(2-octyldodecyl)-naphthalene-1′4′5′8-bis(dicarboximide)-2,6-diyl]-alt-5,5′-(2,2′-bithiophene) (Polyera ActivInk N2200), and IIDDT-C3, a 6,6′ isoindigo-based conjugated polymer 4-decyltetradecyl (1-Material) (Figure 4.1). P(NDI2OD-T2) is a well known n-type polymer obtained by the copolymerization of naphtalene diimide and bithiophene. The large planar unit entails good ambient stability, performance and versatility, as demonstrated by the numerous recent publications on this material [13–19]. Isoindigo is a unit composed of two oxindole rings connected by a double carbon bond and it has recently been exploited in organic electronics thanks to its excellent stability and capability in formation of large crystalline fibrillar networks characterized by strong π-π interactions [20–22].

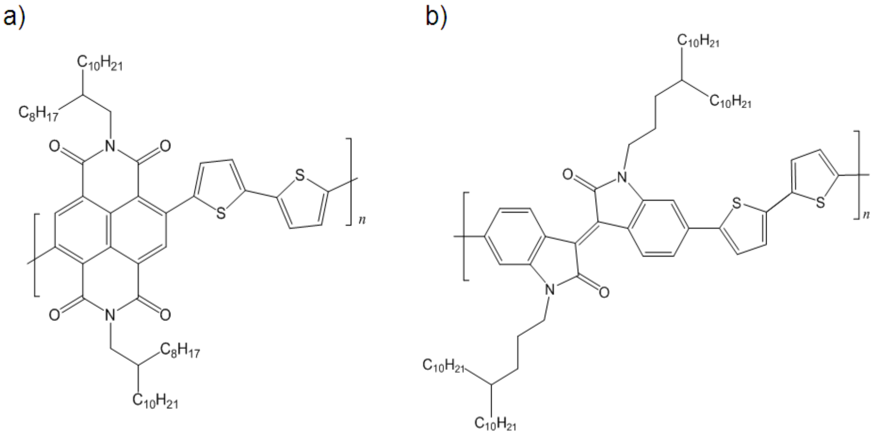

Figure 4.1: Chemical structures of a) N2200 and b) IIDDT-C3.

4.2.2 Device fabrication

The deposition method adopted for both n- and p-type layers from solutions was the Langmuir-Schaefer (LS) technique (described in Chapter 2). All the silicon substrates with 230 nm of silicon oxide as dielectric (Fraunhofer IPMS, Dresden, Germany) were cleaned in ambient conditions by acetone and isopropanol and then dried off using a gentle nitrogen flow. The device surface was then activated by 5 minutes of ozone treatment plus 25 minutes of incubation and at the end functionalized by OTS as descript in Chapter 1. The deposition conditions used for the two materials are the following:

- $\sim$ 1 mono-layer (ML) of N2200: 120 μL of solution 0.25 mg/mL in $CHCl_3$, surface pressure deposition of 20 mN/m;
- $\sim$ 3 MLs of N2200: the same procedure as before but repeated for three times;

- $\sim$ 1 ML of IIDDT-C3: 50 μL of solution 0.5 mg/mL in $CHCl_3$, surface pressure deposition of 25 mN/m;
- $\sim$ 3 MLs of IIDDT-C3: 100 μL of solution 0.5 mg/mL in $CHCl_3$, surface pressure deposition of 35 mN/m.

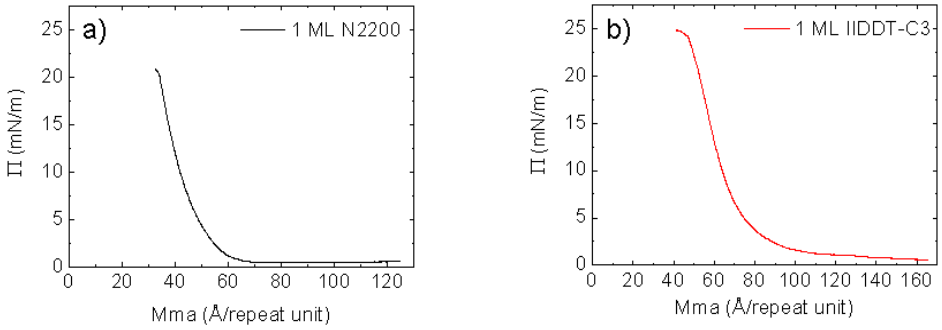

Figure 4.2: Isotherms (i.e. plots of the surface pressure *vs* mean molecular area) before the deposition of a) $\sim$ 1 ML of N2200 and b) $\sim$ 1 ML of IIDDT-C3.

Figure 4.2 illustrates two typical isotherms acquired just before the deposition of a nominal layer of N2200 (left) and IIDDT-C3 (right). The rising of the surface pressure Π indicates the transition from a phase in which the monomers are totally dispersed, which is related to high values of the surface area occupied by each monomer (Mma), to a phase in which they start to organize in a film, i.e. lower Mma. When the desired Π is reached, the barriers stop compressing the film to allow the deposition and the measurement of the surface pressure in interrupt.

4.2.3 Characterization methods

4.2.3.1 X-ray diffraction measurements

All the 2D-GIXRD images presented here were collected at the beamline XRD1 of ELETTRA synchrotron facility (Trieste, Italy) by using a wavelength of 1.55 $\AA$ and a beam size of 200x200 μm^2. The incident angle of the X-ray beam, α_i, was chosen close to the critical angle to discriminate the contribution to the diffraction pattern coming from the upper layers of the organic film and that coming from the substrate. The 2D-GIXRD diffraction patterns were recorded using a 2D camera (Pilatus detector) placed normal to the incident beam direction and at two different distances from the sample (D = 200 mm and D = 470 mm) were chosen in order to detect any Bragg reflection both in the wide and small angle region of the reciprocal space. In particular the images collected at D = 470 mm allows to probe a small portion of the reciprocal space, then to have a better resolution on small scattering vectors $\vec{q}$ (i.e. large d-spacing between lattice planes).

4.2.3.2 X-ray reflectivity measurements

XRRs were performed using a SmartLab Rigaku diffractometer in a parallel beam geometry equipped with a CuK_α (λ = 1.5418 $\AA$) rotating anode followed by a parabolic mirror to collimate the incident beam and a series of variable slits (placed before and after the sample position) to obtain an acceptance of 0.02°.

4.2.3.3 Morphological characterization

Topographical AFM characterization was carried out in intermittent contact mode in air environment making use of a Veeco Dimension 3100 operating on a Nanoscope IV control unit.

4.2.3.4 Electrical characterization

The electrical behavior of all bottom gate-top contacts devices was tested in nitrogen atmosphere by collecting output and transfer characteristics and comparing the mobility and threshold voltage values obtained both in linear and saturation regimes.

4.3 Results and discussion

4.3.1 The single N2200 layer

4.3.1.1 Crystalline structure

Figure 4.3 presents the structural characterization of a N2200 film with nominal thickness of 1 ML deposited by LS technique on OTS-treated SiO_2. The as-cast film (Figure 4.3 a and b) shows two spots in the specular (q_z) direction corresponding to the (100) and (200) reflections that are related to a periodicity of 2.5 nm along the surface normal. In the q_{xy} direction, independently from the portion of the reciprocal space probed, there is only a rod detectable at q_{xy} = 0.46 $\AA^{-1}$ (001) and it is related to the chain backbone repetition [17]. These characteristics are clearer after a thermal treatment at 150° C overnight in vacuum oven, as indicated in Figure 4.3 c and d. The reflections already present in the as-cast film are intensified and a new spot at q_z = 0.76 $\AA^{-1}$ is starting to appear.
The presence of the lamella stacking in the q_z direction and the rod related to the chain backbone in the q_xy direction indicate that the N2200 polymer chains deposited by LS technique organize in an edge-on configuration (Figure 4.4) with respect to the substrate surface.

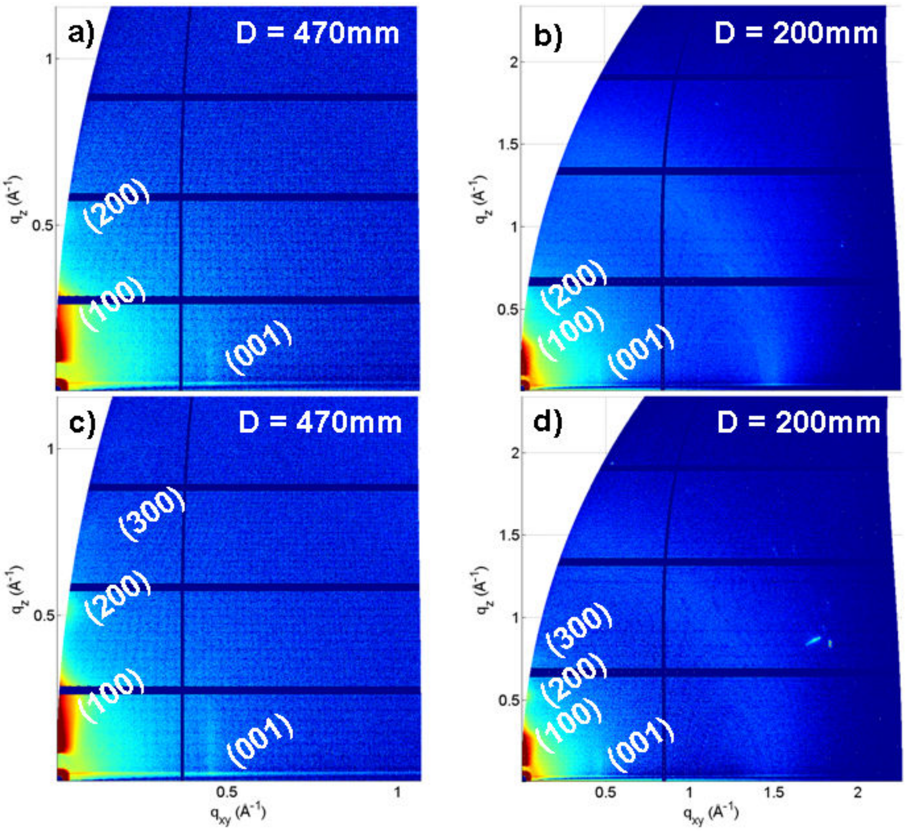

Figure 4.3: a-b) 2D-GIXRD images of ∼ 1 ML of N2200 at sample-detector distance D = 470 mm and D = 200 mm respectively; c-d) 2D-GIXRD images of ∼ 1 ML of N2200 after annealing at 150 °C overnight in vacuum oven at sample-detector distance D = 470 mm and D = 200 mm respectively. The logarithmic scale of colours is the same for all the images as well as the incident angle α_i = 0.18°.

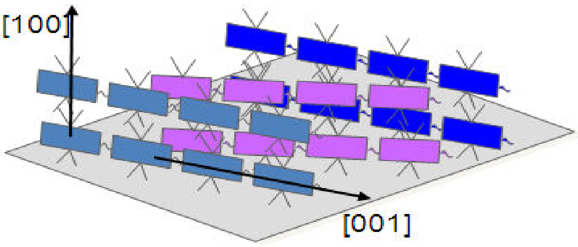

Figure 4.4: Sketch of the edge-on N2200 lamella organization.

In the 2D-GIXRD images collected for thicker films (3 MLs of nominal thickness) (100), (200) and (001) reflections appear stronger (Figure 4.5a). These characteristics are even more pronounced after the annealing (Figure 4.5c) where the rod at q_{xy} = 0.46 $\AA^{-1}$ now is clearly visible as well as more orders of the (h00) family of lattice planes, indicating an improvement in the crystalline order of the organic film. Measurements at D = 200 mm of the as-cast film (Figure 4.5b) reveal the presence of several rings probably associated to the formation of polycrystalline grains of a polymorph on top of the initial layer of film which instead has edge-on configuration (Figure 4.4). All rings disappear after thermal treatment (Figure 4.5d) suggesting a reorganization of the polymer packing. The annealing also promotes the appearance of another rod in the q_{xy} direction corresponding to the $(002)'$ reflection (q_{xy} = 1.76 $\AA^{-1}$) ascribed to the chain backbone in-plane arrangement of a polymorph [23].

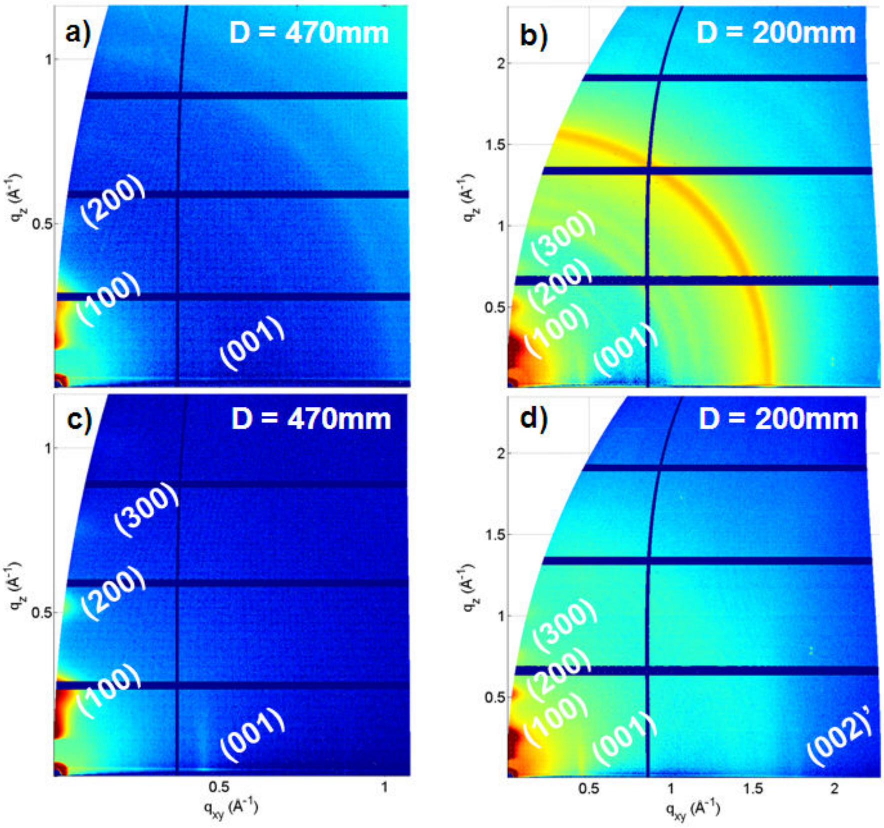

Figure 4.5: a-b) 2D-GIXRD images of $\sim$ 3 MLs of N2200 at sample-detector distance D = 470 mm and D = 200 mm respectively; c-d) 2D-GIXRD images of $\sim$ 3 MLs of N2200 after annealing at 150 °C overnight in vacuum oven at sample-detector distance D = 470 mm and D = 200 mm respectively. The logarithmic scale of colours is the same for all the images as well as the incident angle α_i = 0.18°.

4.3.1.2 X-ray reflectivity

X-ray reflectivity measurements performed on nominal 1 ML thick N2200 film both before and after annealing are shown in Figure 4.6a and 4.6b respectively. A partial fit of the XRR data was obtained by using a single-layer model on top of the silicon substrate with the Rigaku software based on the Parratt's formalism. The entire fit of the XRRs was not possible due to the presence of the (100) and (200) Bragg reflections around $q_z = 0.25\AA^{-1}$ and $q_z = 0.5\AA^{-1}$ (black arrows). The thickness estimated from the fit resulted to be around 4.2 nm for the as-casted film and around 3 nm for the annealed one. These values are higher than 1 ML thickness (2.5 nm) and therefore they justify the presence of (h00) reflections in the specular region which are not expected from single-layer films.

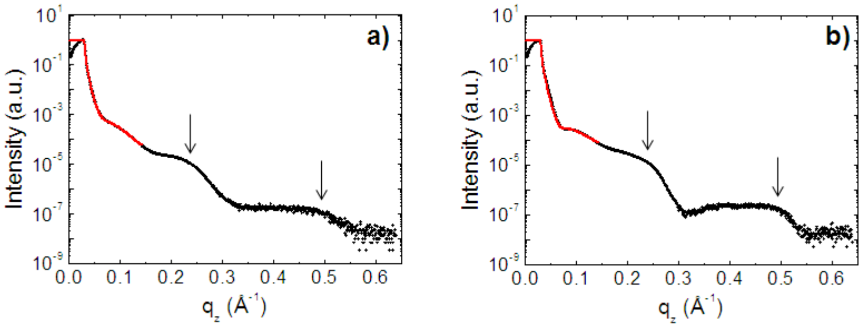

Figure 4.6: XRR measurement of nominal 1 ML N2200 thin-film deposited by LS technique a) before and b) after thermal treatment.

These extrapolated values suggest that the thermal treatment contributes to lower the film thickness, which could be correlated to a reorganization of the molecules towards a smoother morphology.

4.3.1.3 Morphology

The morphology of the nominal single-layer N2200 film (Figure 4.7a) reveals the presence of a great number of holes and aggregates sometimes reaching several tens of nm in height. The film is in fact nor homogeneous neither continuous and it is characterized by a surface roughness of 3 nm. After an annealing at 150 °C overnight in vacuum oven the topography of the film results remarkably different (Figure 4.7b). The number of holes is drastically diminished, the film looks continuous and the surface roughness is lowered to 1.7 nm. This result indicates that during the annealing a molecular reorganization takes place leading to a more homogeneous distribution of the polymer on the substrate surface, as already deduced from XRR analysis.

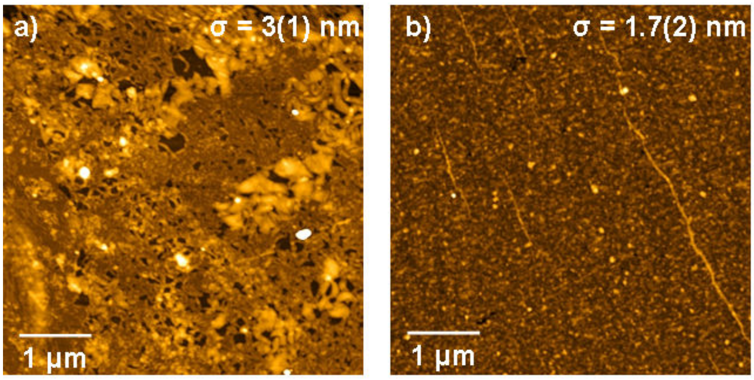

Figure 4.7: 5x5 μm^2 AFM images of nominal single-layer N2200 film a) before and b) after annealing at 150 °C overnight in vacuum oven. Both films were deposited by LS technique.

4.3.1.4 Electrical properties

The electrical characteristics of OFETs based on N2200 at different nominal thickness (from 1ML to 3MLs) were recorded both before and after thermal treatment to detect possible improvements related to the molecular reorganization. μ, V_{TH} and I_{ON}/I_{OFF} values were calculated from the transfer curves both in linear (V_{SD} = 10 V) and saturation (V_{SD} = 50 V) regimes. Nominal 1 ML N2200 film is characterized by a μ of 10^{-3} cm^2/Vs, a V_{TH} around 50 V and a maximum I_{ON}/I_{OFF} of 10^4 (Figure 4.8a).

Upon increasing of the nominal film thickness from 1ML to 2MLs , μ improves of one order of magnitude going from 10^{-3} to 10^{-2} cm^2/Vs, V_{TH} increments from $\sim$ 50 to $\sim$ 60 V and I_{ON}/I_{OFF} remains comparable to the previous case. A further increasing of the film thickness up to $\sim$ 3 MLs slightly improves μ and V_{TH}. This enhancement is related to the fact that with the addition of semiconducting layers the possible number of percolation paths for the charge carriers increments, thus improving their mobility. However, by repeating the LS deposition protocol several times, polycrystalline domains are formed, limiting the improvement of the V_{TH} for the highest thickness. The effect of the annealing at 150 °C overnight in vacuum oven is to drastically boost the electrons mobility, as reported in Figure 4.9. With respect to the as-casted case, the nominal single-layer film after thermal treatment (Figure 4.9a) shows a mobility improvement of one order of magnitude, going then from 10^{-3} to 10^{-2} cm^2/Vs, a slight increasing of V_{TH} and a decreasing of the I_{ON}/I_{OFF} of at least one order of magnitude. The boosting of the charge carrier mobility after annealing is related to the change in the film morphology and to the improvement in crystallinity. Upon increasing of the organic layers (Figure 4.9b and 4.9c), the mobility easily reaches 10^{-1} cm^2/Vs whereas the V_{TH} and I_{ON}/I_{OFF} remain roughly the same.

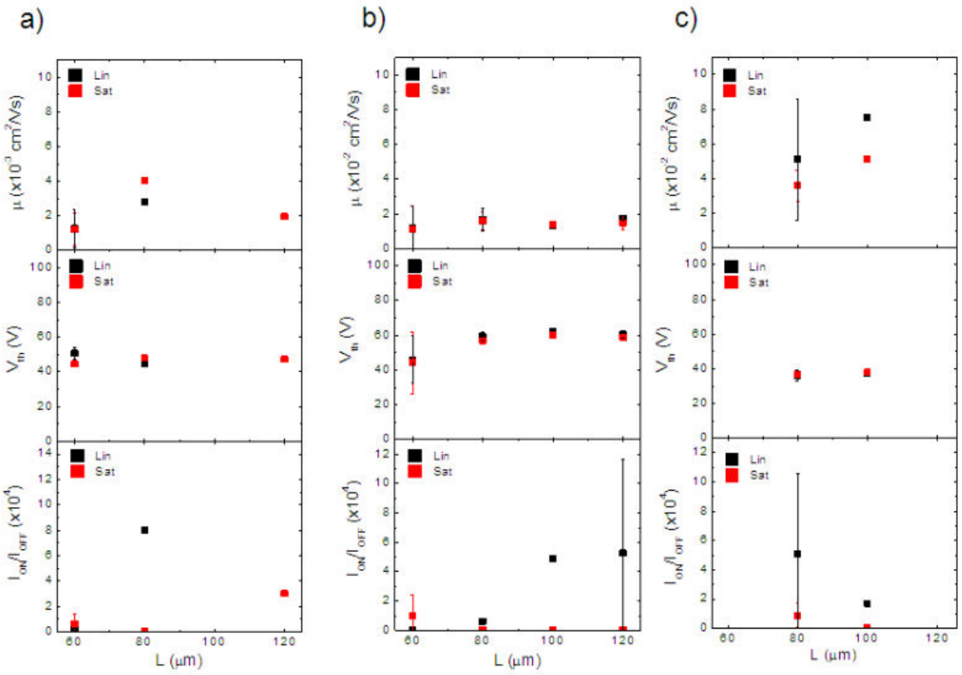

Figure 4.8: Electrical results of a) 1 ML, b) 2 MLs and c) 3MLs of N2200 thin-films deposited by LS technique on OTS-treated substrate.

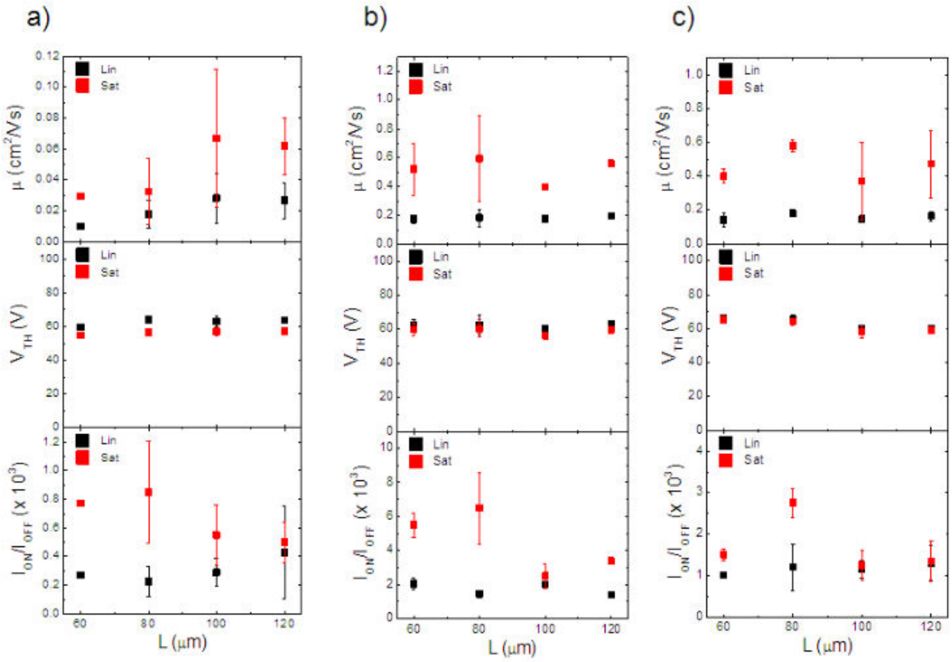

Figure 4.9: Electrical results of a) ∼ 1 ML, b) ∼ 2 MLs and c) ∼ 3 MLs of N2200 thin-films deposited by LS technique on OTS-treated substrate and annealed at 150 °C overnight in vacuum oven.

4.3.2 The single IIDDT-C3 layer

4.3.2.1 Morphology

The morphology of 1 ML IIDDT-C3 film (Figure 4.10a) is characterized by a smooth (σ_{RMS} = 0.6 nm) and compact surface. Despite the consistent number of holes, the film is more homogeneous than the corresponding n-type counterpart (Figure 4.7a). The deposition of multiple IIDDT-C3 layers one on top of the other (Figure 4.10b) increments the surface roughness (σ_{RMS} = 1.2 nm) but at the same time contributes to cover all the holes. In both samples, the characteristic IIDDT-C3 chains present a general preferential growth direction which is strictly related to the deposition technique. In fact, in the LS apparatus (Figure 2.2) the closure of the barriers compresses the molecules on the water surface imposing them to adopt a configuration which optimize the film formation. Polymer aggregates as fiber aligned perpendicularly to the direction of the pressure barriers.

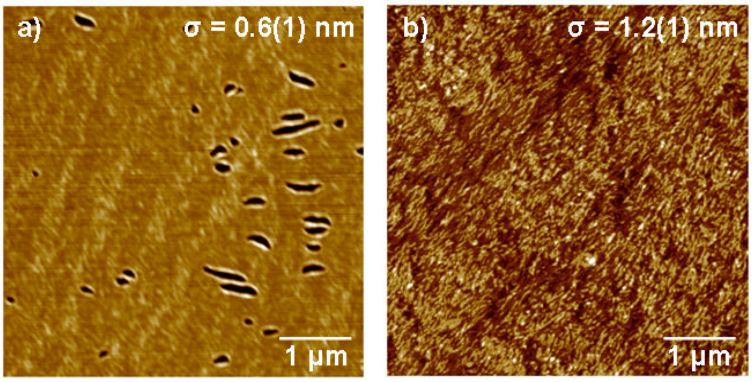

Figure 4.10: 5x5 μm^2 AFM images of a) 1 ML of IIDDT-C3 film and b) 3 MLs IIDDT-C3 film deposited by LS technique.

4.3.2.2 Crystalline structure

As in the case of N2200, 1 ML and 3 MLs thin-films of IIDDT-C3 were structurally characterized at two different D to better probe different zones of the reciprocal space. In the cases at D = 200 mm, the samples were also rotated of 90° with respect to the incoming beam direction (angle ϕ). Diffraction patterns were collected with ϕ = 0° and ϕ = 90°, i.e. the beam direction was perpendicular and parallel to the polymer fibers, respectively. Figure 4.11 shows the data coming from 1 ML of IIDDT-C3 at D = 470 mm (a) and D = 200 mm (b-c). In q_z direction, (h00) reflections related to the lamella stacking, are detectable in all the three images (even though at 470 mm one is partially hidden by the dead zone of the detector), but in the q_{xy} direction no Bragg reflections are appreciable.

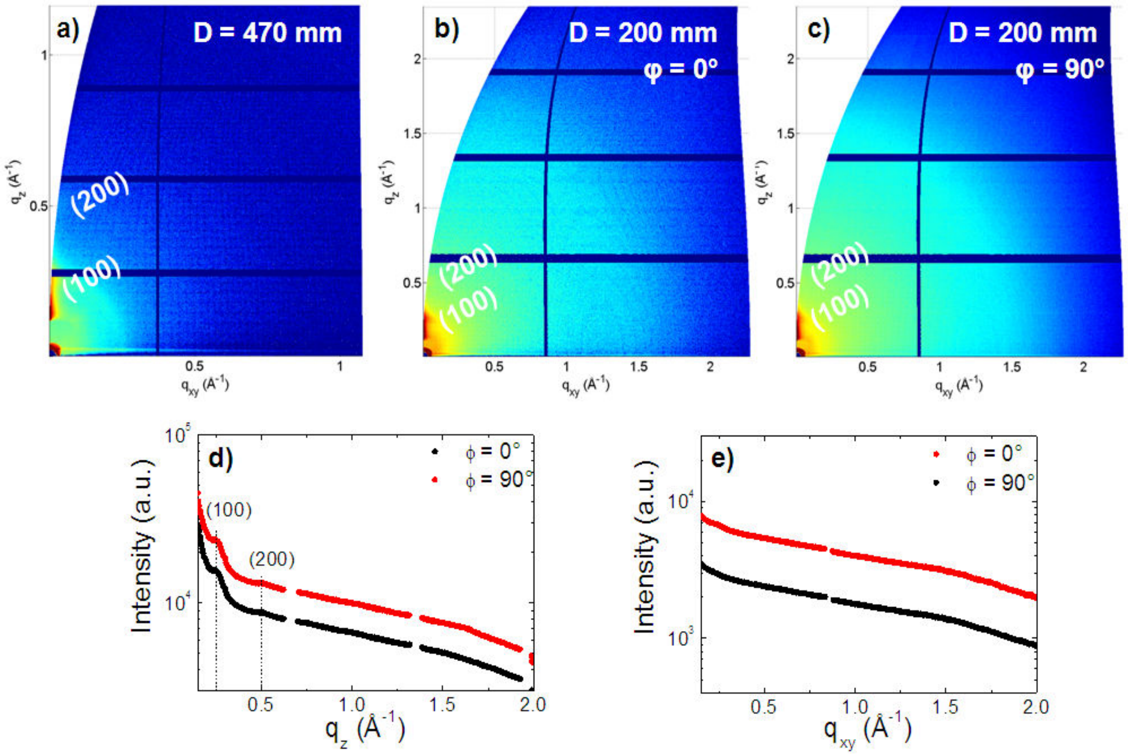

Figure 4.11: Structural investigation of 1 ML of IIDDT-C3 deposited by LS technique: 2D-GIXRD image at sample detector distance a) D = 470 mm and b-c) D = 200 mm; scattering intensity at D = 200 mm integrated along d) the specular direction (q_z) and e) along Yoneda (q_{xy}). ϕ indicates the reciprocal direction of the incoming X-ray beam and the IIDDT-C3 fibers: for $\phi = 0°$ they are perpendicular and for $\phi = 90°$ they are parallel. The scattering intensity integrations were extrapolated before the image transformations.

Other 2D-GIXRD measurements were carried out on a thicker sample (Figure 4.12) to try to improve the signal coming from the material and better understand the polymer packing orientation on the substrate surface. Also in this case, the image at D = 470 mm (Figure 4.12a) shows reflections in the q_z direction related to the (h00) family of planes, i.e the lamella stacking, and absolutely no signals in the q_{xy} direction related to the chain backbone, differently from the N2200 case (Figure 4.5). Nevertheless, this time at D = 200 mm a rod at the Yoneda ascribed to the π-π stacking between lamella is detectable in Figure 4.12c and totally absent in Figure 4.12b. The detection of the π-π reflection when the beam is parallel the fibers indicates that LS technique induces the π-π stacking formation more or less perpendicular to the fiber growth direction. As in the N2200 case, these GIXRD measurements indicate that the IIDDT-C3 lamellae tend to organize in an edge-on configuration (Figure 4.13) with lamella stacking of 2.5 nm and a π-π distance of 3.6 $\AA$. The strong π-π stacking very similar to small molecules is due to the position of the alkyl chains branching point away from the backbone [21], which ensures a good interaction between the lamella cores.

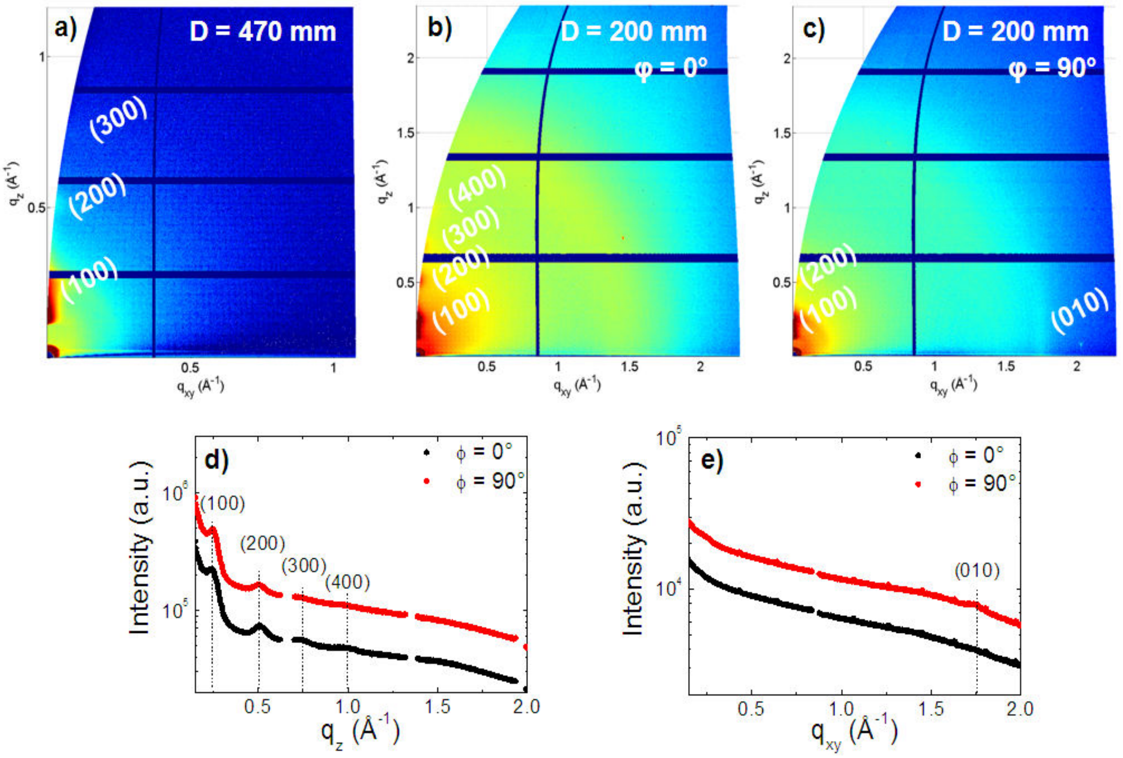

Figure 4.12: Structural investigation of 3 ML of IIDDT-C3 deposited by LS technique: 2D-GIXRD image at sample detector distance a) D = 470 mm and b-c) D = 200 mm; scattering intensity at D = 200 mm integrated along d) the specular direction (q_z) and e) along Yoneda (q_{xy}). ϕ indicates the reciprocal direction of the incoming X-ray beam and the IIDDT-C3 fibers: for ϕ = 0° they are perpendicular and for ϕ = 90° they are parallel. The scattering intensity integrations were extrapolated before the image transformations.

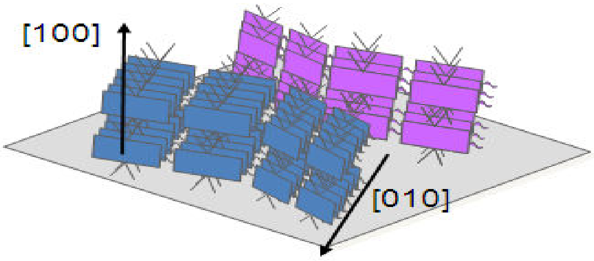

Figure 4.13: Sketch of the edge-on IIDDT-C3 lamella organization.

4.3.2.3 X-ray reflectivity

X-ray reflectivity measurements performed on a single and a triple layer of IIDDT-C3 are shown in Figure 4.14a and 4.14b respectively. As in the case of N2200, the entire sets of data could not be fitted due to the presence of the (100) and (200) Bragg reflections around q_z = 0.25 $Å^{-1}$ and q_z = 0.5 $Å^{-1}$ (indicated by the black arrows). The estimation of the film thicknesses from a partial fit of the XRR data gave values around 4.7 nm for the 1 ML and around 8 nm for the 3 MLs, just a little bit higher than the nominal values.

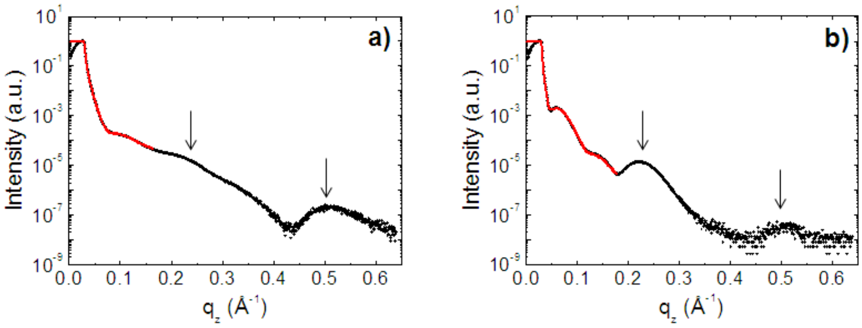

Figure 4.14: XRR measurement of a) 1 ML and b) 3 MLs of IIDDT-C3 deposited by LS technique on OTS-treated SiO_2 substrates.

4.3.2.4 Electrical behavior

The electrical behaviour in linear (V_{SD} = -10V) and saturation (V_{SD} = -50V) regimes of single and triple IIDDT-C3 layers is summarized in Figure 4.15. Upon increasing of the film thickness the μ gains one order of magnitude (from 10^{-2} to $10^{-1} cm^2$/Vs) and the V_{TH} slightly decreases of roughly 10 V, whereas the I_{ON}/I_{OFF} remains in the range $10^5 - 10^6$. The electrical improvements are presumably due to the coverage of all the morphological discontinuities present in single layer devices and thus on the creation of continuous percolation paths for charge carriers.

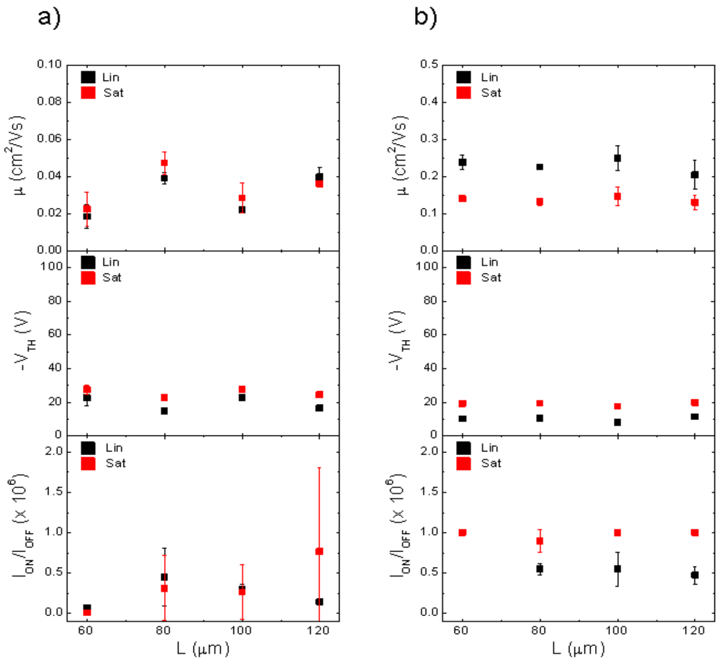

Figure 4.15: Electrical results of a) 1 ML and b) 3 MLs of IIDDT-C3 thin-films deposited by LS technique on OTS treated substrate.

The charge carrier mobility of IIDDT-C3 as-cast devices is in line with the one extrapolated from N2200 annealed ones. With respect to N2200, IIDDT-C3 structure (Figure 4.1) presents an alkyl chains branching point more distant to the chainbone and this favors a close packing between lamella which ultimately translates in good charge carriers mobility already in the as-cast thin-films.

4.3.3 The bilayers

The ambipolar bilayers were fabricated by depositing the p-type polymeric material on top of the n-type one (or vice versa) entirely by LS technique. The combinations studied are schematized in Figure 4.16.

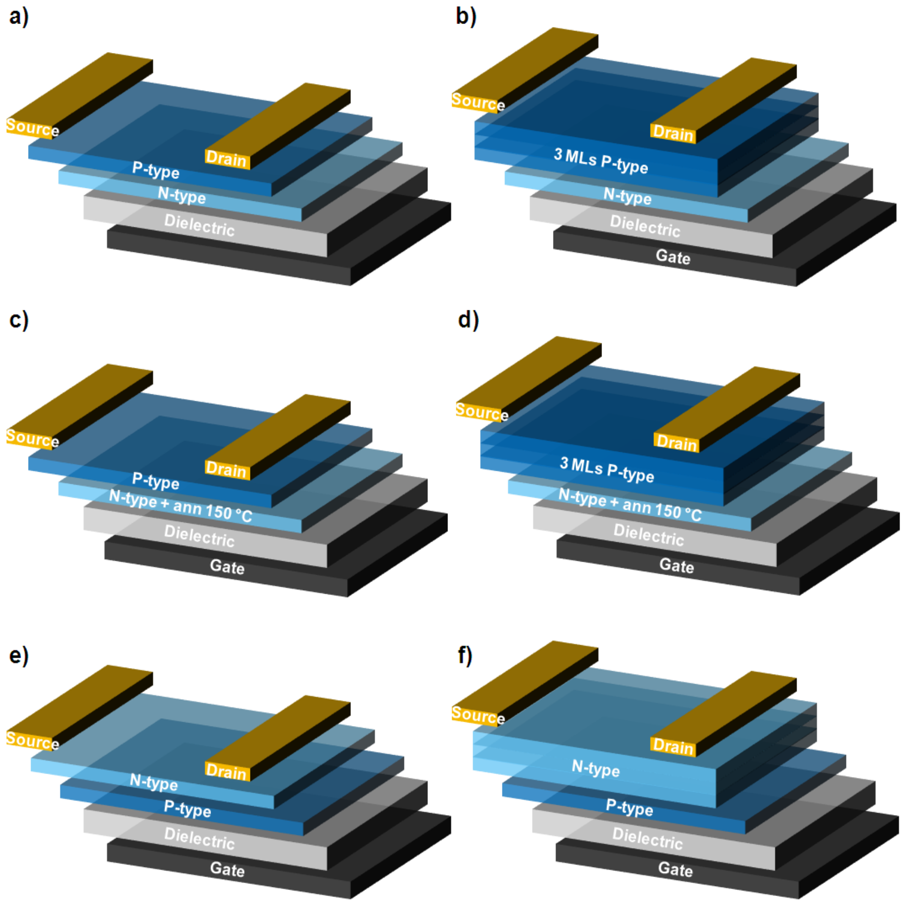

Figure 4.16: Schematic structures of the ambipolar bilayers fabricated: a) 1 ML N2200 + 1 ML IIDDT-C3; b) 1 ML N2200 + 3 MLs IIDDT-C3; c) 1 ML N2200 annealed at 150 °C + 1 ML IIDDT-C3; d) 1 ML N2200 annealed at 150 °C + 3 MLs IIDDT-C3; e) 1 ML IIDDT-C3 + 1 ML N2200; f) 1 ML IIDDT-C3 + 3 ML N2200.

4.3.3.1 Crystalline structure

The results of the structural investigation carried out on bilayers c-f of Figure 4.16 are presented in Figure 4.17.

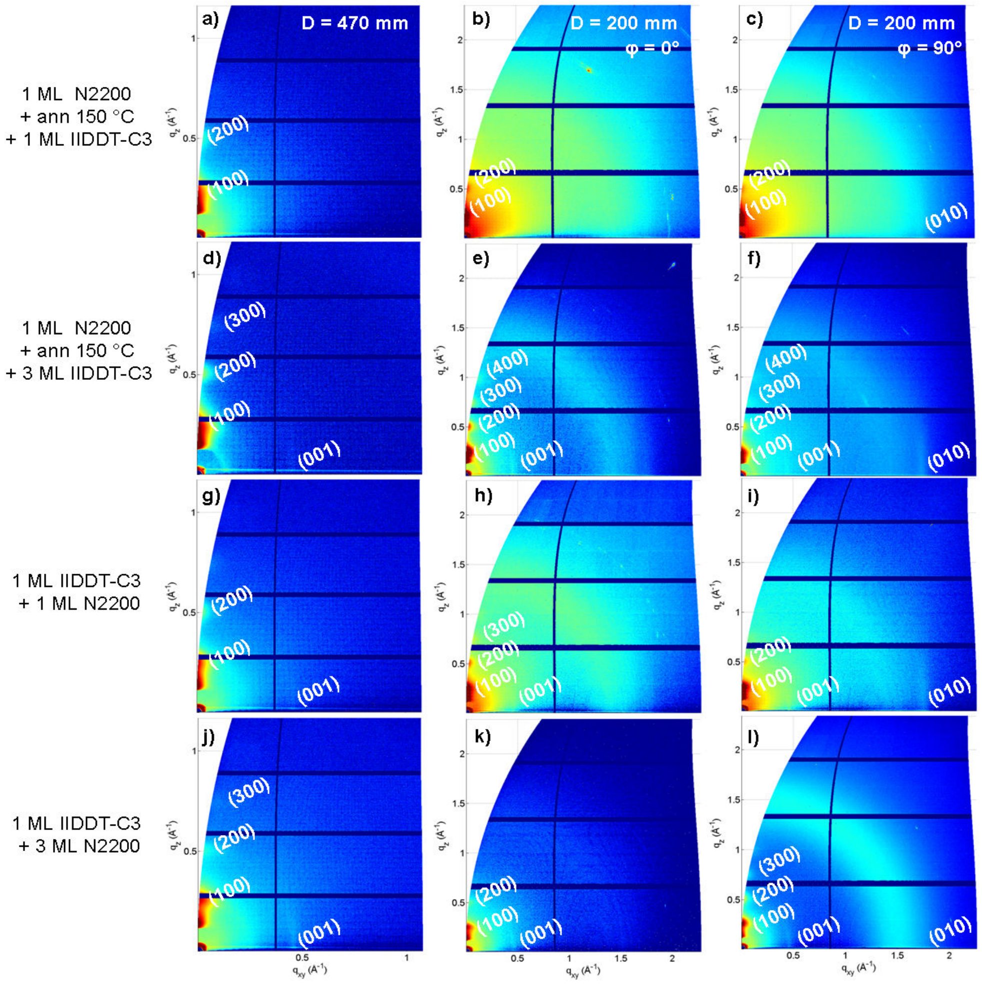

Figure 4.17: 2D-GIXRD images at sample detector distance D = 470 mm and D = 200 mm of four different bilayers: a-c) 1 ML of N2200 annealed at 150 °C overnight in vacuum oven plus 1 ML of IIDDT-C3; d-f) 1 ML of N2200 annealed at 150 °C overnight in vacuum oven plus 3 ML of IIDDT-C3; g-i) 1 ML of IIDDT-C3 plus 1 ML of N2200; j-l) 1 ML of IIDDT-C3 plus 3 ML of N2200. ϕ indicates the reciprocal direction of the incoming X-ray beam and the IIDDT-C3 fibers: for ϕ = 0° they are perpendicular and for ϕ = 90° they are parallel.

All the bilayers presented some common features, as for example the presence of various spots related to the (h00) family of lattice planes in the q_z direction. These reflections are related to the lamella stacking of both polymers, so they imply an edge-on organization of both the polymeric chains with respect to the substrate surface. This description is corroborated by the presence in the q_{xy} direction of the (001) reflection, ascribed to the N2200 chain backbone [18], and the (010) reflection, indicating the π-π stacking between IIDDT-C3 chains which is dependent on the reciprocal orientation between the incoming X-ray beam and the IIDDT-C3 chains (ϕ).

4.3.3.2 Morphology

Figure 4.18 shows the comparison between the topography of two bilayers, specifically those depicted in Figure 4.16a and 4.16c. In the first case The IIDDT-C3 layer was deposited on top of a single as-cast N2200 layer, whereas in the second case the p-type material was deposited on top of a single N2200 layer annealed at 150 °C overnight in vacuum oven.

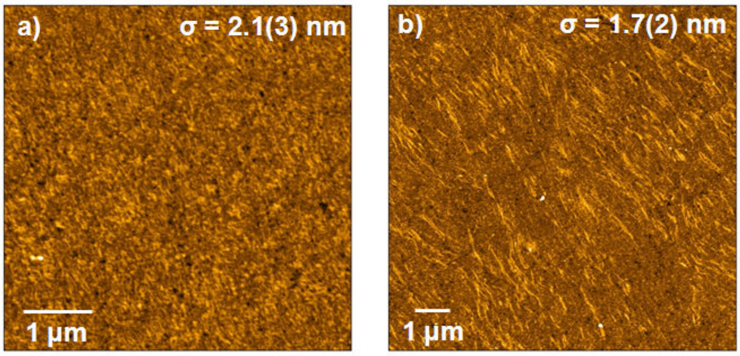

Figure 4.18: AFM images of a) (5x5 μm^2) 1 ML N2200 + 1 ML IIDDT-C3 film and b) (10x10 μm^2) 1ML N2200 annealed at 150 °C + 1 ML IIDDT-C3 film deposited by LS technique.

The thermal treatment of the first deposited layer influences the growth of the topmost layer, which presents a smoother surface (σ_{SURF} decreases from 2.1 to 1.7 nm) and the characteristic polymeric chains of IIDDT-C3.

4.3.3.3 Electrical properties

The influence of the structural and morphological characteristics of the single layers on the electrical properties was investigated by recording output and transfer curves both in linear (V_{SD}: ±10V) and saturation (V_{SD}: ±50V) regimes of the ambipolars. All the devices represented in Figure 4.14 were tested and the results of μ, V_{TH} and I_{ON}/I_{OFF} as functions of devices channel length (L) are reported here below.

N2200 + IIDDT-C3 bilayer ambipolar

The electrical characterization on devices composed by a bottom layer of as-cast N2200 and a top layer of IIDDT-C3 (Figure 4.19) presents V_{TH} values pretty much stable around +60 V and -60 V, μ_{SAT} of the order of 10^{-1} cm^2/Vs for the n-type carriers and 10^{-1} - 10^{-2} cm^2/Vs for the p-type carriers and I_{ON}/I_{OFF} for both p and n-type materials between 10^2 and 10^4. In the linear regime the situation is very similar but both charge carriers mobility remains within 10^{-2} cm^2/Vs.

The increment of the IIDDT-C3 layers on top does not particularly modify the electrical response except for the linear mobility which increases up to the 10^{-1} cm^2/Vs range (Figure 4.20).

With respect to the as-cast N2200 devices (Figure 4.8) the electron mobility is increased of two orders of magnitude and results perfectly balanced to the holes mobility, which is a remarkable result. This large improving might depend on the effect of the p-type layer on top, which tends to fill the morphological holes of the film underneath, thus creating a continuous film able to support both electrons and holes transport. On the other hand, also considerations about the HOMO and LUMO levels of the two materials one on top of the other and respect to the work function of the gold electrodes have to be done. For this purpose, UPS measurements on the bilayers will be carried out in the next future.

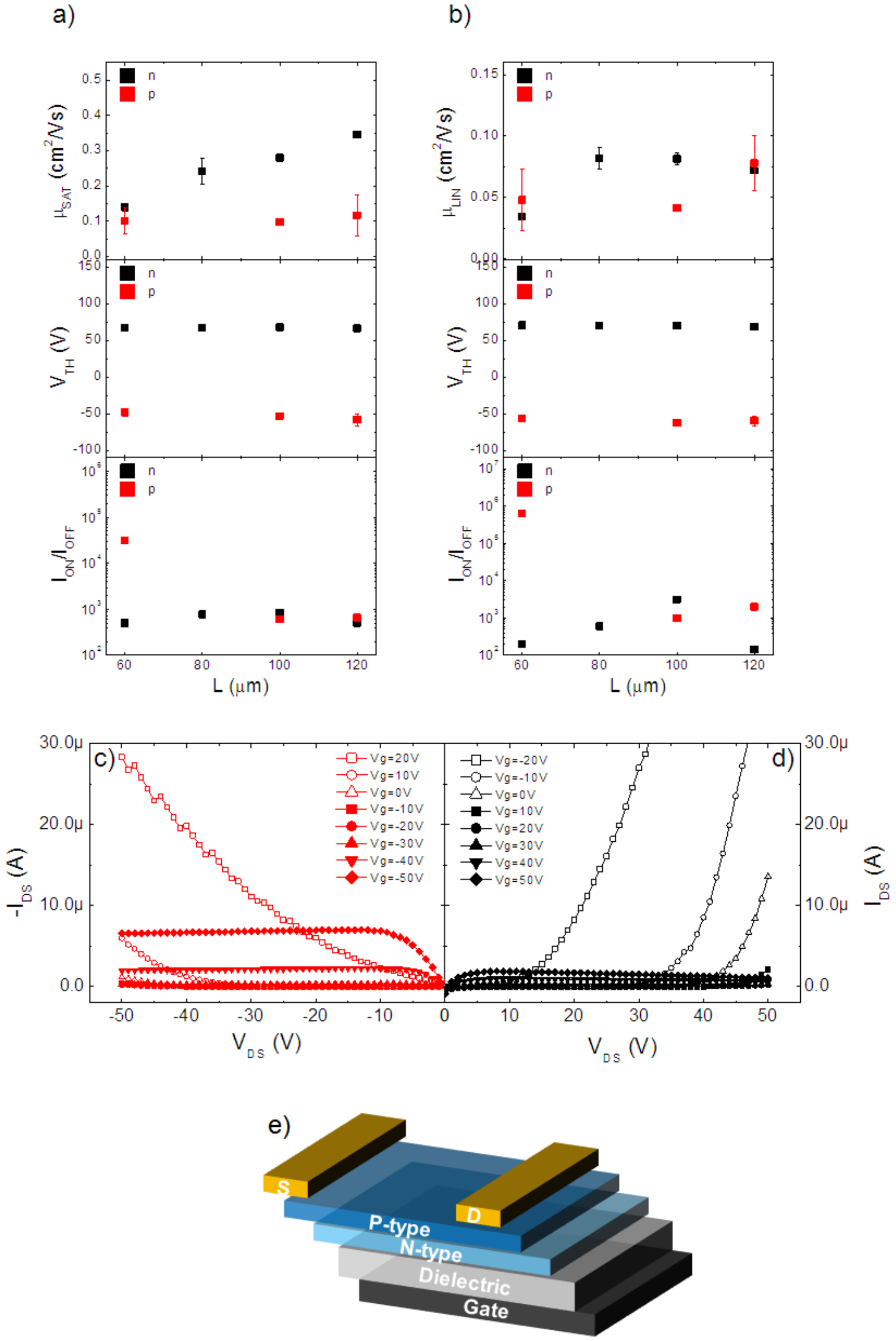

Figure 4.19: Electrical results of device constituted of 1 ML of N2200 + 1 ML of IIDDT-C3 in a) saturation and b) linear regime. Examples of c) p-type and d) n-type output characteristics of a device with L = 80 μm. e) Sketch of the device.

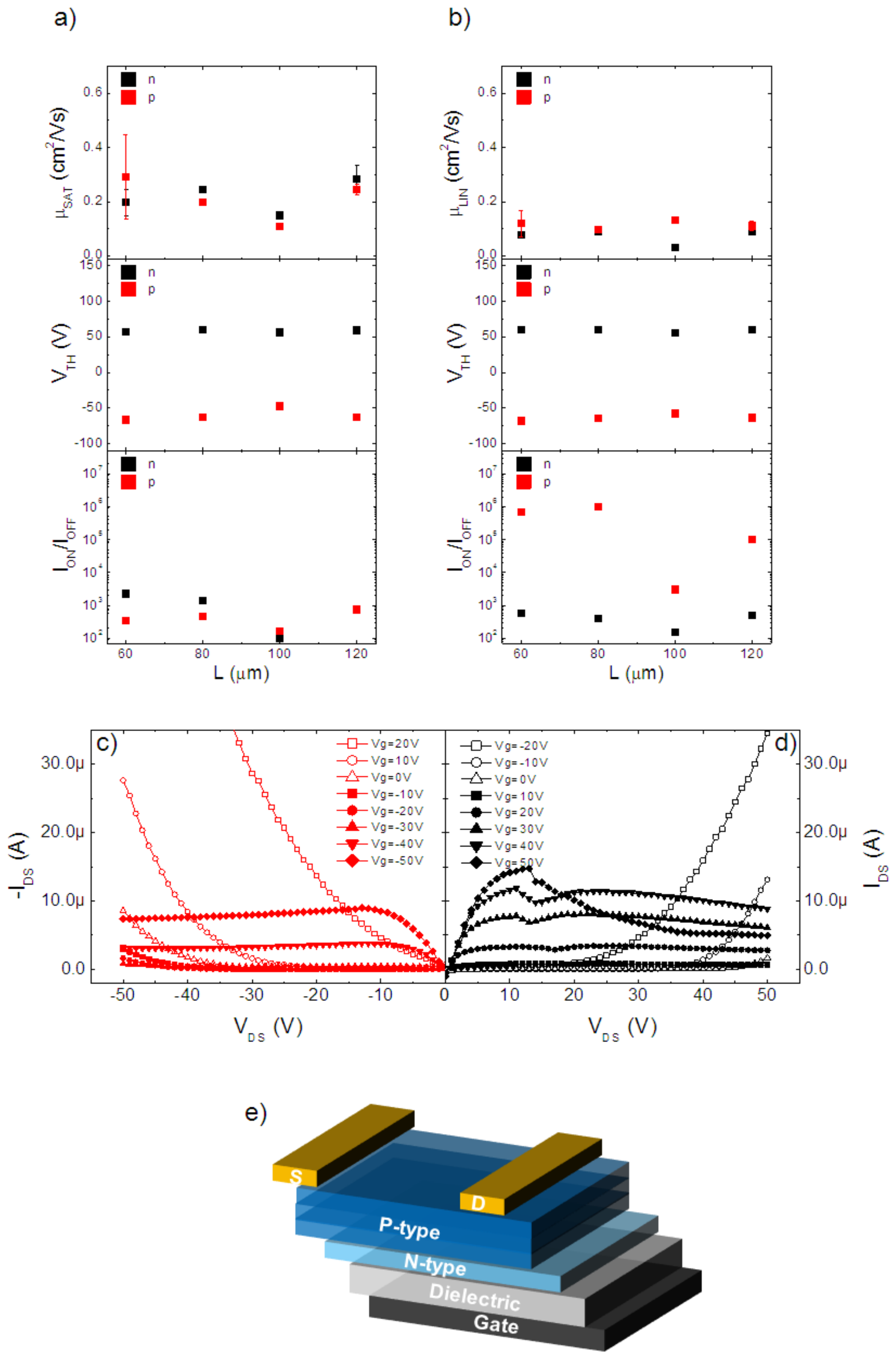

Figure 4.20: Electrical results of device constituted of 1 ML of N2200 + 3 ML of IIDDT-C3 in a) saturation and b) linear regime. Examples of c) p-type and d) n-type output characteristics of a device with L = 80 μm. e) Sketch of the device.

N2200 annealed + IIDDT-C3 bilayer ambipolar

The devices with N2200 annealed as bottom layer and a single IIDDT-C3 as top layer (Figure 4.21) present V_{TH} values stable around +60 V and -50 V, μ_{SAT} of the order of 10^{-1} cm^2/Vs for both types of carrier and I_{ON}/I_{OFF} ranging between 10^2 and 10^4, with the higher values related to the holes. Remarkably, also in the linear regime the mobility reaches 10^{-1} cm^2/Vs.

The increasing of the top IIDDT-C3 layer thickness (4.22) unexpectedly brings to the decreasing of the holes mobility by an order of magnitude (from 10^{-1} to 10^{-2} cm^2/Vs), but leaves the V_{TH} and I_{ON}/I_{OFF} values almost unaltered.

Also in these cases, with respect to the simple N2200 annealed devices (Figure 4.9) the electrons mobility has gained one order of magnitude and results pretty well balanced to the holes mobility. It is difficult to attribute this improvement to the filling-holes effect of the p-type layer on top because in this case (as shown in Figure 4.7) the molecular reorganization caused by the thermal treatment already contributes to fill the uncovered substrate area. In these particular devices UPS measurements are crucial to correctly describe the charge transport mechanism.

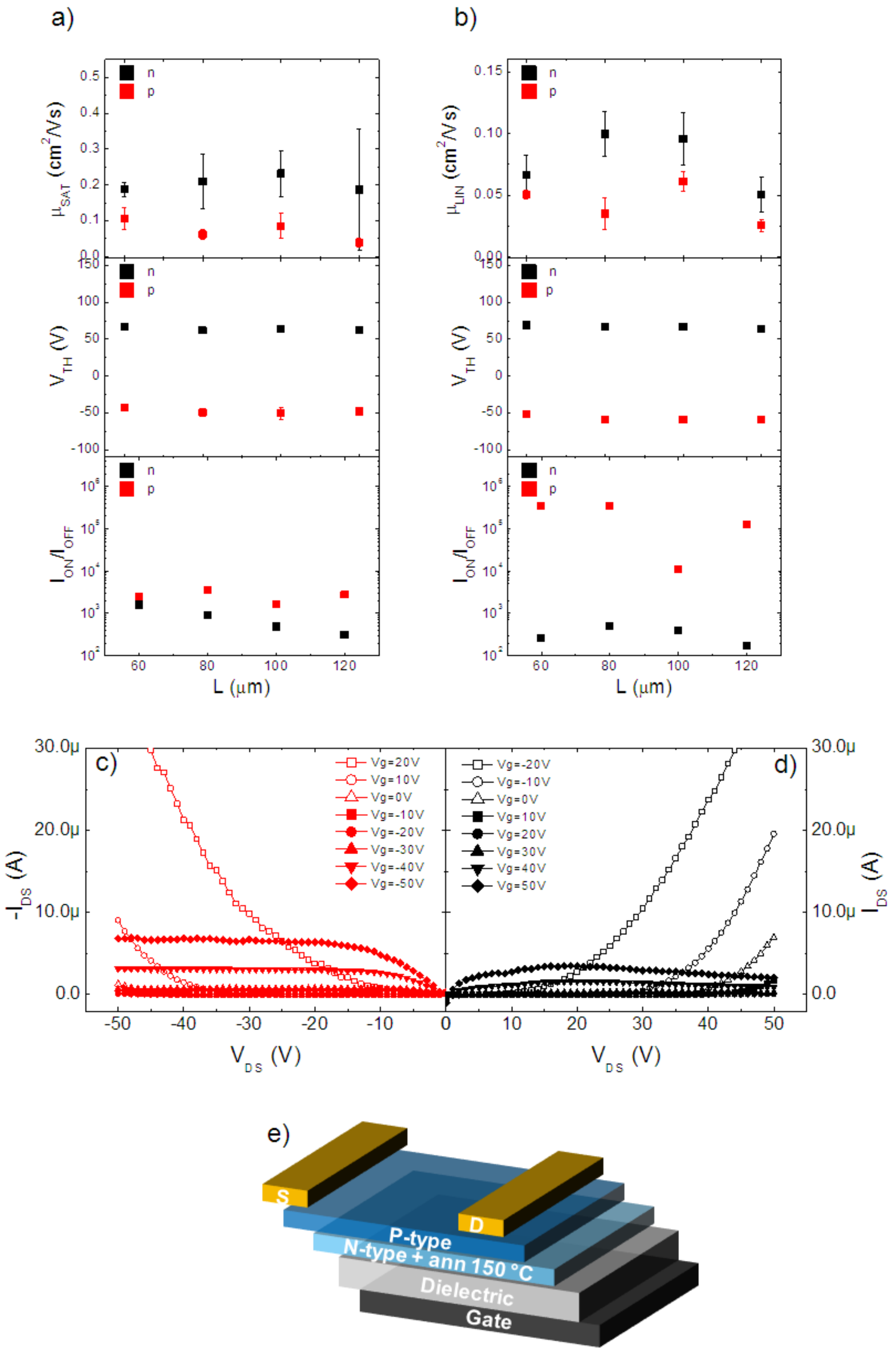

Figure 4.21: Electrical results of device constituted of 1 ML of N2200 annealed at 150 °C overnight in vacuum oven + 1 ML of IIDDT-C3 in a) saturation and b) linear regime. Examples of c) p-type and d) n-type output characteristics of a device with L = 80 μm. e) Sketch of the device.

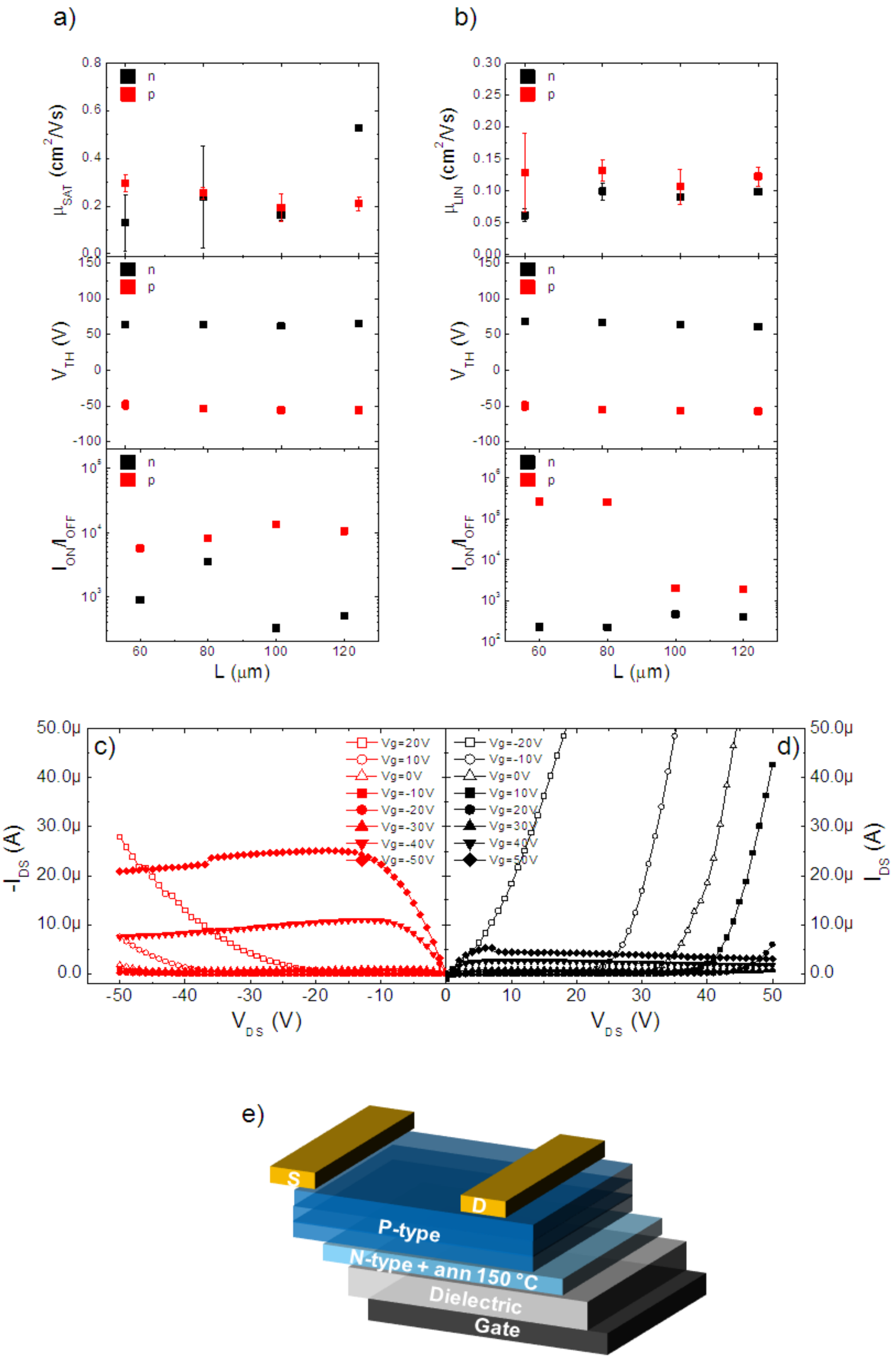

Figure 4.22: Electrical results of device constituted of 1 ML of N2200 annealed at 150 °C overnight in vacuum oven + 3 ML of IIDDT-C3 in a) saturation and b) linear regime. Examples of c) p-type and d) n-type output characteristics of a device with L = 80 μm. e) Sketch of the device.

IIDDT-C3 + N2200

The devices with IIDDT-C3 layer as bottom layer (Figure 4.23) present good p-type electrical characteristics, with stable V_{TH} values, μ_{SAT} ranging from 10^{-1} to $10^{-2} cm^2$/Vs and I_{ON}/I_{OFF} between 10^3 and 10^4, but low n-type mobility (10^{-3} cm^2/Vs) almost comparable with those of the single nominal N2200 layer without any thermal treatment (4.8). Interestingly ,with respect to the precedent bilayer case, in which the order of the n- and p-type layers was inverted, there is not a dramatic change in the V_{TH} values. This could indicate that the ability to form a conductive layer for the two materials does not depend on the layer underneath. Furthermore, the situation does not improve upon increasing of the N2200 thickness on top (Figure 4.24).

The reasons behind this peculiar electrical behavior remain an open issue. Further investigations on the thickness and density of the layers as well as UPS measurements will help figuring out the charge transport mechanism.

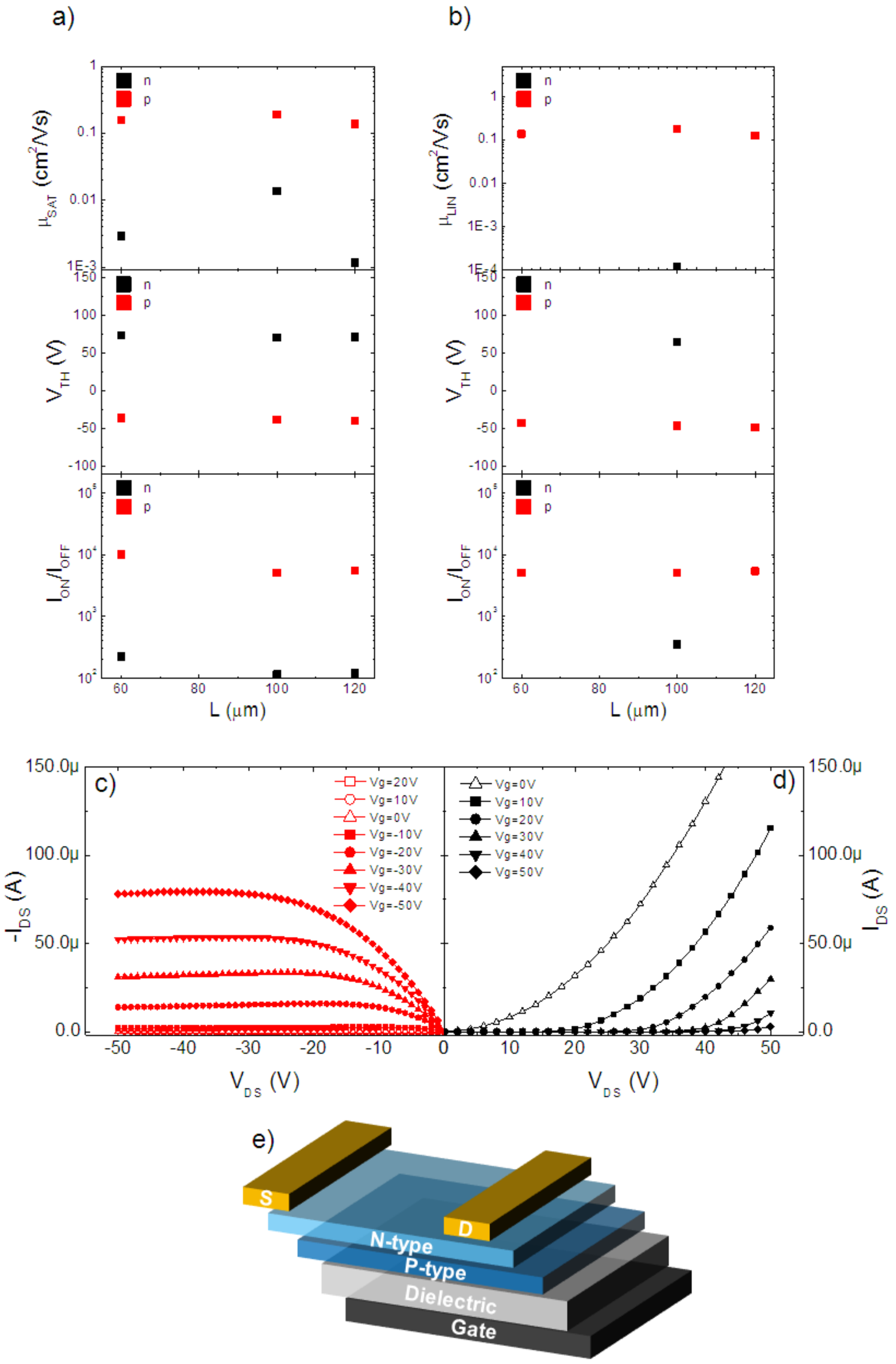

Figure 4.23: Electrical results of device constituted of 1 ML of IIDDT-C3 + 1 ML of N2200 in a) saturation and b) linear regime. Examples of c) p-type and d) n-type output characteristics of a device with L = 100 μm. e) Sketch of the device.

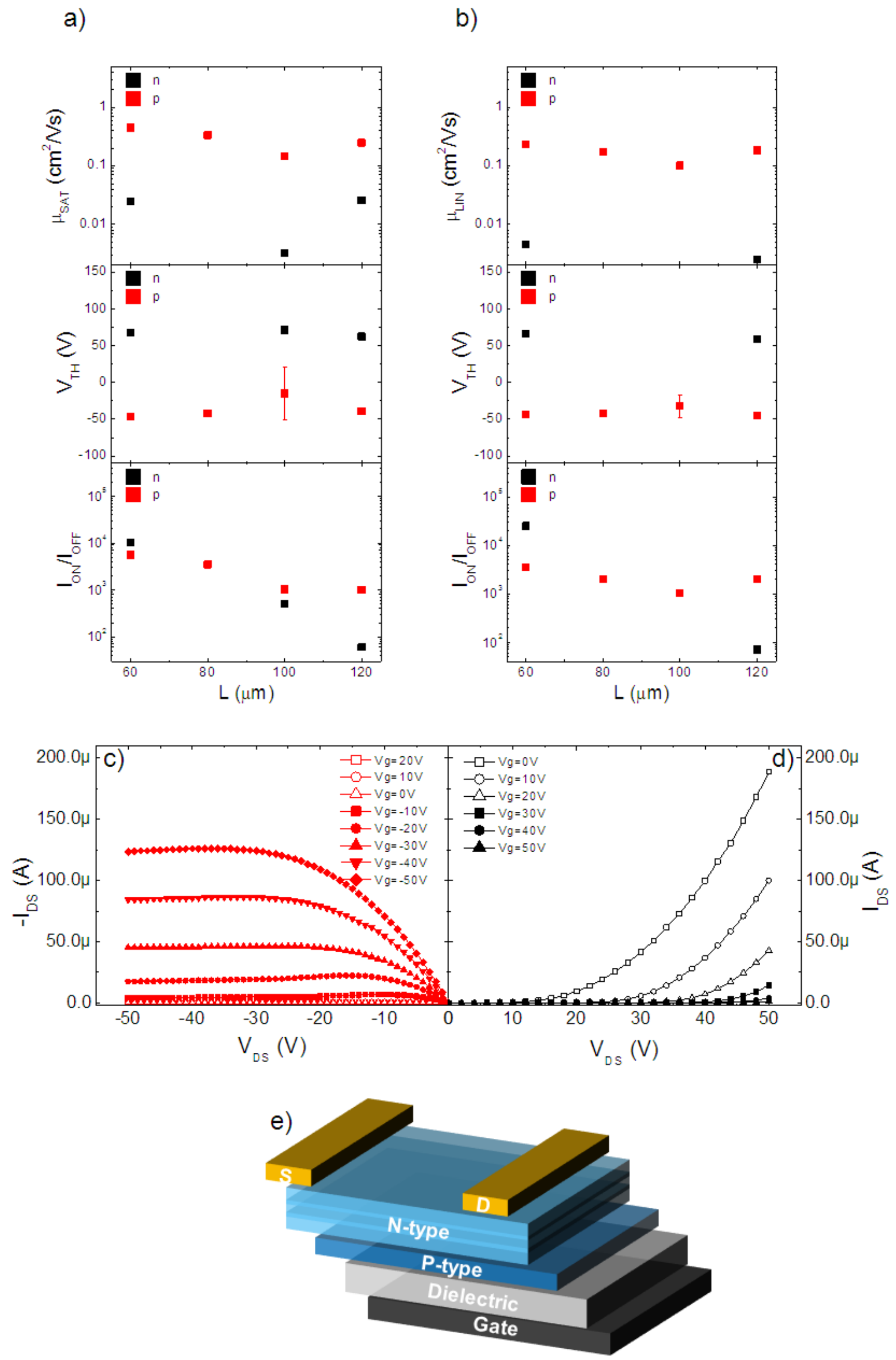

Figure 4.24: Electrical results of device constituted of 1 ML of IIDDT-C3 + 3 ML of N2200 in a) saturation and b) linear regime. Examples of c) p-type and d) n-type output characteristics of a device with L = 80 μm. e) Sketch of the device.

4.4 Conclusions

Polymeric ambipolar bilayers with both active materials deposited from solution have been fabricated and characterized.

From the structural characterization it emerges that the deposition technique employed (Langmuir-Schaefer) coerces the lamella of the two polymers to adopt an edge-on orientation with respect to the substrate surface.

In the case of N2200 a thermal treatment at 150 °C overnight in vacuum oven promotes the reorganization of the polymer on the substrate surface. This reorganization transforms the as-cast film, characterized by an enormous amount of discontinuities and high roughness, into a smoother and continuous film with improved crystallinity and charge carrier mobility due to the increasing number of percolation paths available. A similar result is obtained by increasing the thickness of the N2200 film. Nevertheless, in both cases the V_{TH} remains high (around +60 V) and it even seems to slightly increase after the annealing, indicating that the number of defects is not reduced.

In the IIDDT-C3 case already the as-cast film shows a nice fibrillar packing with a preferential direction for the growth of the fibers induced by the deposition technique. Upon increasing of the film thickness the mobility gains one order of magnitude reaching 10^{-1} cm^2/Vs and the V_{TH} decreases of roughly 10 V, indicating an improvement in the percolation paths as well as a decreasing of the traps for the charge carriers.

The edge-on organization of the lamella for both polymers is maintained in the bilayer architectures and contributes to the correct and balanced electrical behavior of the devices. Several architectures depending on the relative position of the n- and p-type materials were studied. In all the cases where the nominal single N2200 layer was in contact with the substrate, the electron mobility in saturation regime reached 10^{-1} cm^2/Vs independently from the thickness of the IIDDT-C3 layer on top. This result is remarkable, especially if we think that previous measurement of single N2200 layers as-cast and after thermal treatment gave maximum mobility values of 10^{-3} cm^2/Vs and 10^{-2} cm^2/Vs respectively. On the other hand, the situation is reversed when the N2200 layer (independently of the thickness) is deposited on top of an IIDDT-C3 layer. In this last case in fact the electron mobility decreases down to 10^{-3} cm^2/Vs. To relate this boosting or dropping of the electron mobility with an apparent invariant V_{TH} is still an open issue. Further measurements will be performed in the near future to obtain a general comprehension of the charge transport mechanism taking place in these bilayer ambipolars. Ultraviolet photoemission spectroscopy (UPS) measurements will be done to establish the alignment or misalignment of the bilayers energetic levels and a complete fit of the XRR data of the most homogeneous and smooth samples (both single and multiple layers) will be tried to obtain more substantial values of thickness as well as roughness and density.

4.5 Bibliography

[1] R. Capelli, F. Dinelli, M. A. Loi, M. Murgia and M. Muccini. *Organic Light Emitting Materials and Devices X* **6333**, T3330–T3330 (2006)

[2] R. Capelli, F. Dinelli, M. A. Loi, M. Murgia, R. Zamboni and M. Muccini. *Journal of Physics-Condensed Matter* **18(33)**, S–2127–S2138 (2006)

[3] C. Rost, S. Karg, W. Riess, M. A. Loi, M. Murgia and M. Muccini. *Applied Physics Letters* **85(9)**, 1613–1615 (2004)

[4] G. Dell'Erba, A. Luzio, D. Natali, J. Kim, D. Khim, D. Y. Kim, Y. Y. Noh and M. Caironi. *Applied Physics Letters* **104(15)** (2014)

[5] S. Cho, S. H. Nho, M. Eo and M. H. Lee. *Organic Electronics* **15(5)**, 1002–1011 (2014)

[6] C. Lu, J. Wang, H. C. Chang, Y. C. Chiu, H. Y. Chen, H. C. Wu, T. Higashihara and W. C. Chen. *Journal of Materials Chemistry C* **2(36)**, 7489–7493 (2014)

[7] F. Dinelli, M. Murgia, P. Levy, M. Cavallini, F. Biscarini and D. M. de Leeuw. *Physical Review Letters* **92(11)**, 116802 (2004)

[8] A. Dodabalapur, H. E. Katz, L. Torsi and R. C. Haddon. *Science* **269(5230)**, 1560–1562 (1995)

[9] A. Dodabalapur, H. E. Katz, L. Torsi and R. C. Haddon. *Applied Physics Letters* **68(8)**, 1108–1110 (1996)

[10] A. Dodabalapur, J. Laquindanum, H. E. Katz and Z. Bao. *Applied Physics Letters* **69(27)**, 4227–4229 (1996)

[11] P. Cosseddu, A. Bonfiglio, I. Salzmann, J. P. Rabe and N. Koch. *Organic Electronics* **9(2)**, 191–197 (2008)

[12] C. Rost, D. J. Gundlach, S. Karg and W. Riess. *Journal of Applied Physics* **95(10)**, 5782–5787 (2004)

[13] R. Steyrleuthner, R. Di Pietro, B. A. Collins, F. Polzer, S. Himmelberger, M. Schubert, Z. H. Chen, S. M. Zhang, A. Salleo, H. Ade, A. Facchetti and D. Neher. *Journal of the American Chemical Society* **136(11)**, 4245–4256 (2014)

[14] M. El Gemayel, S. Haar, F. Liscio, A. Schlierf, G. Melinte, S. Milita, O. Ersen, A. Ciesielski, V. Palermo and P. Samori. *Advanced Materials* **26(28)**, 4814–+ (2014)

[15] R. Steyrleuthner, M. Schubert, I. Howard, B. Klaumunzer, K. Schilling, Z. H. Chen, P. Saalfrank, F. Laquai, A. Facchetti and D. Neher. *Journal of the American Chemical Society* **134(44)**, 18303–18317 (2012)

[16] A. Luzio, L. Criante, V. D'Innocenzo and M. Caironi. *Scientific Reports* **3** (2013)

[17] J. Rivnay, R. Steyrleuthner, L. H. Jimison, A. Casadei, Z. H. Chen, M. F. Toney, A. Facchetti, D. Neher and A. Salleo. *Macromolecules* **44(13)**, 5246–5255 (2011)

[18] H. Yan, Z. H. Chen, Y. Zheng, C. Newman, J. R. Quinn, F. Dotz, M. Kastler and A. Facchetti. *Nature* **457(7230)**, 679–U1 (2009)

[19] S. Fabiano, C. Musumeci, Z. H. Chen, A. Scandurra, H. Wang, Y. L. Loo, A. Facchetti and B. Pignataro. *Advanced Materials* **24(7)**, 951–+ (2012)

[20] R. Stalder, J. G. Mei, K. R. Graham, L. A. Estrada and J. R. Reynolds. *Chemistry of Materials* **26(1)**, 664–678 (2014)

[21] T. Lei, J. H. Dou and J. Pei. *Advanced Materials* **24(48)**, 6457–6461 (2012)

[22] T. Lei, J. Y. Wang and J. Pei. *Accounts of Chemical Research* **47(4)**, 1117–1126 (2014)

[23] J. Rivnay, M. F. Toney, Y. Zheng, I. V. Kauvar, Z. H. Chen, V. Wagner, A. Facchetti and A. Salleo. *Advanced Materials* **22(39)**, 4359–+ (2010)

CHAPTER 5

IN-SITU AND REAL-TIME STUDY ON PENTACENE OFETS

In this chapter it is presented the study on the structural evolution of pentacene thin-film during the OFET operation.

5.1 Introduction

Even though the cause-effect relationship between microstructure of organic semiconductors and devices performance is widely taken in consideration (see Chapter 1 section 1.4), very little is known about the reverse, that is the impact of the electric field produced by the device operation on the organic semiconductor film structure. In literature there is only a single reported investigation performed by Raman spectroscopy, an indirect structural technique, showing a structural modification in pentacene films induced by the electrical field during device operation [1]. In this chapter it will be presented for the first time a direct measurement of the structural evolution of pentacene thin-films observed during the application of a gate and source-drain bias to the OFET.

5.2 Experimental

5.2.1 Active materials

Due to the intrinsic difficulty of the experiment, pentacene, the most investigated p-type small molecule (see Chapter 1 section 1.1), was the most obvious choice for this study. Moreover, as just mentioned, some preliminary results were already obtained by Raman investigation on this type material.

5.2.2 Device fabrication

Pentacene films were grown by ultra-high vacuum sublimation at a rate of 0.5 ML/min on SiO_2 (200nm)/Si surface at room temperature. Gold electrodes (40 nm) were evaporated later on the top of the organic material. The device architecture presents a channel length (L) of 300 μm and channel width (W) 10 mm, in order to have an aspect ratio (W/L = 34) sufficient to guarantee correct transistor operation and the X-ray beam probing inside the channel (Figure 5.1).

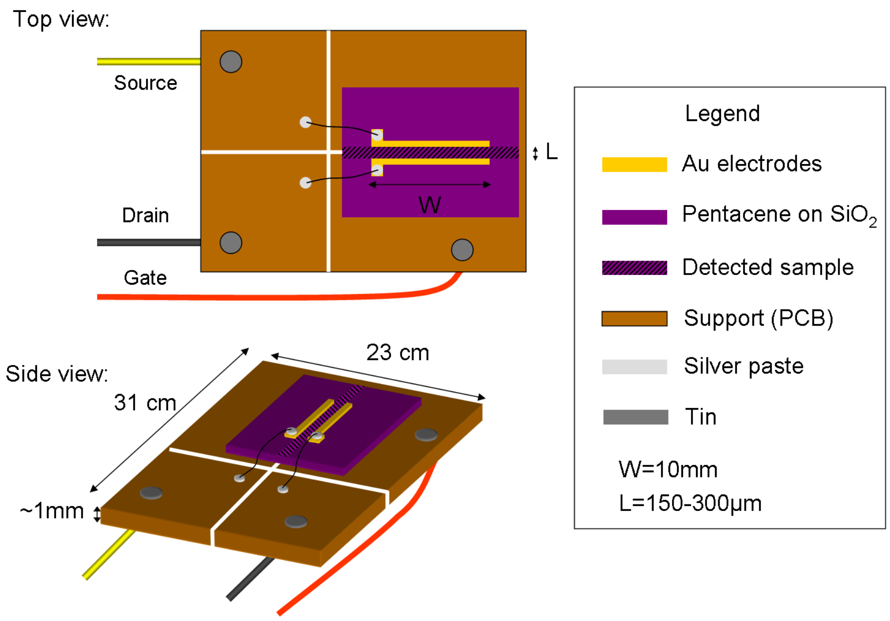

Figure 5.1: Schematic view of a pentacene OFET exploited for in-situ and real-time structural nvestigation.

5.2.3 Characterization methods

5.2.3.1 Structural characterization

X-Ray Diffraction (XRD) measurements, both in specular and Grazing Incidence (GIXRD) geometries, were performed inside the transistor channel during the application of drain-source (V_{SD}) and gate (V_{SG}) voltages (i.e. in-situ and real-time). The reciprocal space map (RSM) of (001) pentacene reflection was performed using a SmartLab-Rigaku diffractometer equipped with a rotating anode (Cu Kα, λ = 1.54056 $\AA$). The out-of-plane and in-plane characterization was performed at two synchrotron facilities: ELETTRA (Italy) and ESRF (France). At MCX-ELETTRA beamline, the beam had a wavelength of 1.0332 $\AA$ and size 200 x 300 μm^2; diffraction peaks were measured by a point detector and the angular acceptance defined by secondary slits before detector was 0.023° for the low ($\theta/2\theta$) and 0.005° for the high resolution (RC) measurements. Further $\theta/2\theta$ scans and rocking curves were collected by a 2D detector at ID01-ESRF beamline with a monochromatic beam of λ = 1 $\AA$. The beam size was 1.8 x 3.0 μm^2 and the images were collected at different position into the channel in order to reduce radiation damage. All diffraction intensities were normalized to the incident beam intensity.

5.2.3.2 Morphological characterization

Topographical AFM characterization was carried out in intermittent contact mode in air environment making use of a Smena, NT-MDT (Moscow, Russia). Data analysis was performed using Gwyddion software.

5.2.3.3 Electrical characterization

Transfer curves were collected with a Keithely parameter analyzer before and after the application of constant V_{SG} and V_{SD} in order to not perturb the system, as well as before, during and after X-rays irradiation of the sample to detect possible damages related to the synchrotron radiation. V_{TH} and μ were extrapolated from the transfer curves in saturation regime following the eq. 1.21.

5.3 Results and discussion

The schematic of a typical experiment is depicted in Figure 5.2. One specific pentacene reflection is probed by the X-ray beam passing through the OFET channel constituted by a few-layers (5-10 layers) of vacuum deposited pentacene.

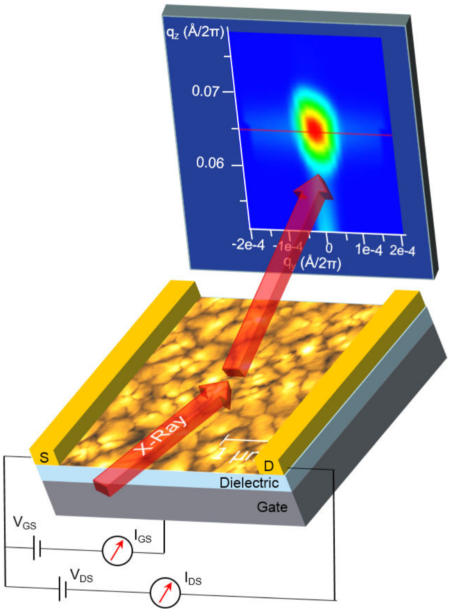

Figure 5.2: Schematics of the in-situ and real-time measurements on pentacene OFET. AFM image and RSM around the (001) reflection of 10MLs thick pentacene film.

In Figure 5.2, also the Reciprocal Space Map (RSM) collected around the (001) reflection and AFM image of a pristine 10 MLs pentacene film are reported. They indicate that the film is formed by very high textured crystals (as deduced from the very narrow Bragg peak) having thin-film phase (as calculated from the peak position, i.e. d_{001} = 1 ML = 15.5 $\mathring{A}$), and it is characterized by big 3D islands (height and size) and a rough surface (σ_{RMS} = 1.7 nm). Before starting with the in-situ and real-time experiments, preventive measurements concerning the time exposure of the OFET to the highly collimated X-ray synchrotron beam were carried out.

5.3.1 Effect of X-ray beam on OFET response

The influence of the x-ray beam on the OFET response was investigated by carrying out a series of transfer curves before, during and after the x-ray exposure, with $V_{SD} = -30V$. All curves are reported in Figure 5.3 and show a shift versus more negative V_{GS} when the film is not perturbed by x-ray beam. On the contrary, during x-ray exposure transfer curves recover their initial state and shifts again towards more negative V_{SG} after the beam is switched off.

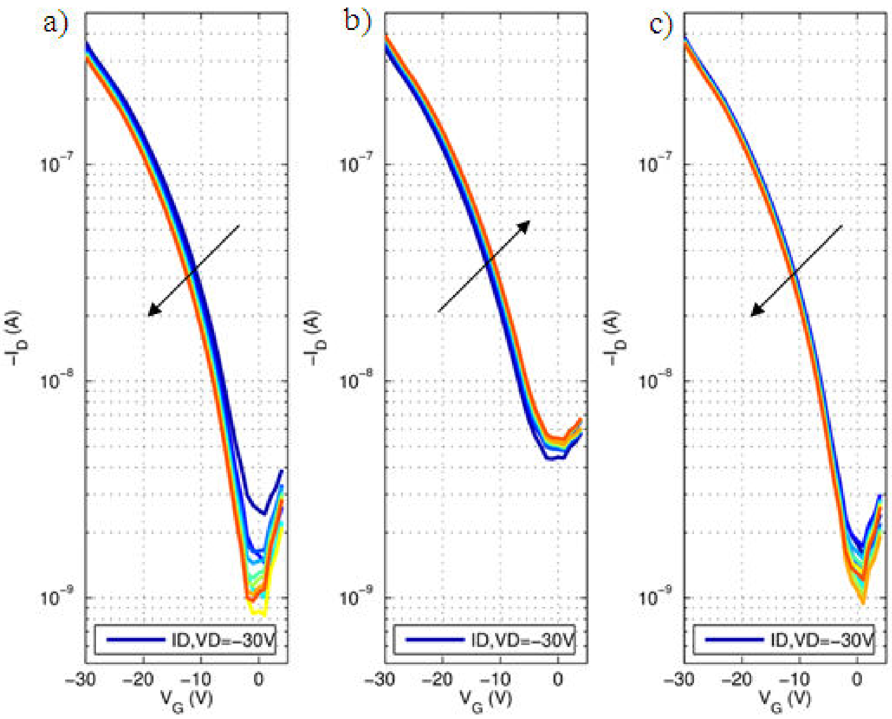

Figure 5.3: Transfer curves acquired a) before, b) during and c) after X-ray exposure. Arrows indicate V_{TH} shift.

Figure 5.8 shows the V_{TH} values extracted from the transfer curves in saturation regime (V_{SD} = 30 V) and plotted versus time. V_{TH} shift towards more negative values is primarily due to the trapping of charge carriers in the traps located at the semiconductor/dielectric interface or in the bulk dielectric. The mobility values extracted from these transfers (Figure 5.8b) show a smaller variation during the applied bias compared to the variation of the V_{TH}. The trapped charges partially screen the applied electric field so that the effective applied V_{SG} is smaller when trapped charges are present. This phenomenon is usually called bias stress and has an important influence on the stability during device operation.

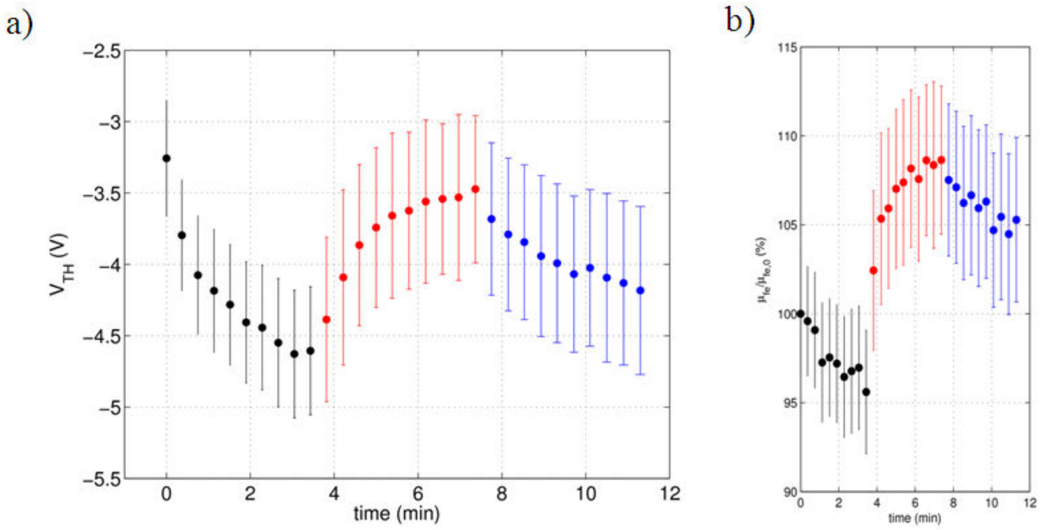

Figure 5.4: a) V_{TH} and b) μ values *vs* time. Color legend: black before, red during, blue after X-ray exposure.

When the OFET is exposed to x-ray beam, V_{TH} shifts back to the positive direction, suggesting a recovery of the transistor. The origin of this behaviour can be ascribed to several phenomena. High energetic synchrotron photons cause atoms ionization and excitation. In the ionization process an electron-loss centre is formed together with a secondary electron of several keV of energy, typically ejected from an inner electron shell of an atom of the absorbing material. The secondary electron will induce further ionization events within the atoms of the material, resulting in the formation of a cascade of electrons, many of which can then ionize other atoms. The generated photoelectrons may perturb the OFET response and, therefore, the extraction of its characteristics, other than induce radiation damage to the organic film [2–4]. Among the excitation processes occurring in the semiconductor film, electrons may move from HOMO to LUMO, producing vacancies (i.e. holes) in the HOMO, or may recombine with holes in the trap states. These transitions may be the main cause of the V_{TH} recovery. On the other hand, photons also penetrate into the dielectric material and interact with it. A migration of the generated photoelectrons to the dielectric surface will take place due to the V_{SG} application, leading to an increasing of the capacitance and, therefore, of the I_{SD}.

5.3.2 X-ray damage study

Due to the high beam intensity and collimation, X-ray radiation of third generation synchrotron can induce radiation damage. One possible mechanism for radiation damage derives from the X-ray beam induced production of photoelectrons in the investigated materials. As just mentioned, the large beam radiation intensity creates a huge amount of photoelectrons in the organic material and in the substrate. As a consequence, reactive artefacts are formed in the organic materials which can cause damage in the molecular structure [2, 3]. Diffraction measurements have shown that pentacene structure is highly stable during the irradiation in the range up to 1022 photons$/cm^2$ due to its high crystallinity [4]. A sequence of $\theta/2\theta$ scans around the (001) Bragg reflection were performed to check the stability of the pentacene structure under long X-ray exposure ($6 \cdot 10^{12}$ photons$/s \cdot cm^2$ at ELETTRA-MCX beamline). As shown in Figure 5.5, the Bragg peak does not change during 30 minutes of constant irradiation.

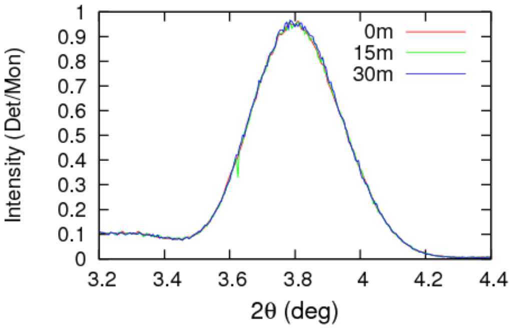

Figure 5.5: $\theta/2\theta$ scans performed at the same position of the film during prolonged X-ray exposure.

Diffraction measurements in Grazing Incidence geometry (GIXRD) were performed at ESRF-ID01 beamline characterized by an X-ray beam intensity 10 order of magnitude higher compared with the previous beamline. In this geometry the beam hints a large area of the sample due to the grazing angle of incidence leading to a broadening of the Bragg peak. In order to reduce the beam footprint and to improve the peak resolution a micro beam size was adopted. Figure 5.6 shows the 2D-GIXRD images collected around the 1 ± 1 reflection at the same sample position. The large amount of high energy photons destroys the crystal structure, leading to the Bragg peak disappearance. To reduce radiation damage 2D-GIXRD measurements were carried out at different positions inside the conductive channel.

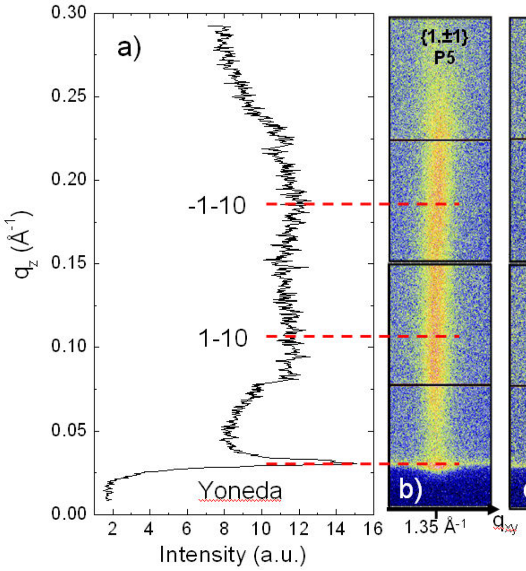

Figure 5.6: a) Scattered intensity integrated along 1 ± 1 rod. b-d) 2D-GIXD images collected in succession at the same channel position around the 1 ± 1 rod.

5.3.3 Effect of the electric field on the out-of-plane diffraction peaks

The stacking layer periodicity was investigated by carrying out specular XRD ($\theta/2\theta$ in Figure 5.7a) and RC (Figure 5.7b) scans at the (001) reflection every 40 minutes, when $V_{SD} = V_{GS} = -20V$ were applied and I_{SD} and I_{SG} were recorded (Figure 5.7c). During operations, the Bragg peak intensity decreases, while the RC curve shifts towards smaller angles without losing intensity. The characteristic decrease of $\mid I_{SD} \mid$ ascribed to bias stress is interrupted by an increase of $\mid I_{SD} \mid$ every time an XRD scan was performed (inset in Figure 5.7c), due to the photocurrent generated by X-ray irradiation.

Figure 5.8 shows the integrated intensities of (001) Bragg peak, the RC peak position, V_{TH} and μ plotted versus time under a variety of conditions. In the presence of $V_{GS} = V_{DS} = -20V$ or $V_{GS} = V_{DS} = -30V$, the Bragg peak intensity decreases and the RC peak shifts toward lower angles. Concomitantly, also V_{TH} decreases together with the mobility. After six hours at $V_{GS} = V_{DS} = -20V$, the integrated intensity has decreased by 34%, the RC peak has shifted by $\Delta\omega = 0.002°$, V_{TH} has shifted from 0 V to -1.7 V and μ has dropped to 20% of the initial value. All but one variation (regarding μ) are reversible, i.e. they are visible when a gate bias is applied ($V_{GS} = V_{DS} = -30V$) and they go back when the biases are switched off to eventually re-appear when biases are re-applied.

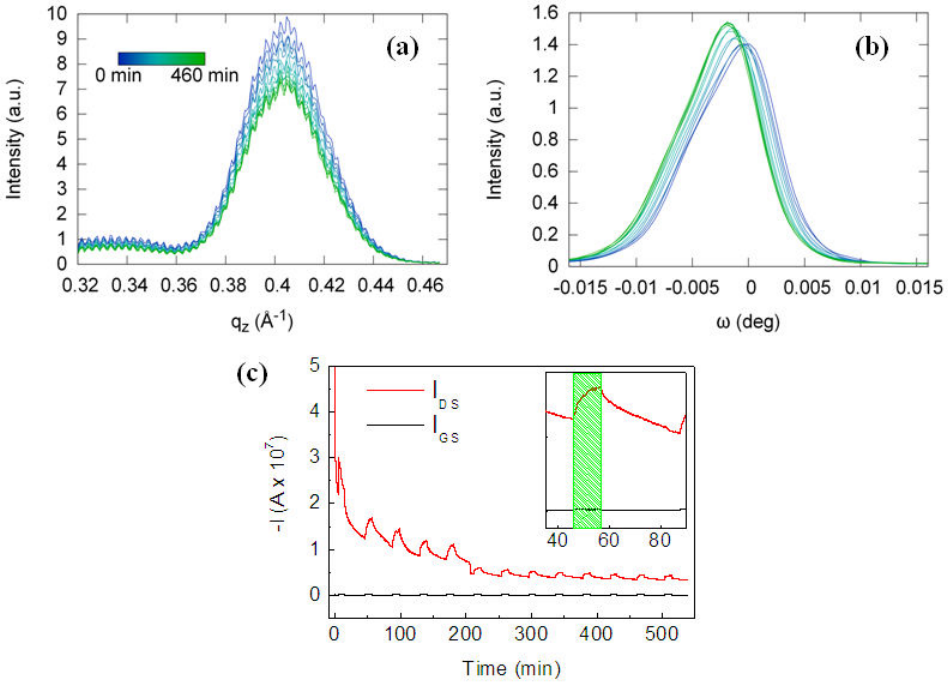

Figure 5.7: $V_{GS} = V_{DS} = -20V$: a) $\theta/2\theta$, b) RC scans collected at XRD1-ELETTRA beamline, and c) I_{DS} and I_{GS} *vs* time. The green box in the inset indicates the time when the XRD scans are performed.

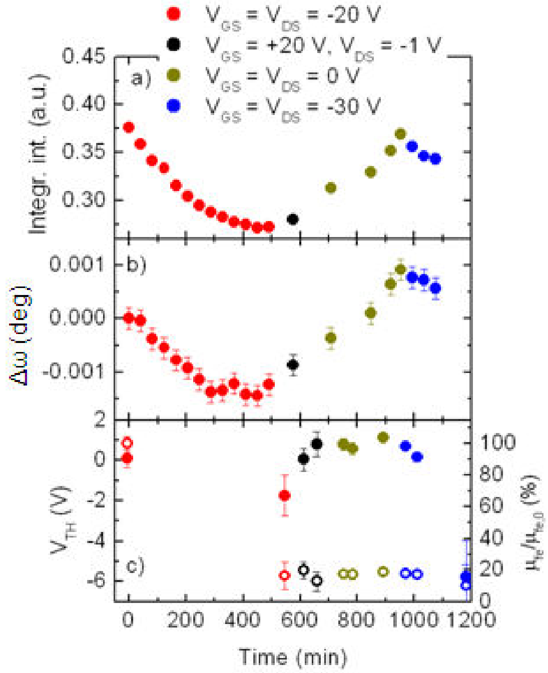

Figure 5.8: a) Integrated intensity of the (001) peak extracted from $\theta/2\theta$ scans, b) Peak shift of the (001) RC and c) V_{TH} (full circles), μ (empty circles) values extracted from transfer curve *vs* time. Absolute errors are calculated with 95% of confidence.

Further $\theta/2\theta$ and RC scans were collected at ID01-ESRF beamline using a 2D detector. By collecting 2D images when incident and detector angles were at the Bragg position, it was possible to measure a partial zone of the RSM around the (001) peak during bias application. The 2D images analysis (Figure 5.9) reveals the Bragg peak shift along the specular direction during the bias stress, which confirms the small lattice expansion previously supposed.

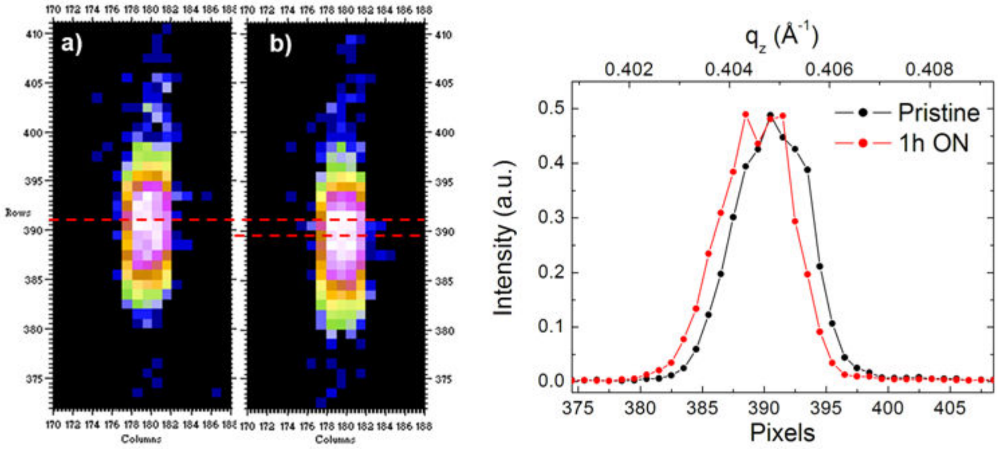

Figure 5.9: 2D detector images collected at the Bragg condition of the pristine film before a) and after b) 1h of $V_{SG} = V_{SD} = -30V$. c) Comparison between vertical slice of the images along the specular direction.

The RC shift towards smaller angles without intensity decrease could be related to a lattice expansion of 0.016 $\mathring{A}$ along the film thickness (i.e. molecular layer thickness), ascribed to a molecular tilt of 2.3 mrad. This is not matched by an analogous observation in the specular scan because of the low angular resolution arising from the Bragg peak broadness (FWHM = 0.3°). The Bragg peak intensity decrease is a consequence of the RC shift. Another relevant phenomenon observed during OFET operation occurs when leakage current appears (Figure 5.10). Indeed, the leakage current (I_{SG}) shields the electric field induced by the gate bias causing a shift back of the RC peak like when transistor is switched off. This behavior highlights the relationship between the vertical electric field effect and the pentacene structural stress.

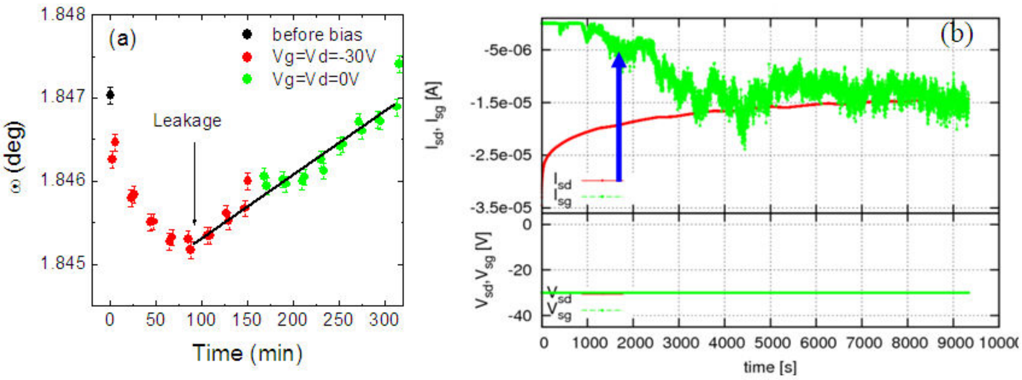

Figure 5.10: a) RC (001) peak position *vs* time; b) I_{SD} and I_{SG} *vs* time whith $V_{SG} = V_{SD} = -30V$ applied. The blue arrow indicates when leakage starts to be relevant.

5.3.4 Effect of the electric field on the in-plane diffraction peaks

The in-plane structure was characterized by collecting 2D-GIXD images around $\{11\}$ rod, corresponding to the strongest in-plane reflection, when $V_{SG} = V_{SD} = -40V$ were applied. In Figure 5.11a the 2D-GIXD image collected before applying any bias is reported. It shows the elongated Bragg signal coming from (1-10) and (-1-10) reflections enhanced at Yoneda position [5] (i.e. when the exit angle of the scattered beam is close to the critical angle, 0.17°for λ = 1 $\AA$) due to the Vineyard effect [6]. After 120 minutes of OFET functioning, the intensity increases regardless the q_z values, as observed in the scattered intensity integrated along the rod plotted in Figure 5.11b. Moreover, the evolution of the scattered intensity integrated along the Yoneda (Figure 5.11c) does not show any significant shift, indicating that the in-plane lattice remains constant as well as the lateral domain coherence. This latter is equal to 58 nm, as evaluated from the peak width along q_{xy} direction, using the Scherrer formula [7] and taking into account the beam footprint as described in ref [8]. This in-plane peak evolution can be explained as an improving of the crystalline order during OFET operation.

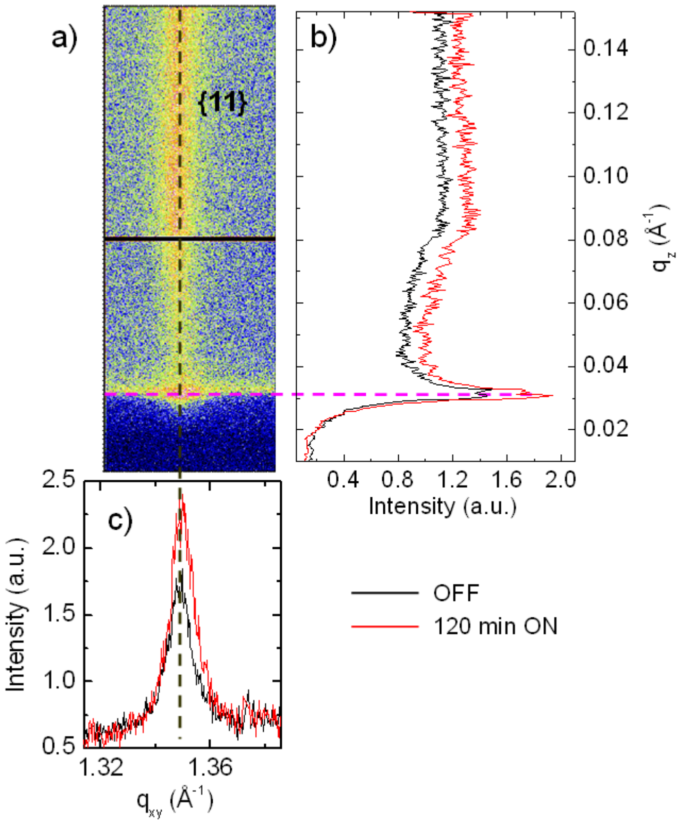

Figure 5.11: a) 2D-GIXD image collected on pristine 6M Ls pentacene film. Scattered intensity integrated along b) the rod at $q_{xy} \sim 1.35 \AA^{-1}$ and c) the Yoneda at $q_z \sim 0.3 \AA^{-1}$ for the images collected before (black line) and after 120 minutes (red line) of bias application.

5.3.5 Computational studies

To corroborate the experimental findings, Professor Zerbetto and co-workers (Chemistry department of the University of Bologna) performed computational studies on two different systems. The first one concerned four pentacene molecules in the vacuum forming a tetramer, that is the case of molecules without periodicity constrains. DFT calculations have shown that in the absence of electrical field tetramer stabilizes in a structure (named A in Figure 5.12a) more compact and at lower energy than the thin-film phase structure [9, 10] (structure B in Figure 5.12b).

In the presence of an electric field along the long axis (simulating the gate field), structure A tends to structure B and both of them become equienergetic. In the second systems, pentacene molecules were constrained in the periodic structure of the thin film phase [9] and deposited on SiO_2 surface. In this case the vertical electrical field slightly affects the crystal structure. By applying a field of 1 V/nm, molecules tilt only 2 mrad towards the direction normal to the surface, according to the experimental results. In the simulation

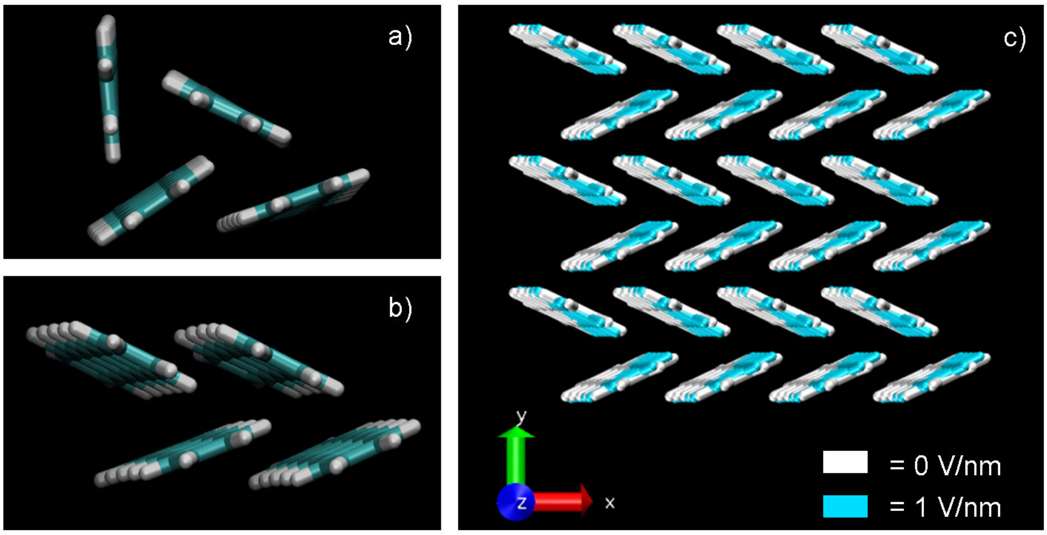

Figure 5.12: Representation of structure A a) and structure B b) of a tetramer in vacuum and c) in the thin film phase.

the applied field is higher than the real one and the strain effect response is almost immediate respect to the several hours needed for observing the Bragg peak shift. These discrepancies can be explained as follows. The simulations were limited to 1 ML thick film. Instead, XRD measurements probe the full film depth (6 or 10 MLs), where molecules are constrained by the upper neighbor potentials which reduce their degree of freedom. Moreover, each layer screens the upper ones from the transversal electric field, reducing the field effect until the fourth ML, as deduced from the effective Debye length calculated on films grown in the same condition [11]. The tetramer field-induced reorganization can be associated to ″situations″ where the number of neighbors is lower than in the crystal, for instance, at the grain boundaries. The presence of a field may modify these structures toward the crystalline one, explaining the increasing of the in-plane peak intensity as a structural ordering. Due to the small amount of molecules forming the grain boundaries, the crystal domain size remains more or less unaffected by the molecular reorganization justifying why the in-plane Bragg peak width is unchanged, regardless the OFET operation. The change of packing motif at the grain boundaries may perturb the charge hopping between crystal grains [12]: molecules re-organize towards the molecular packing of the closer crystalline grain, and a spatial gap may be formed between two crystalline grains creating, therefore, charge traps [13]. This phenomenon may be related with the V_{TH} variation, i.e. the bias stress, introducing a new scenario to the comprehension on charge transport where OFET operation do not only depend on the microstructure of the semiconductor film but also on how the microstructure responds to the applied field and modulates the carrier transport during time.

5.4 Conclusions

Real time XRD measurements performed on few MLs pentance films grown on FET device have revealed structural modification induced by the OFET operation. The experimental results corroborated by computational studies, showed that the application of a transversal electrical field (V_{SG}) slightly perturb the molecular arrangement of crystallites, by inducing a tiny molecular tilt towards the direction of the applied field. Moreover, molecules tend to re-organize at grain boundaries. The structural modification was observed on apolar molecules arranged in high crystalline and high textured crystal grains. This phenomena may be stronger for polar molecules and/or disordered systems (e.g. polymers), opening up a new prospective to the interpretation of charge transport in organic electronic.

5.5 Bibliography

[1] H. L. Cheng, W. Y. Chou, C. W. Kuo, Y. W. Wang, Y. S. Mai, F. C. Tang and S. W. Chu. *Advanced Functional Materials* **18(2)**, 285–293 (2008)

[2] D. H. Juers and M. Weik. *Journal of Synchrotron Radiation* **18**, 329–337 (2011)

[3] P. O'Neill, D. L. Stevens and E. F. Garman. *Journal of Synchrotron Radiation* **9**, 329–332 (2002)

[4] A. Neuhold, J. Novak, H. G. Flesch, A. Moser, T. Djuric, L. Grodd, S. Grigorian, U. Pietsch and R. Resel. *Nuclear Instruments & Methods in Physics Research Section B-Beam Interactions with Materials and Atoms* **284**, 64–68 (2012)

[5] Y. Yoneda. *Physical Review* **131**, 2010–2013 (1963)

[6] G. H. Vineyard. *Physical Review B* **26(8)**, 4146–4159 (1982)

[7] B. E. Warren. X-ray diffraction (Dover, New York, 1990)

[8] D. M. Smilgies. *Journal of Applied Crystallography* **42**, 1030–1034 (2009)

[9] S. Schiefer, M. Huth, A. Dobrinevski and B. Nickel. *Journal of the American Chemical Society* **129(34)**, 10316–+ (2007)

[10] A. Brillante, I. Bilotti, R. G. Della Valle, E. Venuti, A. Girlando, M. Masino, F. Liscio, S. Milita, C. Albonetti, P. D'angelo, A. Shehu and F. Biscarini. *Physical Review B* **85(19)** (2012)

[11] A. Shehu, S. D. Quiroga, P. D'Angelo, C. Albonetti, F. Borgatti, M. Murgia, A. Scorzoni, P. Stoliar and F. Biscarini. *Physical Review Letters* **104(24)**, 246602 (2010)

[12] J. Rivnay, L. H. Jimison, J. E. Northrup, M. F. Toney, R. Noriega, S. F. Lu, T. J. Marks, A. Facchetti and A. Salleo. *Nature Materials* **8(12)**, 952–958 (2009)

[13] P. Annibale, C. Albonetti, P. Stoliar and F. Biscarini. *Journal of Physical Chemistry A* **111(49)**, 12854–12858 (2007)

CHAPTER 6

IN-SITU AND REAL TIME-STRUCTURAL STUDY ON HUMIDITY SENSITIVE ORGANIC THIN FILMS

This chapter summarizes the main preliminary results on the in-situ and real-time investigation of thin-films based on TTF molecule for future humidity sensing applications. This work is part of a collaboration with the group of Prof. Rovira of the Institut de Ciéncia de Materials de Barcelona (ICMAB), Consejo Superior de Investigaciones Cientificas (CSIC, Spain) and my main goal was to probe the effect of the humidity variation on a TTF based thin-film structure.

6.1 Introduction

The large variety of organic semiconducting materials that can be exploited in an OFET offers many opportunities for the fabrication of sensors. The field of application for sensing devices goes from medical diagnostics, food spoilage detection and monitoring of chemicals just to cite some [1, 2]. The increasing demand for small, portable and cheap sensors further moved the attention towards organic materials, which can be deposited at room temperature with low-cost fabrication techniques and on a variety of substrates, including flexible ones like plastic [3], paper [4] or cloths [5, 6]. Moreover organic materials can be easily tuned to change their physical and chemical properties and thus to improve the sensitivity to specific analytes.

Due to the important effect of humidity in several cases, such as moisture sensitive products, storage areas, computer rooms, hospitals, museums and libraries, examples of fabrication and study of humidity sensors based on organic compounds are abundant in literature and they often exploit metal-organic framework [7–9]. For an organic humidity sensor, the sensing effect relies on the absorption of moisture into the active layer that is exposed to the environment. The moisture can interact with the solely surface of the material or diffuse into it through grain boundaries. Especially in the latter case, this may cause a swelling of the film structure along with a doping-like mechanism that reduces the mobility of the OFETs [10]. This swelling effect can be quantified thanks to a structural characterization during the exposure of the organic material to the moisture, which is the case described in this chapter.

6.2 Experimental

6.2.1 Active materials

Composite films constituted by a thin conductive organic layer on top of a polymeric matrix are very attractive for a novel generation of devices. They combine the properties of organic metals, such as conductivity in a wide range of temperatures, with the characteristics of a polymeric matrix, like flexibility, transparency and low density. In this work, the sample investigated contains a conductive surface layer formed by linked microcrystals of $(BEDT-TTF)_xBr_y(H_2O)_n$ (Fiure 6.1). BEDT-TTF compound is just one of the several other TTF derivatives which have demonstrated good propensity to the formation of molecular metals [11, 12]. The film was prepared at the ICMAB-CSIC by the modified reticulate doping technique (MRDT) [13–16].

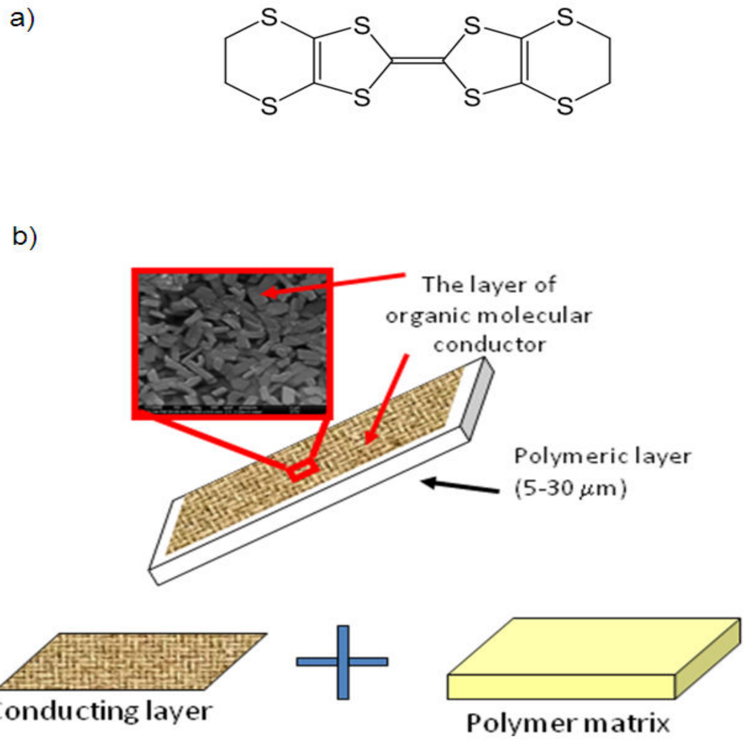

Figure 6.1: a) Chemical structure of BEDT-TTF an b) sketch of a sample prepared by MRDT technique. The red box contains a SEM image of the surface of a $(BEDT-TTF)_xBr_y(H_2O)_n$ film (courtesy of Dr. V. Lebedev, ICMAB-CSIC)

6.2.2 Thin-film fabrication

MRDT involves the generation of a conductive composite layer via donor plus halogen reaction. In the first step a non-conducting polymeric film with molecularly dispersed donors is cast. In the second step the surface of the obtained film is exposed to bromine (Br) vapors. A reaction brings to the crystallization of the complex at the top of the polymer matrix.

Bis(ethylenedithio) tetrathiafulvalene (BEDT-TTF), poly-(bisphenol-A-carbonate) (PC) in pellets (average Mw ca. 64,000) and 1,2-dichlorobenzene were purchased from Sigma Aldrich and no further purified. PC films (25-30 μm thickness) containing 8 wt.% of molecularly dispersed BEDT-TTF were prepared by drop casting a solution of BEDT-TTF (0.014 g) and PC (0.7 g) in 1,2-dichlorobenzene (25 ml) on a glass surface. The samples were kept in the oven at 130 °C for 20 minutes to allow the solvent evaporation. Subsequently, the film surface was treated with vapour from a Br_2/CH_2Cl_2 solution 10^{-5} mol/L. The reaction of the Br with the BEDT-TTF results in the crystallization of the complex in a form of fine network on top of the polymeric matrix.

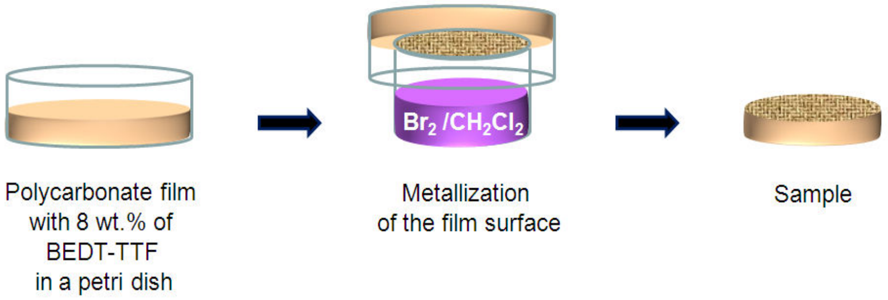

Figure 6.2: Schematic of the MRDT for the fabrication of a $(BEDT-TTF)_xBr_y(H_2O)_n$ film.

6.2.3 Experimental setup for in-situ structural investigation

X-rays measurements were carried out on a sample mounted in a home-made humidity chamber by means of a double-side tape and then installed on the goniometer of a rotating anode diffractometer (CuK_α, $\lambda = 1.54056$ $\AA$) (Figure 6.3). The chamber was connected to a hygrometer probe (HD2101.1 Delta OHM) and to a gas tube, through which a hydrate nitrogen flux was inflated, in order to reach the desired RH%. The flux was maintained as much stable as possible for 30 minutes before performing any X-ray measurement. Two kapton windows allowed the incident X-ray beam to reach the sample surface and the scattered beam the detector. A third hole in the chamber allowed to connect the thin-film contacts made by carbon paste to a Keithley 2636A dual channel parameter analyzer. Unfortunately for the sample investigated it was not possible to detect any current because of contacts deterioration.

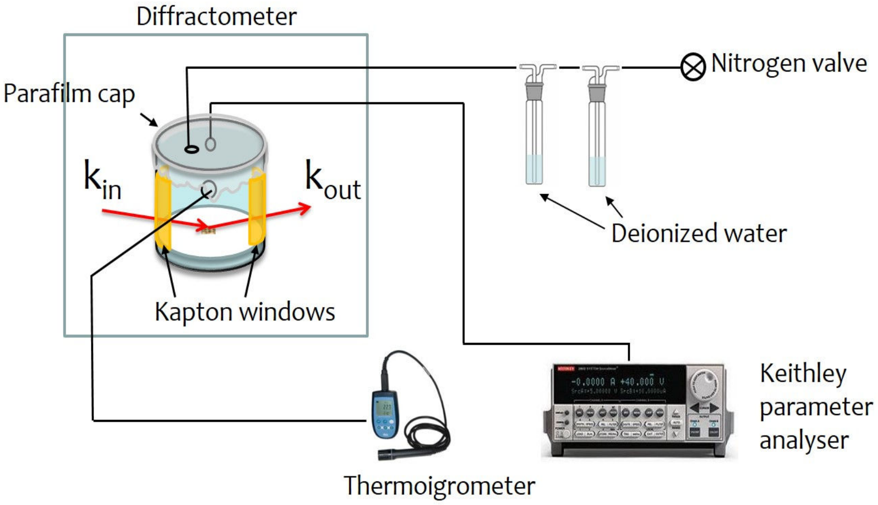

Figure 6.3: Schematic of the experimental setup.

6.3 Results and discussion

The preliminary structural characterization of the $(BEDT-TTF)_xBr_y(H_2O)_n$ thin-film, performed by a specular scan in the laboratory (Figure 6.4a), reveals that the film is crystalline and characterized by a series of intense an narrow Bragg reflections. By collecting a 2D-GIXRD image at the XRD1 beamline of the ELETTRA synchrotron facility (beam size 200x200 μm^2 and wavelength 1 $\AA$) (Figure 6.4b) it was possible to address the polychrystalline nature of the film, characterized by the co-presence of texturing (elongated Bragg spots along the q_z direction) and random oriented domains (rings in the 2D-GIXRD image). For the in-situ and real-time experiment the first two peaks in the specular direction were monitored during the RH% variation.

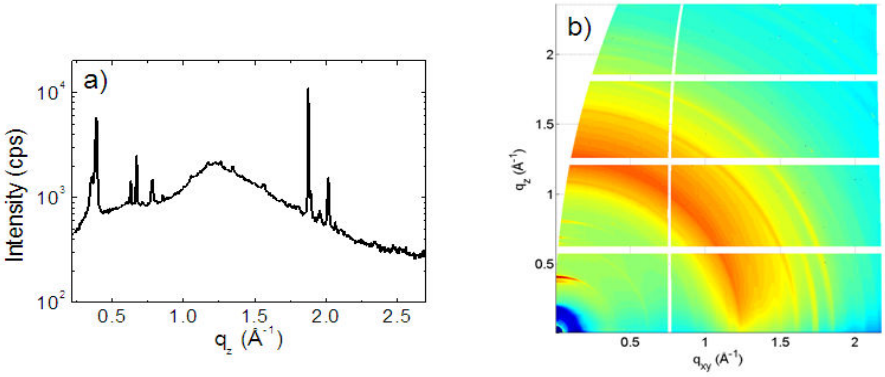

Figure 6.4: a) specular scan and b) 2D-GIXRD image of $(BEDT-TTF)_xBr_y(H_2O)_n$ thin-film.

The experiment was performed during the variation of the RH% from 10% to 80% (Figure

6.5a) and back (Figure 6.6a). From the measurements it is very clear that the variation of RH% affects the position of the first peak, which progressively shifts towards smaller q_z values as soon as the RH% increases and comes back to higher q_z values when RH% decreases, but lets the position of the second peak perfectly unchanged. This indicates that there are at least two different phases in this sample, one sensitive and another one totally careless to relative humidity variations. The peak position reversibly shifts from $q_z = 0.38$ to $q_z = 0.35$ $\AA^{-1}$, corresponding to a d-spacing variation of the 7% (from 16.56 to 17.74 $\AA$) with respect to the initial value d_0 (Figure 6.5b and 6.6b). It is interesting to notice that the lattice expansion, i.e. the d-spacing increment, happens gradually from 10% to 80% of RH, whereas the inverse process basically occurs between 30% and 20% of RH. This observation seems to indicates that, once embedded in the structure, water molecules are not easily released until a certain dry atmosphere is reached.

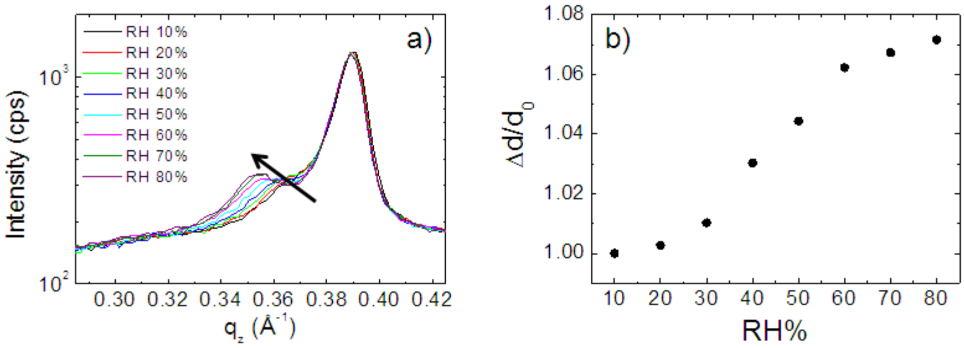

Figure 6.5: a) Evolution of the selected Bragg reflections during the increasing of RH% from 10% to 80% and b) d-spacing variation (Δd) with respect to the initial value (d_0).

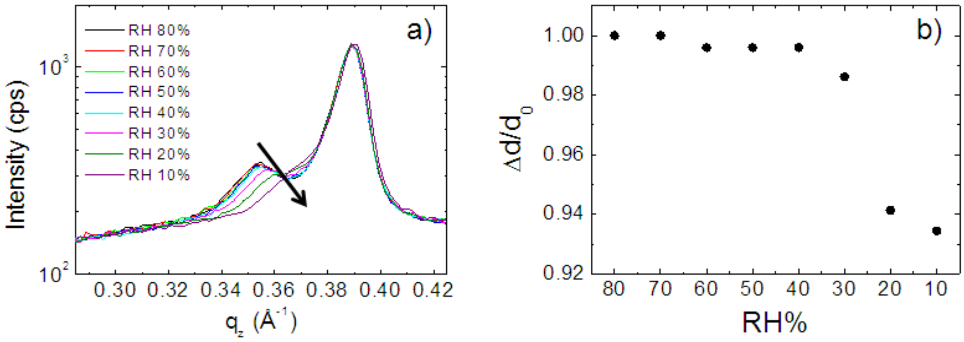

Figure 6.6: a) Evolution of the selected Bragg reflections during the decreasing of RH% from 80% to 10% and b) d-spacing variation (Δd) with respect to the initial value (d_0).

6.4 Conclusions

The pronounced shift in position of the Bragg peak centered around $q_z \sim 0.35\AA^{-1}$ indicates that the water molecules penetrated inside the crystallites of $(BEDT-TTF)_xBr_y(H_2O)_n$ sample reversibly modifying at least one crystallographic phase of the film. Haneda and co-workers performed a similar study on $(BEDO-TTF)_2Br(H_2O)_3$ complex [17]. Their results demonstrated quasi-reversible resistivity and d-spacing variation due to the RH% modification. In particular in their case, the d-spacing analyzed, associated by the authors to the inter-conducting layer distance [18], increased from 16.78 to 16.89 $\AA$ going from 9.8 to 63.8 % of RH. This result, even though very small, is in agreement with our findings and it has been explained as a water embedding in the film structure. Another interesting result of the Haneda work is the fact that the BEDO-TTF complex showed different crystal structures in relation to the RH%. At RH below 10% in fact, the Bragg reflection studied is replaced by the appearance of another peak centered at higher scattering angle but still sensitive to the humidity variation. Our setup did not allow for measurements under 10% of RH, but further optimization can be implemented to verify the presence of a different crystalline phase of BETD-TTF in extremely dry environmental conditions. Despite our results are in agreement with the literature, further investigations need to be carried out in order to depict a model of these TTF-based complex under the effect of humidity variation. It would be interesting, for example, to substitute Br with another halogen or to increase/decrease the wt.% of the material in the PC matrix, as well as to collect the structural response of BETD-TTF under 10% of RH, as already mentioned.

6.5 Bibliography

[1] L. Torsi, A. Dodabalapur, L. Sabbatini and P. G. Zambonin. *Sensors and Actuators B-Chemical* **67(3)**, 312–316 (2000)

[2] A. Kumar, P. Zhang, A. Vincent, R. McCormack, R. Kalyanaraman, H. J. Cho and S. Seal. *Sensors and Actuators B-Chemical* **155(2)**, 884–892 (2011)

[3] E. Laukhina, R. Pfattner, L. R. Ferreras, S. Galli, M. Mas-Torrent, N. Masciocchi, V. Laukhin, C. Rovira and J. Veciana. *Advanced Materials* **22(9)**, 977–+ (2010)

[4] D. Nilsson, T. Kugler, P. O. Svensson and M. Berggren. *Sensors and Actuators B-Chemical* **86(2-3)**, 193–197 (2002)

[5] L. R. Ferreras, R. Pfattner, M. Mas-Torrent, E. Laukhina, L. Lopez, V. Laukhin, C. Rovira and J. Veciana. *Journal of Materials Chemistry* **21(3)**, 637–640 (2011)

[6] J. T. Mabeck and G. G. Malliaras. *Analytical and Bioanalytical Chemistry* **384(2)**, 343–353 (2006)

[7] S. Achmann, G. Hagen, J. Kita, I. M. Malkowsky, C. Kiener and R. Moos. *Sensors* **9(3)**, 1574–1589 (2009)

[8] L. E. Kreno, K. Leong, O. K. Farha, M. Allendorf, R. P. Van Duyne and J. T. Hupp. *Chemical Reviews* **112(2)**, 1105–1125 (2012)

[9] N. Parvatikar, S. Jain, S. Khasim, M. Revansiddappa, S. V. Bhoraskar and M. C. N. A. Prasad. *Sensors and Actuators B-Chemical* **114(2)**, 599–603 (2006)

[10] F. Liao, C. Chen and V. Subramanian. *Sensors and Actuators B-Chemical* **107(2)**, 849–855 (2005)

[11] M. Mas-Torrent, E. Laukhina, C. Rovira, J. Veciana, V. Tkacheva, L. Zorina and S. Khasanov. *Advanced Functional Materials* **11(4)**, 299–303 (2001)

[12] E. Laukhina, E. Ribera, J. Vidal-Gancedo, S. Khasanov, L. Zorina, R. Shibaeva, E. Canadell, V. Laukhin, M. Honold, M. S. Nam, J. Singleton, J. Veciana and C. Rovira. *Advanced Materials* **12(1)**, 54–+ (2000)

[13] J. K. Jeszka, J. Ulanski and M. Kryszewski. *Nature* **289(5796)**, 390–391 (1981)

[14] J. Ulanski, J. K. Jeszka, A. Tracz, I. Glowacki, M. Kryszewski and E. Laukhina. *Synthetic Metals* **56(1)**, 2001–2006 (1993)

[15] E. Laukhina, C. Rovira and J. Ulanski. *Synthetic Metals* **121(1-3)**, 1407–1408 (2001)

[16] E. Laukhina, V. Tkacheva, I. Chuev, E. Yagubskii, J. Vidal-Gancedo, M. Mas-Torrent, C. Rovira, J. Veciana, S. Khasanov, R. Wojciechowski and J. Ulanski. *Journal of Physical Chemistry B* **105(45)**, 11089–11097 (2001)

[17] T. Haneda, A. Tracz, G. Saito and H. Yamochi. *Journal of Materials Chemistry* **21(5)**, 1621–1626 (2011)

[18] S. Horiuchi, H. Yamochi, G. Saito, J. K. Jeszka, A. Tracz, A. Sroczynska and J. Ulanski. *Molecular Crystals and Liquid Crystals Science and Technology Section a-Molecular Crystals and Liquid Crystals* **296**, 365–382 (1997)

CHAPTER 7

CONCLUSIONS AND PERSPECTIVES

This thesis presented the results derived from the investigation of the correlation between structural and electrical properties of different organic semiconducting systems.

The success of chemists in synthesizing new performing compounds with ad-hoc properties enormously enlarged the already abundant variety of organic materials available for future applications. In this manuscript examples of systems based on p-type and n-type small molecules, either processed from solution or from vacuum sublimation, and polymers were given. The structural characterization of these systems was carried out by means of X-ray diffraction techniques exploiting both common laboratory sources and synchrotron radiation. The information obtained on the crystalline order, packing and arrangement of the organic films were correlated with the performance of the corresponding OFETs. To reach this ultimate aim, the approaches utilized were two: a more common ex-situ approach, involving steps of different characterizations on the system at the equilibrium, and a less ordinary one, based on the structural characterization of a system in non-equilibrium conditions, named in-situ and real-time approach.

In organic electronics it is well known that the electrical performance of an OFET are strictly dependent on the crystalline order of the active layer. Nevertheless, the first study presented in this thesis demonstrated that design and synthesis of highly processable molecules with strong supramolecular rearrangement capabilities upon common post-deposition treatments, at the expenses of crystalline order, can be a good strategy to obtain remarkable charge transport in devices. In particular, we determined the effect of the alkyl side chains design on the structural, electrical and morphological properties of spin-coated PDI derivative thin films. Ex-situ X-ray measurements revealed that the substitution of linear alkyl side chains with asymmetric branched ones introduced configurational disorder in the structure due to the formation of four different stereoisomers. This disorder was responsible for the solubility improvement and for the 2D-growth mode of the films. By a simple thermal treatment these characteristics favored a phase transition from a more disordered and metastable crystalline phase towards a more ordered one, still preserving the 2D morphology and thus favoring the charge transport.

The ex-situ approach was also applied to more disordered systems like polymers. In particular in this manuscript we presented for the first time the fabrication of performing polymeric ambipolar bilayers with both n- and p-type active materials deposited from solution. The big dimensions of these materials, related to the long and bulky alkyl chains as well as the presence of a rigid backbone, affect their packing and rearranging capabilities. To overcome this issue and to allow the deposition of multiple layers from solution, the Langmuir-Schaefer technique was exploited. From the structural investigation it emerged that this particular deposition technique forces the organization of the polymeric lamella in a configuration particularly suitable for the charge transport. In the case of the n-type polymer a post-deposition thermal treatment favored the reorganization of the material on the substrate surface, leading to a smoother and continuous morphology, an improving in crystallinity and an enhancement of the device performance. In the case of the p-type polymer the deposition technique imparted the formation of fibers with a preferential growing direction. Several ambipolar architectures depending on the relative position of the n- and p-type materials were studied. Remarkable holes and electron mobilities of the order of 10^{-1} cm^2/Vs were reached in the geometries with the n-type material in contact with the substrate and the p-type material on top of it. The reasons behind the poor electrons charge transport in the reversed architecture (n-type material on top and p-type material at the interface with the dielectric) are still unclear. We think that further investigations, comprising X-ray reflectivity and ultraviolet photoemission spectroscopy measurements, will help us figuring out the charge transport mechanism taking place in these bilayer ambipolars.

Two examples of in-situ and real-time structural investigations were presented in the second half of the thesis.

The results obtained in the first case are unprecedented in literature and tackle a fundamental question in organic electronics. As already mentioned, it is well established that the structural order of the semiconducting layer of an OFET has important consequences on the charge transport in the devices, but little was known about the reverse, that is about the effect of the application of an electric field governing the charge transport to the structure of the organic semiconductor. We answered this question by performing in-situ and real-time structural investigation on vacuum sublimated pentacene OFETs with an ad-hoc geometry. X-ray diffraction measurements, both in specular and grazing incidence configurations, based on synchrotron radiation were performed inside the transistor channel during the application of the V_{SG} and V_{SD} bias. This study clearly demonstrated that the electric field induces a small tilt (2 mrad) on the pentacene molecules. We believe that by using a different molecule, for example a polar one, this effect would be much more pronounced. This outstanding result poses the perspective of charge transport from another point of view, which is not the one of the carriers traveling inside the semiconductor, but it is the one of the semiconductor responding to the electric field application.

The in-situ and real-time approach was also exploited with common laboratory X-ray sources for the structural study of TTF-based thin films for future humidity sensing applications. A humidity chamber which allows the simultaneous structural and electrical characterization of these films in controlled atmosphere was built. The preliminary results presented in this thesis highlighted a reversible structural response of the films to the variation of the RH% in the atmosphere . In particular, the increment of RH% promotes the encapsulation of water molecules in the structure, deduced by the increasing of the d-spacing relative to a particular Bragg reflection. These water molecules are then released by reducing RH% to very dry conditions. Unfortunately, it was not possible to perform electrical measurements due to some contacts problems but future improvement in the setup will guarantee to collect the electrical response of the film during the RH% variation simultaneously with the X-ray measurements.

The results presented are the outcome of multi-technique investigations on thin films devices. We demonstrated that both the approaches adopted, ex-situ and in-situ and real-time, gave irreplaceable support to the description of the relationship between structural and electrical properties of very different organic materials. We believe that this thesis will help convincing that this type of studies are necessary for the progress towards a new generation of materials suitable for electronic applications. Enormous advances have already been made for example in the field of sensing, robotics and medical science, but more can be achieved if a deep and scrupulous characterization of the synthesized materials will be carried out as a standard.

LIST OF PUBLICATIONS

L. Ferlauto, F. Liscio, E. Orgiu, S. Bonacchi, L. Barba, S. Milita, P. Samorí, ″Ultra-thin bi-layer ambipolar field-effect transistors based on solution processable conjugated polymers″, in preparation

F. Liscio, **L. Ferlauto**, R. Pfattner, M. Matta, F. Zerbetto, S. Milita, F. Biscarini, ″Does the organic field-effect transistor operation affect the molecular film structure?″, in preparation

M. A. Squillaci,**L. Ferlauto**, Y. Zagranyarski, S. Milita, K. Müllen, P. Samorí, ″Self-assembly of an amphiphilic π-conjugated dyad into fibers: ultrafast and ultrasensitive humdity sensor″, *Adv. Mater.* accepted

L. Ferlauto, F. Liscio, E. Orgiu, N. Masciocchi, A. Guagliardi, F. Biscarini, P. Samorí, S. Milita, ″Enhancing the charge transport in solution-processed perylene di-imide transistors via thermal annealing of metastable disordered films″, *Adv. Funct. Mater.* 24, 5503-5510 (**2014**)

D. Gentili, P. Sonar, F. Liscio, T. Cramer, **L. Ferlauto**, F. Leonardi, S. Milita, A. Dodabalapur, M. Cavallini, ″Logic-gate devices based on printed polymer semiconducting nanostripes″, *NANO LETTERS* 13, 3643-3647 (**2013**)

F. Liscio, C. Albonetti, K. Broch, A. Shehu, S. D. Quiroga, **L. Ferlauto**, C. Frank, S. Kowarik, R. Nervo, A. Gerlach, S. Milita, F. Schreiber, F. Biscarini, ″Molecular reorganization in organic field-effect transistors and its effect on two-dimensional charge transport pathways″, *ACS NANO* 7, 1257-1264 (**2013**)

D. Gentili, F. di Maria, F. Liscio, **L. Ferlauto**, F. Leonardi, L. Maini, M. Gazzano, S. Milita, G. Barbarella, M. Cavallini, ″Targeting ordered oligothiophene fibers with enhanced functional properties by interplay of self-assembly and wet lithography″, *J. Mater. Chem.* 22, 20852-20856, (**2012**)

SCHOOLS AND CONFERENCES

Schools

- ”School of health and biosciences”, Como (Italy) $18^{th} - 23^{th}$ June 2012
- ”Structure, microstructure, nanostructure: exploiting the potential of powder diffraction techniques”, Trento (Italy) $15^{th} - 20^{th}$ September 2012

Contributed talks

L. Ferlauto, F. Liscio, E. Orgiu, N. Masciocchi, A. Guagliardi, F. Biscarini, P. Samorí, S. Milita, ”Alkyldiimide perylenes: unusual correlation between structural and electrical properties”. Presented at:

- 9^{th} International Conference of Organic Electronics (ICOE), Grenoble $17^{th} - 20^{th}$ June 2013

Posters

L. Ferlauto, F. Liscio, E. Orgiu, N. Masciocchi, A. Guagliardi, F. Biscarini, P. Samorí, S. Milita, ”The surprising role of asymmetric alkyl-chains in perylene di-imide semiconductors”. Presented at:

- AIC-SILS Conference 2014 - 2^{nd} joint Conference of the Italian Crystallographic Association (AIC) and of the Italian Synchrotron Radiation Society (SILS), Florence (Italy) $15^{th} - 18^{th}$ September 2014
- 7^{th} International Conference on Molecular Electronics (ElecMol), Strasbourg (France) $24^{th} - 29^{th}$ August 2014
- 10^{th} International Conference of Organic Electronics (ICOE), Modena (Italy) $11^{th} - 13^{th}$ June 2014
- Meeting of Italian, Spanish and Swiss Crystallographic Association (MISSCA), Como (Italy) $9^{th} - 12^{th}$ September 2013
- Supramolecular Functional Systams for Organic Electronics (SUPERIOR), Strasbourg (France) $26^{th} - 28^{th}$ June 2013

L. Ferlauto, F. Liscio, S. Milita, A. Shehu, P. Evans, M. Murgia, F. Biscarini, ”Real time microstructural investigation of pentacene film on operating organic thin-film transistors”. Presented at:

- 7^{th} International Conference of Organic Electronics (ICOE), Rome (Italy) $22^{nd} - 24^{th}$ June 2011

UNIVERSITÉ DE STRASBOURG

Laura FERLAUTO

EDSC
Ecole Doctorale des
Sciences Chimiques

Correlation between structural and electrical properties of organic semiconducting materials

Résumé

Cette thèse présente plusieurs techniques de caractérisation appliquées à différents matériaux organiques dans le but d'élucider la relation entre leur structure et leurs propriétés après intégration comme matériaux actifs dans des dispositifs OFET. Un soin particulier est porté aux méthodes de caractérisation structurale (2D-GIXRD, XRR et XRD) avec une source classique disponible en laboratoire ou par rayonnement synchrotron. Divers matériaux organiques, dont des petites molécules et des polymères de type p et n déposés en solution ou par sublimation sous vide, sont étudiés. En particulier, l'étude d'OFET à base de deux isomères de péryléne fonctionnalisés ne différant que par la structure de leurs chaînes latérales alkyle démontre que la nature ramifiée et asymétrique de ces dernières peut conduire à une amélioration des performances électriques avec un simple traitement thermique post-dépôt, tandis que la fabrication de dispositifs ambipolaires à base de polymères avec la technique de Langmuir-Schaefer souligne l'importance de la méthode de dépôt sur l'arrangement du matériau sur la surface du substrat. Une approche moins conventionnelle, nommée étude structurale in situ et en temps réel, est aussi présentée pour évaluer les modifications structurales dans les couches minces organiques subissant un processus particulier. Plus précisément, la réponse structurale de couches minces de pentacène à l'application de V_{SG} et V_{SD} à l'OFET et de couches minces de dérivés de TTF à la variation de l'humidité a été étudiée.

Mots-clés: transistors organiques à effet de champ, matériaux organiques, diffraction des rayons X, transport de charges.

Abstract

This thesis presents multiple characterization techniques applied to various organic materials with the ultimate goal of unraveling their structure-properties relationship once encapsulated as active materials in OFETs devices. Particular care is then dedicated to the structural characterization methods (2D-GIXRD, XRR and XRD) both from classical laboratory source and from synchrotron radiation. Various organic materials, comprising p- and n-type small molecules and polymers deposited from solution or by vacuum sublimation are investigated. In particular, the study on OFETs based two functionalized perylene isomers differing only in the shape of the alkyl side-chians demonstrates how the branched and asymmetric nature of the chains can lead to an improvement of the electrical performance with a simple post-deposition thermal treatment, while the fabrication of ambipolar polymeric devices by means of Langmir-Schaefer technique highligts the importance of the deposition method on the arrangement of the material on the substrate surface. A more unusual approach, named in-situ and real-time structural investigation, is also presented to evaluate structural modifications in organic thin films undergoing a particular process. Specifically, the structural responce of pentacene thin films to the application of V_{SG} and V_{SD} to the OFET and of TTF derivatives thin films to the variation of humidty were investigated.

Keywords: organic field effect transistors, organic materials, X-ray diffraction, charge transport.